NASA/TP—2011–214657

# Extension of Ko Straight-Beam Displacement Theory to Deformed Shape Predictions of Slender Curved Structures

*William L. Ko and Van Tran Fleischer*

*Dryden Flight Research Center, Edwards, California*

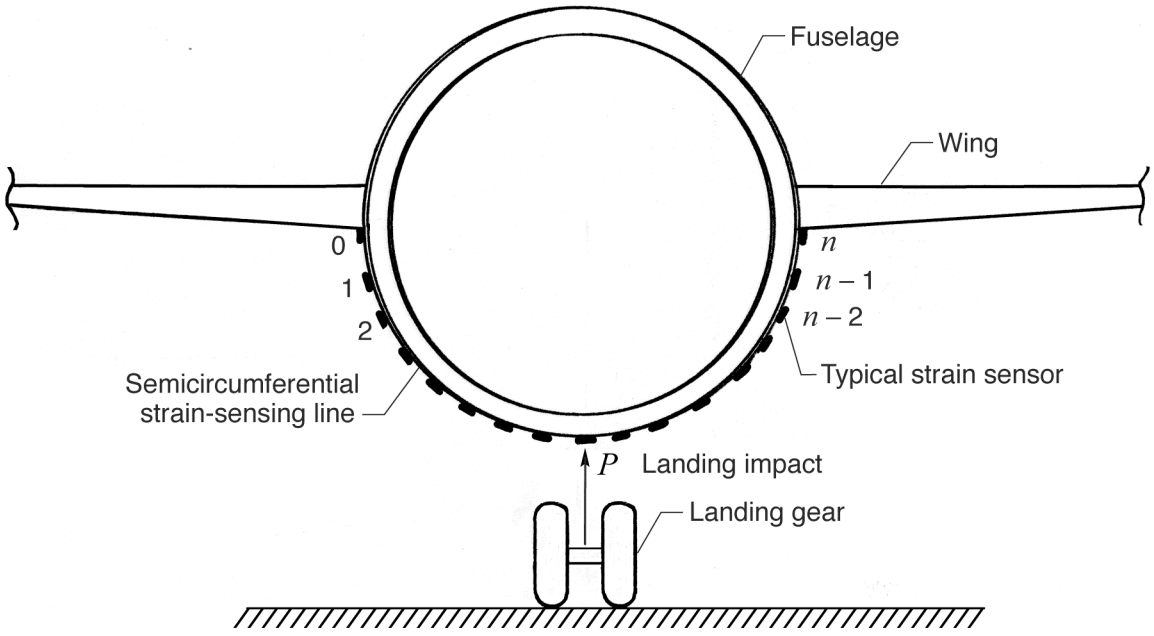


**April 2011**

# NASA STI Program ... in Profile

Since its founding, NASA has been dedicated to the advancement of aeronautics and space science. The NASA scientific and technical information (STI) program plays a key part in helping NASA maintain this important role.

The NASA STI program operates under the auspices of the Agency Chief Information Officer. It collects, organizes, provides for archiving, and disseminates NASA's STI. The NASA STI program provides access to the NASA Aeronautics and Space Database and its public interface, the NASA Technical Report Server, thus providing one of the largest collections of aeronautical and space science STI in the world. Results are published in both non-NASA channels and by NASA in the NASA STI Report Series, which includes the following report types:

- TECHNICAL PUBLICATION. Reports of completed research or a major significant phase of research that present the results of NASA Programs and include extensive data or theoretical analysis. Includes compilations of significant scientific and technical data and information deemed to be of continuing reference value. NASA counterpart of peer-reviewed formal professional papers but has less stringent limitations on manuscript length and extent of graphic presentations.

- TECHNICAL MEMORANDUM. Scientific and technical findings that are preliminary or of specialized interest, e.g., quick release reports, working papers, and bibliographies that contain minimal annotation. Does not contain extensive analysis.

- CONTRACTOR REPORT. Scientific and technical findings by NASA-sponsored contractors and grantees.

- CONFERENCE PUBLICATION. Collected papers from scientific and technical conferences, symposia, seminars, or other meetings sponsored or co-sponsored by NASA.

- SPECIAL PUBLICATION. Scientific, technical, or historical information from NASA programs, projects, and missions, often concerned with subjects having substantial public interest.

- TECHNICAL TRANSLATION. English-language translations of foreign scientific and technical material pertinent to NASA's mission.

Specialized services also include organizing and publishing research results, distributing specialized research announcements and feeds, providing help desk and personal search support, and enabling data exchange services.

For more information about the NASA STI program, see the following:

- Access the NASA STI program home page at *http://www.sti.nasa.gov*

- E-mail your question via the Internet to help@sti.nasa.gov

- Fax your question to the NASA STI Help Desk at 443-757-5803

- Phone the NASA STI Help Desk at 443-757-5802

- Write to:
  NASA STI Help Desk
  NASA Center for AeroSpace Information
  7115 Standard Drive
  Hanover, MD 21076-1320

NASA/TP—2011–214657

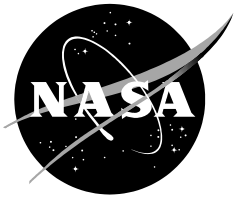

# Extension of Ko Straight-Beam Displacement Theory to Deformed Shape Predictions of Slender Curved Structures

*William L. Ko and Van Tran Fleischer*

*Dryden Flight Research Center, Edwards, California*

National Aeronautics and
Space Administration

*Dryden Flight Research Center*
*Edwards, CA 93523-0273*

**April 2011**

The structural shape prediction method described in this report is protected under U.S. Patent No. 7,520,176, issued April 21, 2009. Therefore, those interested in using the method should contact the NASA Innovative Partnership Program Office at the Dryden Flight Research Center for more information.



Available from:

NASA Center for AeroSpace Information
7115 Standard Drive
Hanover, MD 21076-1320
443-757-5802

# TABLE OF CONTENTS

# ABSTRACT

The Ko displacement theory originally developed for shape predictions of straight beams is extended to shape predictions of curved beams. The surface strains needed for shape predictions were analytically generated from finite-element nodal stress outputs. With the aid of finite-element displacement outputs, mathematical functional forms for curvature-effect correction terms are established and incorporated into straight-beam deflection equations for shape predictions of both cantilever and two-point supported curved beams. The newly established deflection equations for cantilever curved beams could provide quite accurate shape predictions for different cantilever curved beams, including the quarter-circle cantilever beam. Furthermore, the newly formulated deflection equations for two-point supported curved beams could provide accurate shape predictions for a range of two-point supported curved beams, including the full-circular ring. Accuracy of the newly developed curved-beam deflection equations is validated through shape prediction analysis of curved beams embedded in the windward shallow spherical shell of a generic crew exploration vehicle. A single-point collocation method for optimization of shape predictions is discussed in detail.


# NOMENCLATURE

| | |
|---|---|
| $c$ | distance from neutral axis to outermost surface point of uniform beam (depth factor), in. |
| CC | both ends clamped |
| CEV | crew exploration vehicle |
| $c_i$ | $\equiv c(x_i)$ distance from neutral axis to $i$-th strain sensor, in. |
| $c_n$ | value of $c_i$ at free end (beam tip), $x = x_n = l$, in. |
| $c(x)$ | distance from neutral axis to outermost surface point of nonuniform beam (or radius of tapered tubular beam) at axial location, $x$, in. |
| $c_0$ | value of $c_i$ at fixed end (beam root), $x = x_0 = 0$, in. |
| deg | degree |
| $E$ | Young's modulus, lb/in$^2$ |
| $e_i$ | $\equiv y_i - y_i^C$, shape prediction error at strain-sensing station, $x_i$ |
| $e_n$ | $\equiv y_n - y_n^C$, shape prediction error at cantilever curved-beam tip, in. |
| $\hat{e}_n$ | $\equiv \hat{y}_n - y_n^C$, reduced shape prediction error at cantilever curved-beam tip, in. |
| $h$ | depth of beam, in. |
| $i$ | index associated with $i$-th strain sensor at $x_i$ ($i$ = 0, 1, 2, 3, …, $n$) |
| $I$ | moment of inertia, in$^4$ |
| $j$ | index, 1, 2, 3, … |
| $k_{in}$ | $\equiv \sigma_{in}/\sigma$, bending stress ratio on concave side |
| $k_{out}$ | $\equiv \sigma_{out}/\sigma$, bending stress ratio on convex side |
| $l$ | length of beam, in. |
| $M$ | bending moment, in-lb |
| $M_i$ | bending moment at $x_i$, in-lb |
| $n$ | index of last strain sensor (also used to indicate strain-sensing station density) |
| $P$ | force, lb |
| $R$ | radius of curvature of curved beam, in. |

SPAR Structural Performance And Resizing
SS both ends simply supported
TPS thermal protection system
UAV unmanned aerial vehicle

$x$ axial coordinate of beam measured from left end, in.

$x_i$ $x$-coordinate (or symbol) of strain-sensing station (cross section) where $i$-th strain sensor is located, in.

$y$ beam deflection normal to $x$-axis, in.

$y_i$ deflection of cantilever straight beam at $x_i$, in.

$y_i^B$ deflection of two-point supported straight beam at $x_i$, in.

$y_i^C$ radial deflection of curved beam at $i$-th strain-sensing station calculated from SPAR, in.

$\hat{y}_i$ radial deflection of curved beam at $i$-th strain-sensing station, in.

$\hat{y}_i^B$ radial deflection of two-point supported curved beam at $i$-th strain-sensing station, in.

$\delta$ neutral axis offset (distance between neutral axis and centroidal axis), in.

$\Delta l$ $= l/n$, distance between two adjacent strain-sensing stations, in.

$\Delta\phi$ $\equiv \phi_n/n$, angular coordinate differential between two adjacent strain-sensing stations, deg

$\varepsilon_i$ surface bending strain at $i$-th strain-sensing station, in/in.

$\varepsilon(x)$ surface bending strain at axial location, $x$, in/in.

$\eta$ $\equiv y_{n/2}^C - y_{n/2}^B$, amplitude of sine correction function, in.

$\theta_i$ deformed beam slope at axial location, $x_i$, rad or deg

$\theta(x)$ deformed beam slope at axial location, $x$, rad or deg

$\sigma$ magnitude of surface bending stress of equivalent straight beam, lb/in$^2$

$\sigma_{in}$ magnitude of bending stress on concave side of curved beam, lb/in$^2$

$\sigma_{out}$ magnitude of bending stress on convex side of curved beam, lb/in$^2$

$\phi_i$ angular coordinate (measured from left end of beam) of $i$-th strain-sensing station, deg

$\phi_n$ angular coordinate (measured from left end of beam) of $n$-th (last) strain-sensing station (called curved-beam angle), deg

# INTRODUCTION

By installing a series of strain sensors at discrete points along the surface of a beam-like structure (such as an aircraft wing), one can use the measured surface strains as input to the Ko displacement theory to calculate structural deflections and cross-sectional rotations at discrete points for mapping the structural deformed shapes. The most attractive strain-sensing system, an alternative to the conventional strain gage system (which contains too much lead wire weight), is the fiber-optic strain-sensing system, because the fiber optics are lightweight, fine, and flexible filaments (approximately the size of human hairs), and they can be highly multiplexed (Bragg gratings) to define sensing stations at desired sensing intervals (refs. 1–3). In the formulation of the Ko displacement theory (refs. 4–7), the beam was first divided into multiple domains of equal length, so that variations of both bending strain and beam depth could be assumed to be linear within in each small domain. This approach enabled piecewise integrations of the classical beam differential equation to yield beam slope and deflection equations for each domain. The resulting displacement equations were then expressed in terms of strains measured at multiple equally

spaced strain-sensing stations (at domain junctures) on the surface of the beam structures. The surface strain data could then be input to the displacement equations for the calculation of slopes, deflections, and cross-sectional twist angles of the beam structures at the strain-sensing cross sections for generating the overall deformed shapes of the beam structures.

The Ko displacement theory (refs. 4–7), combined with the onboard fiber-optic strain-sensing system, form a powerful tool (called *Method for Real-Time Structure Shape-Sensing*, U.S. Patent No. 7,520,176; ref. 8) for in-flight deformed shape monitoring of flexible wings and tails (such as those often employed on unmanned aerial vehicles, UAVs) by the ground-based pilot for maintaining safe flights. In addition, the wing shape, monitored in real time, could be input to the aircraft control system for aeroelastic wing shape control. The fiber-optic strain-sensing technique (refs. 4–8) has been further applied to a new reverse process (called *Process for Using Surface Strain Measurements to Obtain Operational Loads for Complex Structures*, U.S. Patent No. 7,715,994; ref. 9) for structural operational load monitoring.

The Ko displacement theory (refs. 4–8) was originally developed for predicting the deformed shapes of straight beams (cantilever and two-point supported beams). In addition, the theory can also be applied to shape predictions of unsupported free-free beam-like structures, such as aircraft wings and fuselages, during flight. The displacement theory (refs. 4–5) has been successfully validated for its accuracy by finite-element analysis of different sample structures such as cantilever tubular beams (uniform, tapered, slightly tapered, step-wise tapered), two-point supported tapered tubular beams, flat panels, and tapered wing boxes (unswept and swept).

By introducing curvature-effect corrections, one can modify the straight-beam displacement theory (refs. 4–7) for shape predictions of curved beams. Mathematical functional forms of the curvature-effect correction terms could be established, with the aid of finite-element displacement solutions, and incorporated into the straight-beam deflection equations for the formulation of curved-beam deflection equations.

This technical report examines the prediction errors arising from the use of straight-beam deflection equations for shape predictions of curved beams, and demonstrates the methods used in the formulation of curved-beam deflection equations for shape predictions of both cantilever and two-point supported curved beams. The accuracy of the newly formulated curved-beam deflection equations has been validated through shape prediction analysis of curved beams embedded in the windward shallow spherical wall of a generic crew exploration vehicle (CEV). This report also discusses the single-point collocation method for optimizing the accuracy of the shape predictions of curved beams.

# BASICS OF THE KO DISPLACEMENT THEORY

The basics of the Ko displacement theory for the straight beams (refs. 4–5) are briefly described in this section. The principal assumptions made in the formulation of the theory also are discussed.

## Beam Differential Equations

The formulation of the displacement theory is built upon the classical beam differential equation (elastic curvature of a deformed straight beam) given by (refs. 10–11)

$$\frac{d^2y}{dx^2} = \frac{M(x)}{EI} \tag{1}$$

in which $y$ is the lateral deflection, $x$ is the beam axial coordinate, $M(x)$ is the bending moment, $E$ is the Young's modulus, and $I$ is the moment of inertia.

At the cross section, $x$, the bending moment, $M(x)$, and associated bending strain, $\varepsilon(x)$, induced at the bottom (or top) fiber (outermost point from the neutral axis) of the nonuniform straight beam can be written as (refs. 4–5)

$$M(x) = EI\,\frac{\varepsilon(x)}{c(x)} \tag{2}$$

in which $c(x)$ is the local half depth (distance from the neutral axis to the bottom surface) of the nonuniform beam. When equations (1) and (2) are combined, the modified differential equation for the nonuniform beam is obtained as

$$\frac{d^2y}{dx^2} = \frac{\varepsilon(x)}{c(x)} \tag{3}$$

Note that under the present strain formulation, the modified beam differential equation (3) contains only the beam half depth, $c(x)$, and the bending strain, $\varepsilon(x)$. The flexural rigidity, $EI$, is eliminated. Formulation of the Ko displacement theory (refs. 4–5) for nonuniform straight beams is based upon the modified beam differential equation (3), which could be sufficiently accurate if the nonuniform beam cross sections change gradually (ref. 10, p. 143).

If the mathematical functional forms of $\{c(x), \varepsilon(x)\}$ are given, equation (3) can be integrated once to yield the beam slope, $dy/dx$. The equation can then be integrated a second time to yield the beam deflection, $y(x)$, for the shape predictions.

## Basic Assumptions

When the single and double integrations of equation (3) were carried out, the following assumptions were made:

1. The nonuniform beam of length $l$ (fig. 1) is discretized into $n$ domains of equal length, $\Delta l (= l/n)$, and the beam section within each domain is assumed to linearly taper down (or linearly taper up). The strain sensors, $i$ (= 0, 1, 2, 3,…, $n$), are to be installed at the bottom (or top) of the domain junctures, $x = x_i$ ($i$ = 0, 1, 2, 3,…, $n$) (also called strain-sensing stations, $x_i$). Thus, in the domain, $x_{i-1} \le x \le x_i$, between any two adjacent strain-sensing stations, $\{x_{i-1}, x_i\}$, the beam half depth, $c(x)$, can be expressed as a linear function of $(x - x_{i-1})$ as

$$c(x) = c_{i-1} - (c_{i-1} - c_i)\frac{x - x_{i-1}}{\Delta l} \quad ; \quad x_{i-1} \le x \le x_i \tag{4}$$

in which $\{c_{i-1},\ c_i\}$ are the values of $c(x)$ at the strain-sensing stations, $\{x_{i-1}, x_i\}$, respectively.

2. The distribution of the bending strain, $\varepsilon(x)$, in the domain, $x_{i-1} \le x \le x_i$, between the two adjacent strain-sensing stations, $\{x_{i-1}, x_i\}$, is also assumed to change linearly with $(x - x_{i-1})$ as

$$\varepsilon(x) = \varepsilon_{i-1} - (\varepsilon_{i-1} - \varepsilon_i)\frac{x - x_{i-1}}{\Delta l} \qquad ; \qquad x_{i-1} \le x \le x_i \tag{5}$$

in which $\{\varepsilon_{i-1}, \varepsilon_i\}$ are the values of $\varepsilon(x)$ at the strain-sensing stations, $\{x_{i-1}, x_i\}$, respectively.

## Linearity of Bending Moments

Note that for a slightly nonuniform beam, $c(x)$ is a weak linear function of $(x - x_{i-1})$ (the small slope term in eq. (4)), and the associated bending moment, *M(x)* (eq. (2)), will vary almost linearly between the two adjacent strain-sensing stations, $\{x_{i-1}, x_i\}$, because the higher-order terms in the binomial expansion of the denominator $[c(x)]^{-1}$ may be neglected. This argument may not hold, however, if $c(x)$ is not a weak linear function of $x$, because the higher-order terms in the binomial expansion of the denominator $[c(x)]^{-1}$ must be retained.

For the uniform beam ( $c(x) = c =$ constant), the bending moment, *M(x)*, is directly proportional to the bending strain, $\varepsilon(x)$, according to equation (2). Therefore, if the strain, $\varepsilon(x)$, is a linear function of $x$ given by equation (5), then *M(x)* will also be a linear function of $x$.

## Beam Slopes and Deflections

The slope, $\tan\theta(x)(\equiv dy/dx)$, of the nonuniform beam at the axial location, $x$, within the domain, $x_{i-1} \le x \le x_i$ (fig. 1), can be obtained by integrating equation (3) once, and enforcing the continuity of the slope at the inboard strain-sensing station, $x_{i-1}$, as

$$\tan\theta(x) = \underbrace{\int_{x_{i-1}}^{x} \frac{d^2y}{dx^2}\,dx}_{\text{Integration of eq. (3)}} + \underbrace{\tan\theta_{i-1}}_{\text{Slope at } x_{i-1}} = \underbrace{\int_{x_{i-1}}^{x} \frac{\varepsilon(x)}{c(x)}\,dx}_{\substack{\text{Slope increment} \\ \text{above } \tan\theta_{i-1}}} + \underbrace{\tan\theta_{i-1}}_{\text{Slope at } x_{i-1}} \qquad ; \qquad (x_{i-1} \le x \le x_i) \tag{6}$$

in which $\tan\theta_{i-1}$ is the slope at the inboard strain-sensing station, $x_{i-1}$. The deflection, $y(x)$, of the nonuniform beam within the domain, $x_{i-1} \le x \le x_i$ (fig. 1), can be obtained by integrating slope equation (6), and enforcing the continuity of deflection at the inboard adjacent strain-sensing station, $x_{i-1}$, as

$$y(x) = \underbrace{\int_{x_{i-1}}^{x} \tan\theta(x)\,dx}_{\substack{\text{Integration of}\\ \text{eq. (6)}}} + \underbrace{y_{i-1}}_{\substack{\text{Deflection}\\ \text{at } x_{i-1}}} = \underbrace{\int_{x_{i-1}}^{x}\int_{x_{i-1}}^{x} \frac{\varepsilon(x)}{c(x)}\,dx\,dx}_{\substack{\text{Deflection increment}\\ \text{above } y_{i-1}}} + \underbrace{\int_{x_{i-1}}^{x} \tan\theta_{i-1}\,dx}_{\substack{\text{Deflection at } x\\ \text{due to } \tan\theta_{i-1}}} + \underbrace{y_{i-1}}_{\substack{\text{Deflection}\\ \text{at } x_{i-1}}}$$

$$(x_{i-1} \le x \le x_i) \quad (7)$$

in which $y_{i-1}$ is the deflection at the inboard strain-sensing station, $x_{i-1}$.

In light of the linearity assumptions of $\{c(x),\ \varepsilon(x)\}$ given by equations (4) and (5), respectively, equations (6) and (7) can now be integrated once and twice, respectively, to yield the indicial forms of the slope and deflection equations for each domain. These indicial equations are then combined to yield the final mathematical forms of the deflection equations expressed in terms of beam geometrical parameters and surface strains presented in the following section (refs. 4–5).

## Straight-Beam Deflection Equations

The deflection equations (integrations of equation (7)) previously developed for nonuniform, slightly nonuniform, and uniform straight cantilever beams, have the following mathematical forms (refs. 4–5):

1. For nonuniform straight cantilever beams ($c_i \ne c_{i-1}$) (derivations in ref. 5, Appendix A),

$$y_i = (\Delta l)^2 \sum_{j=1}^{i} \left\{ \left[2(i-j)+1\right] \frac{\varepsilon_{j-1}-\varepsilon_j}{2(c_{j-1}-c_j)} - \frac{\varepsilon_{j-1}c_j - \varepsilon_j c_{j-1}}{(c_{j-1}-c_j)^3} \left[ c_j \log\frac{c_j}{c_{j-1}} + (c_{j-1}-c_j) \right] \right\}$$

$$+ (\Delta l)^2 \sum_{j=1}^{i-1} (i-j) \left[ \frac{\varepsilon_{j-1}c_j - \varepsilon_j c_{j-1}}{(c_{j-1}-c_j)^2} \log\frac{c_j}{c_{j-1}} \right] + y_0 + (i)\Delta l \tan\theta_0 \quad ; \quad (i = 1, 2, 3, ..., n) \qquad (8)$$

2. For slightly nonuniform straight cantilever beams ($c_i / c_{i-1} \to 1$),

$$y_i = \frac{(\Delta l)^2}{6} \sum_{j=1}^{i} \frac{1}{c_{i-j}} \left\{ \left[ 3(2j-1) - (3j-2)\frac{c_{i-j+1}}{c_{i-j}} \right] \varepsilon_{i-j} + (3j-2)\varepsilon_{i-j+1} \right\} + y_0 + (i)\Delta l \tan\theta_0$$

$$(i = 1, 2, 3, \ldots, n) \quad (9)$$

which was obtained from equation (8) by expanding the logarithmic terms in the neighborhood of $c_i / c_{i-1} \approx 1$ (derivations in ref. 5, Appendix C).

3. For uniform straight cantilever beams ( $c_i = c_{i-1} = c$ ),

$$y_i = \frac{(\Delta l)^2}{6c}\left[(3i-1)\varepsilon_0 + 6\sum_{j=1}^{i-1}\left(i-j\right)\varepsilon_j + \varepsilon_i\right] + y_0 + (i)\Delta l \tan\theta_0 \quad ; \quad (i = 1,2,3,...,n) \tag{10}$$

which was obtained by grouping the terms after setting $c_i = c_{i-1} = c$ in equation (9) (derivations in ref. 4 and Appendix D of ref. 5).

In each of the deflection equations (8)–(10), the deflection, $y_i$, at the sensing station, $x_i$, is expressed in terms of the inboard beam half depths ( $c_0, c_1, c_2, ..., c_i$ ) and the associated inboard strains ( $\varepsilon_0, \varepsilon_1, \varepsilon_2, ..., \varepsilon_i$ ), including the values of $\{ c_i, \varepsilon_i \}$ at the strain-sensing station, $x_i$, where the deflection, $y_i$, is calculated. Because equations (8)–(10) contain no structural properties (they actually are contained implicitly in the strains), in the shape predictions of complex structures (for example, aircraft wings), one can avoid tedious computations of bending stiffness, *EI*, at different strain-sensing stations (cross sections). This feature is a characteristic of the Ko displacement theory.

## UNIFORM CANTILEVER STRAIGHT BEAMS

In this report, only the uniform beams ( $c_i = c_{i-1} = c$ = constant) are considered; therefore, only equation (10) is needed. To show the progression of the functional form of equation (10) with an increasing value of the index, *i*, deflection equation (10) is written out explicitly for different indices, *i* (strain-sensing station, $x_i$ ), as

$$y_1 = \frac{(\Delta l)^2}{6c}(2\varepsilon_0 + \varepsilon_1) + y_0 + \Delta l \tan\theta_0 \tag{10a}$$

$$y_2 = \frac{(\Delta l)^2}{6c}\left(5\varepsilon_0 + 6\varepsilon_1 + \varepsilon_2\right) + y_0 + 2\Delta l \tan\theta_0 \tag{10b}$$

$$y_3 = \frac{(\Delta l)^2}{6c}\left[8\varepsilon_0 + 6(2\varepsilon_1 + \varepsilon_2) + \varepsilon_3\right] + y_0 + 3\Delta l \tan\theta_0 \tag{10c}$$

$$y_4 = \frac{(\Delta l)^2}{6c}\left[11\varepsilon_0 + 6\left(3\varepsilon_1 + 2\varepsilon_2 + \varepsilon_3\right) + \varepsilon_4\right] + y_0 + 4(\Delta l)\tan\theta_0 \tag{10d}$$

$$y_5 = \frac{(\Delta l)^2}{6c}\left[14\varepsilon_0 + 6\left(4\varepsilon_1 + 3\varepsilon_2 + 2\varepsilon_3 + \varepsilon_4\right) + \varepsilon_5\right] + y_0 + 5(\Delta l)\tan\theta_0 \tag{10e}$$

$$y_6 = \frac{(\Delta l)^2}{6c}\left[17\varepsilon_0 + 6\left(5\varepsilon_1 + 4\varepsilon_2 + 3\varepsilon_3 + 2\varepsilon_4 + \varepsilon_5\right) + \varepsilon_6\right] + y_0 + 6(\Delta l)\tan\theta_0 \tag{10f}$$

$$y_7 = \frac{(\Delta l)^2}{6c}\left[20\varepsilon_0 + 6\left(6\varepsilon_1 + 5\varepsilon_2 + 4\varepsilon_3 + 3\varepsilon_4 + 2\varepsilon_5 + \varepsilon_6\right) + \varepsilon_7\right] + y_0 + 7(\Delta l)\tan\theta_0 \tag{10g}$$

$$y_8 = \frac{(\Delta l)^2}{6c}\left[23\varepsilon_0 + 6\left(7\varepsilon_1 + 6\varepsilon_2 + 5\varepsilon_3 + 4\varepsilon_4 + 3\varepsilon_5 + 2\varepsilon_6 + \varepsilon_7\right) + \varepsilon_8\right] + y_0 + 8(\Delta l)\tan\theta_0 \tag{10h}$$

……..

$$y_n = \frac{(\Delta l)^2}{6c}\left[(3n-1)\varepsilon_0 + 6\sum_{j=1}^{n-1}\left(n-j\right)\varepsilon_j + \varepsilon_n\right] + y_0 + n(\Delta l)\tan\theta_0 \tag{10i}$$

Equation (10) explicitly shows that the deflection, $y_i$, at the strain-sensing station, $x_i$, is obtained by summing up all the inboard strains ($\varepsilon_0, \varepsilon_1, \varepsilon_2, ..., \varepsilon_i$), including the strain, $\varepsilon_i$, at the current strain-sensing station, $x_i$. For the cantilever beam, both the deflection, $y_0$, and slope, $\tan\theta_0$, at the fixed end ($x = x_0 = 0$) in equation (10) are zero (that is, $y_0 = \tan\theta_0 = 0$). The terms, $y_0 + (i)\Delta l \tan\theta_0$, however, are purposely retained for completeness so that equation (10) can be extended to the deflection equations for the simply supported beam, for which the left-end deflection, $y_0$, is zero ($y_0 = 0$), but the left-end slope, $\tan\theta_0$, is nonzero ($\tan\theta_0 \neq 0$).

## TWO–POINT SUPPORTED STRAIGHT BEAMS

Deflection equation (10) for uniform cantilever beams also can be used for shape predictions of uniform two-point supported beams (simple beams). Depending on the support conditions, equation (10) can be used directly or with modifications.

### Left End Simply Supported

If the uniform two-point supported straight beam is simply supported at the left end (the right end may be either simply supported or clamped), the slope, $\tan\theta_0$, at the left support ($x = x_0 = 0$) is no longer zero ($\tan\theta_0 (\neq 0)$). Also, the unknown nonzero slope, $\tan\theta_0$, must be determined so that equation (10) can be modified for shape predictions of left-end simply supported beams.

Let $y_i^B$ be the deflection at the strain-sensing station, $x_i$, of the left-end simply supported straight beam. Then $y_i^B$ can be calculated from equation (10) ($y_i$ replaced by $y_i^B$) with the nonzero slope term, $\tan\theta_0 (\neq 0)$, retained:

$$y_i^B = \underbrace{\frac{(\Delta l)^2}{6c}\left[(3i-1)\varepsilon_0 + 6\sum_{j=1}^{i-1}\left(i-j\right)\varepsilon_j + \varepsilon_i\right]}_{\text{Cantilever beam deflection equation}} + i(\Delta l)\underbrace{\tan\theta_0}_{\text{Nonzero}} \quad ; \quad (i = 1,2,3,...,n) \tag{11}$$

By setting the deflection, $y_i^B$, at the right support ($x = x_n = l$) to zero (that is, $y_i^B = y_n^B = 0$), one can determine the unknown slope, $\tan\theta_0$, at the left support ($x_i = x_0 = 0$) from equation (11) as

$$\tan\theta_0 = -\frac{1}{n(\Delta l)} y_n \tag{12}$$

in which $y_n$ is the deflection at the right end of the beam ($x_i = x_n = l$) calculated from equation (10i), neglecting $\{ y_0 + (i)\Delta l \tan\theta_0 \}$ terms. Namely,

$$y_n \equiv \underbrace{\frac{(\Delta l)^2}{6c}\left[ (3n-1)\varepsilon_0 + 6\sum_{j=1}^{n-1}\left(n-j\right)\varepsilon_j + \varepsilon_n \right]}_{\substack{\text{Cantilever beam tip deflection (eq. (10i) neglecting} \\ \{y_0 + n(\Delta l)\tan\theta_0\} \text{ terms)}}} \tag{13}$$

In light of equation (12), deflection equation (11) for the left-end simply supported straight beam becomes

$$y_i^B = y_i - \underbrace{\frac{i}{n} y_n}_{\substack{\text{To enforce} \\ y_n^B = 0 \\ \text{at right} \\ \text{support} \\ (i = n)}} \quad ; \quad (i = 1,2,3,...,n) \tag{14}$$

in which $y_i$ is the cantilever beam deflection at the strain-sensing station, $x_i$, given by equation (10), setting $y_0 = 0$ and $\tan\theta_0 = 0$ (or from equation (13), setting the index $n = i$).

## Left End Clamped

If the uniform two-point supported straight beam is clamped at the left end (the right end can be either clamped or simply supported), the deflections, $y_i^B$, can be calculated from the cantilever-beam deflection equation (10) (replacing $y_i$ with $y_i^B$ and setting $y_0 = 0$ and $\tan\theta_0 = 0$) for the shape predictions (refs. 4–5). The calculated deflection, $y_n^B$, at the right support ideally should be zero ($y_n = 0$). If the calculated value of $y_n^B$ is not exactly zero ($y_n \neq 0$), however, and it has a small value, a correction term

must be added to equation (10) to enforce $y_n^B = 0$. To enforce $y_n^B = 0$ at the right end, and also to maintain a zero slope ( $\tan\theta_0 = 0$ ) at the clamped left end, equation (14) can be modified by squaring the second term as

$$y_i^B = y_i - \underbrace{\left(\frac{i}{n}\right)^2 y_n}_{\substack{\text{To enforce} \\ y_n^B = 0 \\ \text{at right support} \\ (i = n)}} \quad ; \quad (i = 1,2,3,...,n) \tag{15}$$

for the calculations of deflections, $y_i^B$, of the left-end clamped straight beam.

## BASICS OF CURVED BEAMS

The purpose of this section is to examine the deflection prediction errors involved in using the straight-beam deflection equation (10) for shape predictions of curved beams with different curvatures, and then to show how the prediction errors can be practically eliminated by introducing the curvature-effect correction terms to equation (10). Table 1 lists the geometrical parameters and associated bending stresses for different curved beams with rectangular cross sections (taken from ref. 10, p. 148).

Table 1. Curvature-related data for curved beams (ref. 10).

| $R/c$ | $k_{in}$ | $k_{out}$ | $\delta / R$ |
|---|---|---|---|
| 1.2 | 2.89 | 0.57 | 0.305 |
| 1.4 | 2.13 | 0.63 | 0.204 |
| 1.6 | 1.79 | 0.67 | 0.149 |
| 1.8 | 1.63 | 0.70 | 0.112 |
| 2.0 | 1.52 | 0.73 | 0.090 |
| 3.0 | 1.30 | 0.81 | 0.041 |
| 4.0 | 1.20 | 0.85 | 0.021 |
| 6.0 | 1.12 | 0.090 | 0.0093 |
| 8.0 | 1.09 | 0.92 | 0.0052 |
| 10.0 | 1.07 | 0.94 | 0.0033 |

In table 1, $\{R, c\}$ are the radius of curvature and the half depth of the uniform curved beam, respectively, $\delta$ is the neutral axis offset (distance between the neutral axis and centroidal axis) given by (ref. 10, p. 148; ref. 11, p. 183)

$$\delta = R - \frac{2c}{\ln\left(\frac{R+c}{R-c}\right)} \tag{16}$$

and $\{k_{in},\ k_{out}\}$ are the magnitudes of the normalized bending stresses on the concave and convex sides, respectively, of the curved beam defined as

$$k_{in} = \frac{\sigma_{in}}{\sigma} \tag{17}$$

$$k_{out} = \frac{\sigma_{out}}{\sigma} \tag{18}$$

in which $\{\sigma_{in}, \sigma_{out}\}$ are the magnitudes of the bending stresses on the concave and convex sides, respectively, and $\sigma$ is the magnitude of the surface bending stress of the equivalent straight beam.

The data listed in table 1 are plotted in figure 2. Note that the magnitude of the bending stress on the concave side ($k_{in}$) is larger than the magnitude of the bending stress on the convex side ($k_{out}$), and that the difference between $k_{in}$ and $k_{out}$ decreases as the radius of curvature factor, $R/c$, increases. Also notice that the neutral axis of the curved beam does not coincide with the centroidal axis, but it is shifted away from the centroidal axis toward the concave side by an offset distance, $\delta$. As shown in figure 2, the curvature effect gradually decreases with an increasing radius of curvature factor, $R/c$, and practically diminishes at approximately *R/c* = 17 ($\delta / R \approx 0.001$). In the region *R/c* >17, one observes that $k_{in} \approx k_{out}$ and $\delta \approx 0$, and the curved beam approaches the straight beam. Therefore, for the slightly curved beam with a radius of curvature factor, *R/c*, greater than 17 (*R/c* >17, fig. 2), the curved beam can be treated like a straight beam. Thus the straight-beam deflection equation (10) can be applied for shape predictions without introducing too many errors. The next section discusses the prediction errors of using the straight-beam deflection equation (10) for shape predictions of curved beams with different curvatures.

## BASICS OF ANALYTICAL SHAPE PREDICTIONS

The present shape prediction study of curved beams is called an analytical shape prediction study. Instead of using the strain data measured by fiber optics, the Structural Performance And Resizing (SPAR) finite-element computer program (ref. 12) was used to generate the surface bending strain data and beam deflection curves (to be used as reference deflection curves).

The bending strains, $\varepsilon_i$ (*i* = 0, 1, 2, 3,…, *n*), at the *i*-th strain sensors needed for deflection calculations (eq. (10)) were generated by converting the SPAR axial nodal stresses, $\sigma_i$ (*i* = 0, 1, 2, 3,…, *n*), at the *i*-th strain sensor point, into the bending strains, $\varepsilon_i$, through Hooke's law (that is, $\varepsilon_i = \sigma_i / E$), in which *E* is the Young's modulus. Alternatively, the bending strains, $\varepsilon_i$, can also be generated from the axial length changes of the SPAR elements where the bending strains, $\varepsilon_i$, are to be measured. This method was found to lose accuracy near the high slope regions of the deformed beam, however, and therefore was not used (ref. 4).

The bending strains generated by the SPAR program were then input to the straight-beam deflection equations to calculate the theoretical deflection curves for comparison with the corresponding SPAR deflection curves (used as reference). The prediction errors caused by curvature effect also were examined. The final mathematical functional forms for the curvature-effect correction terms were

determined when the trial deflection curves best fit the corresponding SPAR deflection curves. The curvature-effect correction terms thus determined were then introduced to the straight-beam deflection equations to formulate the curved-beam deflection equations.

## SHAPE PREDICTIONS OF CANTILEVER CURVED BEAMS

Before the straight-beam deflection equation (10) is applied to the shape predictions of cantilever curved beams, the prediction errors resulting from equation (10) first must be examined. For the prediction error studies, cantilever curved beams with different curvatures, listed in the next section, were analyzed.

### Geometry

Table 2 lists the dimensions of five types of cantilever curved beams (the straight cantilever beam is listed as a limit case) for the shape prediction error studies. All the cantilever curved beams considered have a unit width, an identical curved length of $l$ = 100 in., and an identical half depth of $c = h/2 = 0.25$ in. To maintain the same curved-beam length, the radius of curvature, $R$, was changed with the change of the curved-beam angle, $\phi_n$.

Table 2. Dimensions of cantilever curved beams analyzed; width = 1 in.

| $l$, in. | $\phi_n$, deg | $R$, in. | $h$, in. | $c$, in. | $R/c$ |
|---|---|---|---|---|---|
| 100 | 0.0 (straight) | ∞ | 0.50 | 0.25 | ∞ |
| 100 | 22.5 | 254.65 | 0.50 | 0.25 | 1,019 |
| 100 | 45.0 | 127.32 | 0.50 | 0.25 | 509 |
| 100 | 67.5 | 84.88 | 0.50 | 0.25 | 340 |
| 100 | 90.0 (1/4 circle) | 63.66 | 0.50 | 0.25 | 255 |

Based on the range of the radius of curvature factor, $R/c$, listed in table 2, the neutral axis offset, $\delta$, calculated from equation (16) was negligible (fig. 2). Therefore, the neutral axis offset effect was ignored in the shape prediction analysis.

Figure 3 shows the undeformed and deformed shapes, generated from the SPAR program, of a typical cantilever curved beam with an inward radial load of $P$ = 1 lb at the beam tip. There are $n + 1$ ($n$ = 8) equally spaced strain sensors ($i$ = 0, 1, 2, 3,…, $n$) installed on the lower surface of the beam, with the strain sensors (0, $n$) located at the fixed end ($x = x_0 = 0$) and at the free end ($x = x_n = l$), respectively.

Figure 4 shows the strain curves, generated from the SPAR program, for the cantilever curved beams with different curvatures. Note from figure 4 that as the curvature increases (that is, an increasing curved-beam angle, $\phi_n$), the strain curve near the left fixed end continues to bend further downward from the straight strain line of the straight beam ($\phi_n = 0$). Also note from figure 4 that all the strain curves for the cantilever curved beams have very small curvatures, and any segment of the strain curve between the two adjacent strain-sensing stations is very close to a straight line, reinforcing the assumption of piecewise linear distributions of bending strains (eq. (5)) used in the formulation of the Ko displacement theory (refs. 4–6). The piecewise linear strain curves will converge to the corresponding actual curvilinear strain curves (fig. 4) as the number of strain-sensing stations is increased. For the fiber-optic strain sensors, the

number of strain-sensing stations can be increased very easily at will by simply reducing the sensing intervals of the Bragg gratings along the optical fiber (refs. 1–3).

## Uncorrected Deflections

To use the straight-beam deflection equation (10) for shape predictions of a cantilever curved beam, the axial coordinate, $x$, will now represent the tangential coordinate, $x = R\phi$, of the curved beam, and $y$ will represent the radial displacement, which is considered positive when pointed inward. Because the radius of curvature factors, $R/c$ = 255–1,019 (table 2), are much greater than 17 (beyond which the curvature effect diminishes), the neutral axis and centroidal axis of the cantilever curved beams are almost coincidental (fig. 2). Therefore, when equation (10) was used, the half depth, $c$, was not modified, because the neutral axis offset, $\delta$, was practically zero ($\delta \approx 0$).

Figure 5 shows the deflection curves calculated for all the cantilever curved beams. The deflection curves calculated from equation (10) are represented by solid lines with solid circular symbols, and the deflection curves calculated from the SPAR program are represented by dotted lines with open circular symbols. Note that equation (10) overpredicts the curved-beam deflections calculated from the SPAR program, and the prediction error increases progressively with the increasing curved-beam angle, $\phi_n$. Namely, as the curvature increases (that is, increasing $\phi_n$), the deflection curve calculated from equation (10) continues to bend upward further away from the corresponding SPAR deflection curve (considered as the reference deflection curve).

## Shape Prediction Errors

Let $y_i^C$ ($i$ = 1, 2, 3, …, $n$) be the radial deflections calculated from the SPAR program (assumed to be the true radial deflections), and let $y_i$ ($i$ = 1, 2, 3, …, $n$) be the deflections calculated from the straight-beam deflection equation (10). Then the difference, $e_i (\equiv y_i - y_i^C)$, will be considered as the shape prediction error at the strain-sensing station, $x_i$. Table 3 lists the beam tip deflections, $\{y_n^C, y_n\}$ (maximum), of the cantilever curved beams together with the normalized beam tip shape prediction errors, $e_n \big/ y_n^C$, for different cantilever curved beams. Note that the prediction error, $e_n \big/ y_n^C$, at the curved-beam tip based on the straight-beam deflection equation (10) increases progressively with the increase in the curved-beam angle $\phi_n$, and reaches a maximum of 26.6437 percent at $\phi_n$ = 90° for a quarter-circle beam.

Table 3. Comparison of beam tip deflections calculated from SPAR with those calculated from straight-beam deflection equation (10) for different cantilever curved beams; $l$ = 100 in.; $c$ = 0.25 in.; $P$ = 1 lb; $n$ = 8.

| $\phi_n$, deg | $y_n^C$, in. (SPAR) | $y_n$, in. (eq. (10)) | $e_n / y_n^C \times 100\%$ (eq. (10) prediction error) |
|---|---|---|---|
| 0.0 (straight) | 9.4714 | 9.4793 | 0.0834 |
| 22.5 | 9.1834 | 9.3209 | 1.4951 |
| 45.0 | 8.3693 | 8.8805 | 6.1000 |
| 67.5 | 7.1645 | 8.1891 | 14.3011 |
| 90.0 (1/4 circle) | 5.7582 | 7.2924 | 26.6437* |

*Peak prediction error.

## Curvature-Effect Corrections

To reduce (or eliminate) the prediction errors from using the straight-beam deflection equation (10) for shape predictions of cantilever curved beams, a curvature-effect correction term must be introduced to modify equation (10). A trial mathematical function for the curvature-effect correction term was added to equation (10) to calculate the corrected deflection curve for each cantilever curved beam, which was then compared with the corresponding SPAR deflection curve (used as reference). After extensive searching, the most accurate mathematical functional form for the curvature-effect correction term was introduced to equation (10) to formulate the following modified deflection equation for calculations of deflections, $\hat{y}_i$ ($i$ = 1, 2, 3, …, $n$), of the cantilever curved beams (established September 24, 2008). For $0 \le \phi_n \le 90°$ arcs,

$$\hat{y}_i = y_i - \underbrace{\frac{1}{4.5}\left(\frac{\phi_n}{90}\right)^2\left(\frac{i}{n}\right)^4 y_n}_{\text{Curvature-effect correction term}} \quad ; \quad (i = 1,2,3,...,n) \tag{19}$$

in which $y_i$ ($i$ =1, 2, 3, …, $n$) is to be calculated from the cantilever straight-beam deflection equation (10) (setting $y_0 + (i)\Delta l \tan\theta_0 = 0$). Equation (19) is called the cantilever curved-beam deflection equation and is applicable for the whole range ($0 \le \phi_n \le 90°$) of cantilever curved beams analyzed, including the special case of a straight beam ($\phi_n = 0°$), for which the curvature-effect correction term vanishes (that is, $\hat{y}_i = y_i$).

## Corrected Deflections

The corrected deflection curves calculated from the cantilever curved-beam deflection equation (19) are plotted in figure 6 for different curved beams. Note that the predicted deflection curves practically match the corresponding SPAR deflection curves, with pictorially inconspicuous prediction errors. This good agreement confirms the accuracy of the newly developed cantilever curved-beam deflection equation (19) for shape predictions of a whole range ($0 \le \phi_n \le 90°$) of cantilever curved beams analyzed.

### Reduced Shape Prediction Errors

Table 4 lists the corrected beam tip deflections, $\hat{y}_n$, together with the reduced prediction errors, $\hat{e}_n(\equiv \hat{y}_n - y_n^C)$. The uncorrected beam tip deflections, $y_n$, calculated from equation (10) and the associated prediction errors, $e_n(\equiv y_n - y_n^C)$, taken from table 3 also are listed for comparison. Note that the corrected beam tip deflection errors, $\hat{e}_n \big/ y_n^C$, are merely 0.0849–1.4987 percent, which are almost negligible compared with the uncorrected beam tip deflection errors of $e_n \big/ y_n^C$ of 1.4951–26.6437 percent.

Table 4. Comparison of curved-beam tip deflections calculated from SPAR with those calculated from deflection equations (10) and (19) for different cantilever curved beams; $l$ = 100 in.; $c$ = 0.25 in.; $P$ = 1 lb; $n$ = 8.

| $\phi_n$, deg | $y_n^C$, in. (SPAR) | $y_n$, in. (eq. (10)) | $e_n / y_n^C \times 100\%$ (eq. (10) prediction error) | $\hat{y}_n$ (eq. (19)) | $\hat{e}_n / y_n^C \times 100\%$ (eq. (19) prediction error) |
|---|---|---|---|---|---|
| 0.0 | 9.4714 | 9.4793 | 0.0834 | 9.4793 | 0.0834 |
| 22.5 | 9.1836 | 9.3209 | 1.4951 | 9.1914 | 0.0849 |
| 45.0 | 8.3693 | 8.8805 | 6.100 | 8.3871 | 0.2127 |
| 67.5 | 7.1645 | 8.1891 | 14.3011 | 7.1654 | 0.0126 |
| 90.0 | 5.7582 | 7.2924 | 26.6437 | 5.6719 | 1.4987 |

For easy visualization, figure 7 shows the uncorrected and corrected curved-beam tip deflection prediction errors $\{e_n \big/ y_n^C, \hat{e}_n / y_n^C\}$ plotted as functions of the curved-beam angle, $\phi_n$, based on the data of table 4. Note that the prediction errors of using equation (10) increases progressively with increasing $\phi_n$. With curvature-effect corrections (eq. (19)), the beam tip prediction error curve is nearly a horizontal line because of a negligible error range (table 4).

## SHAPE PREDICTIONS OF TWO–POINT SUPPORTED CURVED BEAMS

The straight-beam deflection equations (14) and (15) may be reasonably accurate for shape predictions of simply supported and clamped shallow curved beams, respectively. For shape predictions of deeper curved beams, however, equations (14) and (15) could lose prediction accuracy. Therefore, curvature-effect correction terms are needed to modify both equations (14) and (15). The mathematical functional forms for the curvature-effect correction terms were determined with the aid of SPAR finite-element analysis of different two-point supported curved beams listed in the next section.

### Geometry

Table 5 lists the dimensions of the two-point supported curved beams that were analyzed for establishing the mathematical functional forms of the curvature-effect correction terms. All the two-point supported curved beams that were analyzed have a unit width, an identical curved length of $l$ = 200 in., and an identical half depth of $c = h/2$ = 0.25 in. To maintain the same curved-beam length, the radius of curvature, $R$, was changed with the change of the curved-beam angle, $\phi_n$. For the range of radius of

curvature factor, *R/c*, listed in table 5, the neutral axis offset factor, $\delta / R$, is practically zero according to the $\delta / R$ curve of figure 2.

Table 5. Dimensions of two-point supported curved beams; width = 1 in.

| *l*, in. | $\phi_n$, deg | *R*, in. | *h*, in. | *c*, in. | *R/c* |
|---|---|---|---|---|---|
| 200 | 0 (straight) | ∞ | 0.50 | 0.25 | ∞ |
| 200 | 45 | 254.65 | 0.50 | 0.25 | 1,019 |
| 200 | 90 (1/4 circle) | 127.32 | 0.50 | 0.25 | 509 |
| 200 | 135 | 84.88 | 0.50 | 0.25 | 340 |
| 200 | 180 (1/2 circle) | 63.66 | 0.50 | 0.25 | 255 |
| 200 | 225 | 50.93 | 0.50 | 0.25 | 204 |
| 200 | 270 (3/4 circle) | 42.44 | 0.50 | 0.25 | 170 |
| 200 | 315 | 36.38 | 0.50 | 0.25 | 146 |
| 200 | 360 (full circle) | 31.83 | 0.50 | 0.25 | 127 |

Figure 8 shows a typical two-point supported curved beam under two types of support conditions: (1) both ends clamped, and (2) both ends simply supported. Each two-point supported curved beam was subjected to an upward (inward) radial force of $P$ = 2 lb at the curved beam midpoint. As shown in figure 8, $n + 1$ ($n$ = 16) equally spaced strain sensors were installed along the outer surface of the curved beam. The corresponding strain-sensing stations (not shown) for the inner surfaces of the curved beam also are needed so that the outer and inner strains at the same beam cross sections can be averaged to eliminate possible axial strain components caused by beam curvature and support constraints.

## Curvature-Effect Corrections

For shape predictions of curved beams, the straight-beam equation (14) (for both ends simply supported) or equation (15) (for both ends clamped) will generate too many prediction errors when the beam curvature increases. Therefore, the curvature-effect correction terms must be introduced to equations (14) and (15) to formulate the modified deflection equations for shape predictions of two-point supported curved beams.

The mathematical functional forms for the curvature-effect correction terms were extensively searched with the aid of the SPAR computer program. Namely, the SPAR program was used to generate both the bending strains and deflection curves of various two-point supported curved beams. The SPAR bending strains were then input to the straight-beam deflection equation (14) (for both ends simply supported) or equation (15) (for both ends clamped) to calculate the respective predicted deflection curves for comparison with the corresponding SPAR deflection curves (considered as reference deflection curves). The curvature correction terms expressed in trial mathematical functional forms were added to equation (14) or (15) to improve the curved-beam shape predictions. The curvature correction mathematical functional forms were continually modified until the predicted deflection curves converged toward the corresponding SPAR deflection curves. The reformulated equation (14) or (15) containing the final forms of the curvature-effect correction terms were then considered as the deflection equations for the two-point supported curved beams.

## Both Ends Clamped

Figure 9 shows the deformed shapes, generated from the SPAR program, of various clamped curved beams including the straight beam ($0 \le \phi_n \le 360°$), each of which was subjected to an upward central force of $P$ = 2 lb. Note that in the range of $45 \le \phi_n \le 270°$, the central regions of the curved beams caved in, but both the left and right regions buckled out because of stationary supports. The central inward bending diminished for the curved-beam angles, $\phi_n$ = 315° and $\phi_n$ = 360°.

### Strain Curves

Figure 10 shows the strain curves, generated from the SPAR program, for various clamped curved beams including the straight beam ($0 \le \phi_n \le 360°$). The strain curve for the clamped straight beam ($\phi_n$ = 0) has the classical V-shape consisting of two inclined straight lines. The strain curves for the clamped curved beams, however, have a rounded M-shape and stay quite close. Slight strain differences are visible in the two submit regions, and the strain curves fan out toward the left and right supports.

### Deflection Equations

After the mathematical functions were searched extensively for the best curvature-effect correction terms in light of the SPAR deflection curves, the modified deflection equations were formulated for calculations of the deflections, $\hat{y}_i^B$ ($i$ =1, 2, 3, …, $n$), of the clamped curved beams with curved-beam angles up to $\phi_n$ = 360° (complete circle). The modified deflection equations for the whole range ($0 \le \phi_n \le 360°$) of clamped curved beams are presented in the next paragraph. For completeness, the degenerated deflection equation for the clamped straight beam is written out separately.

For $\phi_n$ = 0° (straight beam),

$$\hat{y}_i^B \equiv y_i^B = y_i - \underbrace{\left(\frac{i}{n}\right)^2 y_n}_{\substack{\text{To enforce} \\ \hat{y}_n^B = 0 \text{ at} \\ \text{right support} \\ (i = n).}} \quad ; \quad (i = 1,2,3,...,n) \tag{20a}$$

For $0 \le \phi_n \le 225°$ arcs (established July 14, 2008) (Chino Hills earthquake, July 29, 2008, 11:40 a.m., scale 5.4),

$$\hat{y}_i^B = y_i - \underbrace{\left[\left(\frac{i}{n}\right)^2 + \frac{4}{\pi}\left(\frac{\phi_n}{360}\right)^2 \sin^4\left(\frac{i}{n}\pi\right)\right] y_n}_{\substack{\text{Correction term to enforce } \hat{y}_n^B = 0 \text{ at} \\ \text{right support } (i = n).}} \quad ; \quad (i = 1,2,3,...,n) \tag{20b}$$

For $225 < \phi_n \le 360°$ arcs (established July 17, 2008),

$$\hat{y}_i^B = y_i - \underbrace{\left[\left(\frac{i}{n}\right)^2 + 2.25\left(\frac{\phi_n}{360}\right)^3 \sin^4\left(\frac{i}{n}\pi\right)\right] y_n}_{\text{Correction term to enforce } \hat{y}_n^B = 0 \text{ at right support } (i = n).} \quad ; \quad (i = 1,2,3,...,n) \tag{20c}$$

In equation (20), $y_i$ is the deflection of the cantilever straight beam given by equation (10) (setting $y_0 = 0$ and $\tan\theta_0 = 0$). Note that the functional forms of the curvature-effect correction terms are slightly different for different ranges of the curved-beam angle, $\phi_n$. For shape predictions of the clamped curved-beam case, only two deflection equations are needed to cover the whole range of curved-beam angles ($0 \le \phi_n \le 360°$).

In equations (20b–c), the first correction term, $(i/n)^2$, within the brackets is to cause the $\hat{y}_i^B = y_i$ curve to rotate with respect to the left support point to nullify the deflection at the right support (that is, $\hat{y}_n^B = 0$), thereby causing the left and right regions of the rotated theoretical deflection curve to fit the corresponding regions of the SPAR deflection curve. The second correction term with a sine function (eqs. (20b–c)) is to bend the central region of the rotated theoretical deflection curves upward to match the corresponding central regions of the SPAR deflection curves as shown in the following section.

**Deflection Curves**

The strain data generated from the SPAR program (fig. 10) were input to the clamped curved-beam deflection equation (20) to generate the theoretical deflection curves. Figure 11 shows the deflection curves generated from the SPAR program compared with the theoretical deflections curves calculated from the straight-beam deflection equations (10) and (15), and also from the modified deflection equation (20), for the whole range of curved-beam angles ($0 \le \phi_n \le 360°$).

For the straight beam ($\phi_n = 0$, fig. 11a), the deflection curves, $y_i^B = y_i$ (cantilever straight-beam deflection equation (10)) and $y_i^B = y_i - (i/n)^2 y_n$ (clamped straight-beam deflection equation (19a)), agree quite nicely with the SPAR deflection curve. Equation (10) ($y_i^B = y_i$), however, gives a pictorially inconspicuous nonzero deflection of $y_n = 0.014285$ in. at the right end. Keep in mind that the term, $(i/n)^2 y_n$, in the deflection equation, $y_i^B = y_i - (i/n)^2 y_n$, is to rotate (with slight distortions) the $y_i^B = y_i$ curve (eq. (10)), with respect to the left support, to nullify the right-end deflection, $\hat{y}_n^B$, of the clamped straight beam (that is, to set $\hat{y}_n^B = 0$). For the curved beams (figs. 11b–i), the deflection curves, $y_i^B = y_i$ (eq. (10)), produce marked prediction errors (in the range of $y_n$ = –0.10952 to –0.15475) at the right ends of the beam because of the curvature effect. With the term, $(i/n)^2 y_n$, included, the

$y_i^B = y_i - (i/n)^2 y_n$ curve (eq. (20a)) compares nicely with the corresponding SPAR deflection curve for the curved-beam angle, $\phi_n$ = 45° (fig. 11b). For curved-beam angles, $\phi_n \geq 90°$ (figs. 11c–i), however, the $y_i^B = y_i - (i/n)^2 y_n$ curve can fit only the regions near both ends of the corresponding SPAR deflection curve, and the central region of the $y_i^B = y_i - (i/n)^2 y_n$ curve starts to diverge from the corresponding SPAR curve as $\phi_n$ increases, and reaches a maximum level at $\phi_n$ = 360°. When the sine function correction terms (eqs. (20b–c)) are introduced, the central region of each final theoretical deflection curve can be bent upward to converge toward the central region of the corresponding SPAR deflection curve (figs. 11b–i).

## Both Ends Simply Supported

Figure 12 shows the deformed shapes, generated from the SPAR program, of various simply supported curved beams including the straight beam ($0 \leq \phi_n \leq 360°$), each of which was subjected to an upward central force of $P$ = 2 lb. Similar to the clamped curved beams (fig. (9)), for the simply supported curved beams with the curved-beam angle, $45 \leq \phi_n \leq 270°$, the central region of the curved beam bent inward, but both the left and right regions bulged out because of stationary supports. For the curved-beam angles, $\phi_n$ = 315° and $\phi_n$ = 360°, both the left and right regions bulged out because of stationary supports, but the central region did not cave in.

### Strain Curves

Figure 13 shows the strain curves, generated from the SPAR program, for different simply supported curved beams with a whole range of curved-beam angles ($\phi_n$ = 0–360°). The strain curve for the straight beam ($\phi_n$ = 0) again has the classical V-shape, consisting of two inclined straight lines. The strain curves for the curved beams, however, have a rounded M-shape and are very similar. Slight differences in the strain curves are magnified in the left and right summit regions.

### Deflection Equations

The strain data generated from the SPAR program (fig. 13) were used to calculate the theoretical deflection curves for comparison with the corresponding reference SPAR deflection curves. After mathematical functions were searched extensively for the curvature-effect correction terms in light of the reference SPAR deflection curves, modified deflection equations were established for calculations of deflections, $\hat{y}_i^B$ ($i$ =1, 2, 3, …, $n$), of simply supported curved beams with a whole range of curved-beam angles ($0 \leq \phi_n \leq 360°$). The modified deflection equations for simply supported curved beams are presented in this section. For completeness, the deflection equation for the simply supported straight-beam case ($\phi_n$ = 0°) is written out separately.

For $\phi_n = 0°$ (straight-beam case),

$$\hat{y}_i^B \equiv y_i^B = y_i - \underbrace{\frac{i}{n} y_n}_{\substack{\text{To enforce} \\ y_n^B = 0 \text{ at} \\ \text{right support} \\ (i = n)}} \quad ; \quad (i = 1, 2, 3, ..., n) \tag{21a}$$

For $\phi_n = 45°$ arc,

$$\hat{y}_i^B = y_i - \underbrace{\left[ \frac{i}{n} + \left( \frac{\phi_n}{360} \right)^2 \sin\left( \frac{i}{n} \pi \right) \right] y_n}_{\substack{\text{Correction term to enforce } \hat{y}_n^B = 0 \\ \text{at right support } (i = n).}} \quad ; \quad (i = 1, 2, 3, ..., n) \tag{21b}$$

For $\phi_n = 90°$ arc,

$$\hat{y}_i^B = y_i - \underbrace{\left[ \frac{i}{n} + \frac{1}{\pi} \left( \frac{\phi_n}{360} \right)^3 \sin\left( \frac{i}{n} \pi \right) \right] y_n}_{\substack{\text{Correction term to enforce } \hat{y}_n^B = 0 \\ \text{at right support } (i = n).}} \quad ; \quad (i = 1, 2, 3, ..., n) \tag{21c}$$

For $135 \le \phi_n \le 225°$ arcs,

$$\hat{y}_i^B = y_i - \underbrace{\left[ \frac{i}{n} - \frac{1}{\pi} \left( \frac{\phi_n}{360} \right)^3 \sin^4\left( \frac{i}{n} \pi \right) \right] y_n}_{\substack{\text{Correction term to enforce } \hat{y}_n^B = 0 \\ \text{at right support } (i = n).}} \quad ; \quad (i = 1, 2, 3, ..., n) \tag{21d}$$

For $\phi_n = 270°$ arc,

$$\hat{y}_i^B = y_i - \underbrace{\left[ \frac{i}{n} - \frac{0.9}{\pi} \left( \frac{\phi_n}{360} \right)^3 \sin^4\left( \frac{i}{n} \pi \right) \right] y_n}_{\substack{\text{Correction term to enforce } \hat{y}_n^B = 0 \\ \text{at right support } (i = n).}} \quad ; \quad (i = 1, 2, 3, ..., n) \tag{21e}$$

For $\phi_n = 315°$ arc,

$$\hat{y}_i^B = y_i - \underbrace{\left[\frac{i}{n} - \frac{0.8}{\pi}\left(\frac{\phi_n}{360}\right)^3 \sin^3\left(\frac{i}{n}\pi\right)\right] y_n}_{\text{Correction term to enforce } \hat{y}_n^B = 0 \text{ at right support } (i = n).} \quad ; \quad (i = 1,2,3,...,n) \tag{21f}$$

For $\phi_n = 360°$ ring,

$$\hat{y}_i^B = y_i - \underbrace{\left[\frac{i}{n} - \frac{0.7}{\pi}\left(\frac{\phi_n}{360}\right)^3 \sin^3\left(\frac{i}{n}\pi\right)\right] y_n}_{\text{Correction term to enforce } \hat{y}_n^B = 0 \text{ at right support } (i = n).} \quad ; \quad (i = 1,2,3,...,n) \tag{21g}$$

Note that six different deflection equations are needed for the simply supported curved beams to cover the whole range of curved-beam angles ($0 \le \phi_n \le 360°$). Remember that for the clamped curved beams, only two deflection equations are needed to cover the whole range of curved-beam angles ($0 \le \phi_n \le 360°$).

**Deflection Curves**

Figure 14a shows the deflection curve, $\hat{y}_i^B = y_i^B = y_i - (i/n) y_n$, for the simply supported straight beam (eq. (21a)) compared with the deflection curve generated from the SPAR program. The two deflection curves are extremely close, showing the prediction accuracy of equation (21a). Figures 14b–i compare the theoretical and SPAR deflection curves for the curved-beam angles, $\phi_n$ = 45–360°. For the simply supported curved beams, the deflection curves, $\hat{y}_i^B = y_i^B = y_i - (i/n) y_n$, calculated from the straight-beam equation (21a) are fairly close to the corresponding SPAR deflection curves up to $\phi_n$ = 135°, and the prediction error (underprediction) gradually increases with increasing $\phi_n$, reaching a maximum at $\phi_n$ = 360°.

Remember that the term, $(i/n)y_n$, in the deflection equation, $\hat{y}_i^B = y_i^B = y_i - (i/n) y_n$ (eq. (21a)), is to shift the $\hat{y}_i^B = y_i$ curve upward proportionally with respect to the left support point to bring the right support deflection, $\hat{y}_n^B$, to zero ($\hat{y}_n^B = 0$). For curved beams, this shift causes the $\hat{y}_i^B = y_i^B = y_i - (i/n) y_n$ curves to fit only the left and right regions of the corresponding SPAR deflection curves. The central regions remain to be corrected. When the sine correction terms (eqs. (21b–g)) are added, the central regions of the final deflection curves could be bent upward to fit the central regions of the corresponding SPAR deflection curves quite well.

## GENERIC CREW EXPLORATION VEHICLE CURVED STRUCTURES

The new deflection equations developed for cantilever curved beams (eq. (19)) and for two-point supported curved beams (eqs. (20) and (21)) will now be applied to shape predictions of the generic crew exploration vehicle (CEV) curved structures. As shown in figure 15, the windward shallow spherical wall of the generic CEV is fabricated with dual honeycomb sandwich walls (exterior composite wall and interior aluminum wall). Both walls have an identical depth of $2c$ = 0.5 in. and are separated by a 2-in. gap. The exterior wall region chosen for the shape prediction analysis has a radius of curvature of $R$ = 245.75 in., and subtends an azimuth angle of 22°, which excludes the rounded toroidal shoulder regions. The shape predictions of the CEV outer shell (with the thermal protection system removed) can start from the shape predictions of the CEV curved beam embedded in the exterior wall of the CEV. Two types of CEV curved beams were analyzed: (1) cantilever curved beam, and (2) two-point supported curved beam.

## SHAPE PREDICTIONS OF CREW EXPLORATION VEHICLE CANTILEVER CURVED BEAMS

Figure 16 shows the SPAR model of the CEV cantilever curved beam, which is a cutout of the generic CEV windward exterior wall along its radius (fig. 15). An inward radial load of $P$ = 1 lb is applied at the beam tip. There are $n$ + 1 ($n$ = 8) equally spaced strain sensors ($i$ = 0, 1, 2, 3,…, $n$) (fig. 16) designated on the lower surface of the CEV cantilever curved beam, with strain sensors (0, $n$) located at the fixed end ( $x = x_0 = 0$ ) and at the free end ( $x = x_n = l$ ), respectively.

The CEV cantilever curved beam has a curved length of $l$ = 94.36 in., a curved-beam angle of $\phi_n$ = 22°, and a unit width. Table 6 provides the complete dimensions of the CEV cantilever curved beam, including the dimensions of an equivalent cantilever straight beam (same length, depth, and width as the CEV cantilever curved beam).

Table 6. Dimensions of CEV cantilever curved beam and equivalent straight beam.

| Beam | $l$, in. | $\phi_n$, deg | $R$, in. | $h$, in. | $c$, in. |
|---|---|---|---|---|---|
| CEV cantilever | 94.3612 | 22.0 | 254.75 | 0.50 | 0.25 |
| Equivalent straight | 94.3612 | 0.0 | ∞ | 0.50 | 0.25 |

Based on the geometrical data provided in table 6, the radius of curvature factor, $R/c$, for the CEV curved beam is $R/c = 983$, which is far greater than the curvature-effect limit of $R/c$ = 17 (fig. 2), beyond which the curvature effect diminishes. Thus in light of figure 2, the CEV curved beam can be classified as a very shallow curved beam.

Also based on the data in table 6, the neutral axis offset, $\delta$, of the CEV curved beam was calculated from equation (16) to be $\delta$ = 0.049754 in., which gives the normalized neutral axis offset of $\delta/R$ = 0.000202. This value is far too small to appear in table 1. Thus the neutral axis of the CEV curved beam is practically coincidental with the centroidal axis (see fig. 2). Therefore, in the calculations of theoretical deflection curves, the neutral axis offset effect was neglected.

## Strain Curves

Figure 17 shows the curves for the bending strains, $\varepsilon_i$, generated from the SPAR program, for the lower surface of the CEV cantilever curved beam and the equivalent straight beam. The strain curve for the CEV cantilever curved beam is very close to that of the equivalent straight beam, for which the strain curve is a straight line with maximum strain at the built-in end and tapering down to zero at the beam tip.

## Deflection Curves

The strain data, generated from the SPAR program, of figure 17 were used as inputs to the cantilever curved-beam deflection equation (19) for deflection calculations for the CEV cantilever curved beam. Table 7 compares the calculated deflections with the deflections generated from the SPAR program for the CEV cantilever curved beam.

Table 7. Comparison of deflections calculated from SPAR with those calculated from curved-beam deflection equation (19) for the CEV cantilever curved beam.

| $\hat{y}_i^B$ | $\hat{y}_0^B$ (fixed end) | $\hat{y}_1^B$ | $\hat{y}_2^B$ | $\hat{y}_3^B$ | $\hat{y}_4^B$ | $\hat{y}_5^B$ | $\hat{y}_6^B$ | $\hat{y}_7^B$ | $\hat{y}_8^B$ (free end) |
|---|---|---|---|---|---|---|---|---|---|
| SPAR | 0.0000 | 0.1747 | 0.6687 | 1.4375 | 2.4335 | 3.6096 | 4.9166 | 6.3055 | 7.7265 |
| Eq. (19), curved | 0.0000 | 0.1743 | 0.6675 | 1.4343 | 2.4289 | 3.5986 | 4.9171 | 6.3183 | 7.7624 |
| Difference, percent | 0.0000 | 0.2290 | 0.1795 | 0.2225 | 0.1890 | 0.3047 | 0.0102 | 0.2030 | 0.4646 |

For the prediction error comparison, table 8 compares the deflections calculated from the straight-beam deflection equation (10) with those calculated from the SPAR program for the equivalent cantilever straight beam.

Table 8. Comparison of deflections calculated from SPAR with those calculated from straight-beam deflection equation (10) for the equivalent straight cantilever beam.

| $y_i$ | $y_0$ (fixed end) | $y_1$ | $y_2$ | $y_3$ | $y_4$ | $y_5$ | $y_6$ | $y_7$ | $y_8$ (free end) |
|---|---|---|---|---|---|---|---|---|---|
| SPAR | 0.0000 | 0.1787 | 0.6834 | 1.4684 | 2.4863 | 3.6910 | 5.0355 | 6.4734 | 7.9578 |
| Eq. (10), straight | 0.0000 | 0.1788 | 0.6841 | 1.4694 | 2.4881 | 3.6934 | 5.0388 | 6.4776 | 7.9631 |
| Difference, percent | 0.0000 | 0.0560 | 0.1024 | 0.0681 | 0.0724 | 0.0650 | 0.0655 | 0.0649 | 0.0666 |

Note from table 7 that based on the cantilever curved-beam deflection equation (19), the prediction error at the tip of the CEV cantilever curved beam is only 0.4646 percent. For the equivalent straight cantilever beam (table 8), the prediction error at the beam tip based on equation (10) is even smaller, in the amount of 0.0666 percent.

The deflection data of tables 7 and 8 are plotted in figure 18 for visual comparison. The deflection curves, calculated from the cantilever curved-beam deflection equation (19) and from the straight-beam deflection equation (10), fall practically on top of the corresponding SPAR deflection curves. The small number of prediction errors listed in tables 7 and 8 are pictorially inconspicuous in figure 18. The excellent agreement between the theoretical deflection curves and the corresponding SPAR deflection curves validates the high accuracy of both the cantilever curved-beam deflection equation (19) and the cantilever straight-beam deflection equation (10).

# SHAPE PREDICTIONS OF CREW EXPLORATION VEHICLE TWO–POINT SUPPORTED CURVED BEAMS

Figure 19 shows the CEV two-point supported curved beam, which is a cutout of the generic CEV windward exterior wall along its diameter (rounded shoulder regions excluded). The CEV two-point supported curved beam is a union of the CEV cantilever curved beam and its mirror image. An inward radial load of $P$ = 2 lb is applied at the beam center (symmetrical loading condition). The CEV two-point supported curved beam has a curved length of $l$ = 188.72 in., which subtends a curved-beam angle of $\phi_n = 44°$, and has a unit width. Table 9 provides the complete dimensions of the CEV two-point supported curved beam and an equivalent straight beam (same length and depth as the CEV curved beam).

Table 9. Dimensions of CEV two-point supported curved beam and equivalent straight beam.

| Beam | $l$, in. | $\phi_n$, deg | $R$, in. | $h$, in. | $c$, in. |
|---|---|---|---|---|---|
| CEV full | 188.72 | 44.0 | 254.75 | 0.50 | 0.25 |
| Straight | 188.72 | 0.0 | ∞ | 0.50 | 0.25 |

There are $n$ + 1 ($n$ = 16) equally spaced strain sensors ($i$ = 0, 1, 2, 3, …, $n$) installed on the curved-beam convex surface. The corresponding strain-sensing stations (not shown) for the curved-beam concave surface also are needed so that a pair of the convex and concave surface strains can be averaged to eliminate possible axial strain components caused by beam curvature and stationary supports.

In the shape prediction analysis of the CEV two-point supported curved beam, the following four types of support conditions were considered (fig. 19):

1. Both ends clamped and free to move along beam curve (CC-free)
2. Both ends clamped and stationary (CC-fixed)
3. Both ends simply supported and free to move along beam curve (SS-free)
4. Both ends simply supported and stationary (SS-fixed)

As discussed previously, the neutral axis of the CEV curved beam is practically coincidental with the centroidal axis (that is, $\delta \approx 0$, fig. 2). Therefore, like the CEV cantilever curved-beam case, the neutral axis offset effect was ignored in the calculations of theoretical deflection curves of the CEV two-point supported curved beam.

## Both Ends Clamped

Figure 20 shows the deformed shapes of the CEV clamped curved beam subjected to an inward radial central force of $P$ = 2 lb. For the CC-free case (fig. 20a), the deformed shape is slightly wavy, because the supports are allowed to move tangentially. For the CC-fixed case (fig. 20b), the deformed shape is wavier because of stationary support constraints.

Because the CEV curved-beam angle, $\phi_n$ = 44°, falls within the range, $0 \le \phi_n \le 225°$, the clamped curved-beam deflection equation (20b) was used for the shape predictions of the CEV curved beam with both CC-free and CC-fixed support conditions. Equation (20b) is rewritten as

$$\hat{y}_i^B = y_i - \underbrace{\left[\left(\frac{i}{n}\right)^2 + \frac{4}{\pi}\left(\frac{\phi_n}{360}\right)^2 \sin^4\left(\frac{i}{n}\pi\right)\right] y_n}_{\text{Correction term to enforce } \hat{y}_n^B = 0 \text{ at right support } (i = n).} \quad ; \quad (i = 1,2,3,...,n) \tag{22}$$

**Case of Both Ends Clamped and Free to Move Along Beam Curve (CC-Free)**

Figure 21 shows the strains, $\varepsilon_i$, generated from the SPAR program, for the CEV two-point supported curved beam and the equivalent straight beam under the CC-free support condition. The two strain curves are V-shaped and very close, indicating that the CEV curved beam behaves almost like a straight beam under the CC-free support condition. The strain data, generated from the SPAR program, of figure 21 were used to calculate the deflections for the CEV CC-free curved beam and CC-free equivalent straight beam using deflection equations (22) and (10), respectively. Table 10 compares the deflections calculated from the SPAR program with those calculated from the curved-beam deflection equation (22) for the CEV CC-free curved beam.

Table 10. Comparison of deflections calculated from SPAR with those calculated from deflection equation (22) for the CEV CC-free curved beam.

| $\hat{y}_i^B$ | $\hat{y}_0^B$ (left end) | $\hat{y}_1^B$ | $\hat{y}_2^B$ | $\hat{y}_3^B$ | $\hat{y}_4^B$ | $\hat{y}_5^B$ | $\hat{y}_6^B$ | $\hat{y}_7^B$ | $\hat{y}_8^B$ (center) |
|---|---|---|---|---|---|---|---|---|---|
| SPAR | 0.0000 | 0.0882 | 0.3150 | 0.6351 | 1.0021 | 1.3693 | 1.6898 | 1.9164 | 2.0025 |
| Eq. (22), curved | 0.0000 | 0.0838 | 0.3056 | 0.6200 | 0.9812 | 1.3427 | 1.6581 | 1.8811 | 1.9655 |
| Difference, percent | 0.0000 | 4.9887 | 2.9841 | 2.3776 | 2.0856 | 1.9426 | 1.8760 | 1.8420 | 1.8477 |

|<----------Left half of CEV CC-free curved beam---------->

Table 11 compares the deflections calculated from the SPAR program with those calculated from the straight-beam deflection equation (15) for the CC-free equivalent straight beam. Note from tables 10 and 11 that the prediction error at the center ($y_8$) of the CEV CC-free curved beam is only 1.8477 percent compared with the miniscule prediction error of 0.2471 percent at the center ($y_8$) of the CC-free equivalent straight beam.

Table 11. Comparison of deflections calculated from SPAR with those calculated from deflection equation (15) for the CC-free equivalent straight beam.

| $\hat{y}_i^B$ | $\hat{y}_0^B$ (left end) | $\hat{y}_1^B$ | $\hat{y}_2^B$ | $\hat{y}_3^B$ | $\hat{y}_4^B$ | $\hat{y}_5^B$ | $\hat{y}_6^B$ | $\hat{y}_7^B$ | $\hat{y}_8^B$ (center) |
|---|---|---|---|---|---|---|---|---|---|
| SPAR | 0.0000 | 0.0868 | 0.3121 | 0.6298 | 0.9936 | 1.3571 | 1.6741 | 1.8982 | 1.9833 |
| Eq. (15), straight | 0.0000 | 0.0852 | 0.3103 | 0.6287 | 0.9939 | 1.3593 | 1.6779 | 1.9031 | 1.9882 |
| Difference, percent | 0.0000 | 1.8433 | 0.5767 | 0.1747 | 0.0302 | 0.1621 | 0.2270 | 0.2581 | 0.2471 |

|<----------Left half of CEV CC-free straight beam---------->

Figure 22 shows the deflection curves calculated from the data of table 10 for the CEV CC-free curved beam. Because of graphical proximity, and to avoid plot congestion, the deflection curve for the equivalent straight beam was not plotted from the data in table 11. The predicted deflection curve based on equation (22) is represented by a solid line with solid circular symbols, whereas the deflection curve calculated from the SPAR program is represented by a dotted line with open circular symbols. Figure 22 also shows the deflection curve, $\hat{y}_i^B = y_i$, calculated from the straight-beam deflection equation (10), which is represented by a dashed-dotted line with solid triangular symbols. Note that the deflection curve, $\hat{y}_i^B = y_i$, gives relatively good shape prediction on the left-half region of the beam. The prediction error, however, gradually increases beyond the midpoint of the beam and reaches a maximum value of $y_n = 0.241682$ in. at the right support. With the curvature effect introduced (eq. (22)), the predicted deflection curve converges to the SPAR deflection curve. The accuracy of the shape predictions may be optimized by slightly altering the coefficient (4/*p*) of the sine correction function in equation (22).

**Case of Both Ends Clamped and Stationary (CC-Fixed)**

Figure 23 shows the strains, $\varepsilon_i$, generated from the SPAR program, for the CEV two-point supported curved beam under the CC-fixed support condition. Because of stationary supports, the strain curve has a rounded M-shape. The strain data of figure 23 were used to calculate the deflections using the curved-beam deflection equation (22). Table 12 compares the deflections calculated from the SPAR program with those calculated from the curved-beam deflection equation (22) for the CEV CC-fixed curved beam. Note that the prediction error at the center ( $\hat{y}_8^B$ ) (maximum deflection point) of the CEV CC-fixed curved beam is only 0.2349 percent, showing the degree of accuracy of deflection equation (22) formulated for clamped curved beams.

Table 12. Comparison of deflections calculated from SPAR with those calculated from deflection equation (22) for the CEV CC-fixed curved beam.

| $\hat{y}_i^B$ | $\hat{y}_0^B$ (left end) | $\hat{y}_1^B$ | $\hat{y}_2^B$ | $\hat{y}_3^B$ | $\hat{y}_4^B$ | $\hat{y}_5^B$ | $\hat{y}_6^B$ | $\hat{y}_7^B$ | $\hat{y}_8^B$ (center) |
|---|---|---|---|---|---|---|---|---|---|
| SPAR | 0.0000 | –0.0168 | –0.0457 | –0.0621 | –0.0529 | –0.0157 | –0.0421 | 0.0998 | 0.1277 |
| Eq. (22) | 0.0000 | –0.0167 | –0.0454 | –0.0619 | –0.0525 | –0.0149 | 0.0425 | 0.1000 | 0.1274 |
| Difference, percent | 0.0000 | 0.5952 | 0.6565 | 0.3221 | 0.7561 | 2.6144 | 0.9501 | 0.2004 | 0.2349 |

|<----------Left half of CEV CC-fixed curved beam ---------->

Note: Inward deflection is considered positive; outward deflection is negative.

Figure 24 shows the deflection curves for the CEV CC-fixed curved beam plotted from the data listed in table 12. The deflection curve calculated from equation (22) is represented by a solid line with solid circular symbols, whereas the deflection curve calculated from the SPAR program is represented by a dotted line with open circular symbols. Also, the deflection curve, $\hat{y}_i^B = y_i$, calculated from the straight-beam deflection equation (10) is represented by a dashed-dotted line with solid triangular symbols. Note that the straight-beam deflection equation (10) induces a maximum prediction error of $y_n = -0.097526$ in. at the right support. With the curvature effect considered, the deflection curve calculated from equation (22) pictorially agrees with the SPAR deflection curve, confirming the high accuracy of the curved-beam deflection equation (22) formulated for clamped curved beams.

## Both Ends Simply Supported

Figure 25 shows the deformed shapes, generated from the SPAR program, of the CEV simply supported curved beam under an inward radial central load of $P = 2$ lb. For the SS-free case (fig. 25a), the deformation is a shallow bow shape, because the supports are allowed to move tangentially. For the SS-fixed case (fig. 25b), the deformed shape is wavier because of the stationary support points.

Because the CEV two-point supported curved beam has a curved-beam angle ($\phi_n = 44°$) very close to $\phi_n = 45°$, in the calculations of the deflections for both the SS-free and SS-fixed cases, the curved-beam deflection equation (20b) ($\phi_n = 45°$), rewritten as equation (23), was used:

$$\hat{y}_i^B = y_i - \underbrace{\left[\frac{i}{n} + \left(\frac{\phi_n}{360}\right)^2 \sin\left(\frac{i}{n}\pi\right)\right] y_n}_{\text{Correction term to enforce } \hat{y}_n^B = 0 \text{ at right support } (i = n).} \quad ; \quad (i = 1,2,3,...,n) \tag{23}$$

### Case of Both Ends Simply Supported and Free to Move Along Beam Curve (SS-Free)

Figure 26 shows the strains, $\varepsilon_i$, generated from the SPAR program, for the CEV two-point supported curved beam and for the equivalent straight beam under the SS-free support condition. The two strain curves are V-shaped and are fairly close, but not as close as those in the CC-free support case (fig. 21). The strain data of figure 26 were used to calculate the deflection curves for the CEV SS-free curved beam

using deflection equation (23). Table 13 compares the deflections calculated from the SPAR program with those calculated from the curved-beam deflection equation (23) for the CEV SS-free curved beam.

Table 13. Comparison of deflections calculated from SPAR with those calculated from deflection equation (23) for the CEV SS-free curved beam.

| $\hat{y}_i^B$ | $\hat{y}_0^B$ (left end) | $\hat{y}_1^B$ | $\hat{y}_2^B$ | $\hat{y}_3^B$ | $\hat{y}_4^B$ | $\hat{y}_5^B$ | $\hat{y}_6^B$ | $\hat{y}_7^B$ | $\hat{y}_8^B$ (center) |
|---|---|---|---|---|---|---|---|---|---|
| SPAR | 0.0000 | 1.6723 | 3.2909 | 4.8022 | 6.1534 | 7.2916 | 8.1664 | 8.7264 | 8.9242 |
| Eq. (23), straight | 0.0000 | 1.6566 | 3.2600 | 4.7573 | 6.0960 | 7.2242 | 8.0911 | 8.6465 | 8.8419 |
| Difference, percent | 0.0000 | 0.9388 | 0.9390 | 0.9350 | 0.9328 | 0.9244 | 0.9221 | 0.9156 | 0.9222 |

|<----------Left half of CEV SS-free curved beam---------->

The strain data of figure 26 were used as inputs to calculate the deflections for the SS-free equivalent straight beam, using both the SPAR program and deflection equation (14) (for simply supported straight beams). Table 14 compares these deflections. Note from tables 13 and 14 that the prediction error of 0.9222 percent at the center ( $\hat{y}_8^B$ ) of the SS-free CEV curved beam is slightly larger than the corresponding prediction error of 0.8214 percent for the SS-free equivalent straight beam.

Table 14. Comparison of deflections calculated from SPAR with those calculated from deflection equation (14) for SS-free equivalent straight beams.

| $\hat{y}_i^B$ | $\hat{y}_0^B$ (left end) | $\hat{y}_1^B$ | $\hat{y}_2^B$ | $\hat{y}_3^B$ | $\hat{y}_4^B$ | $\hat{y}_5^B$ | $\hat{y}_6^B$ | $\hat{y}_7^B$ | $\hat{y}_8^B$ (center) |
|---|---|---|---|---|---|---|---|---|---|
| SPAR | 0.0000 | 1.4737 | 2.9011 | 4.2356 | 5.4319 | 6.4425 | 7.2220 | 7.7232 | 7.9010 |
| Eq. (14) | 0.0000 | 1.4865 | 2.9262 | 4.2721 | 5.4779 | 6.4969 | 7.2823 | 7.7874 | 7.9659 |
| Difference, percent | 0.0000 | 0.8686 | 0.7652 | 0.8617 | 0.8468 | 0.8444 | 0.8349 | 0.8313 | 0.8214 |

|<----------Left half of SS-free equivalent straight beam---------->

Figure 27 shows the deflection curves based on the data listed in table 13 for the CEV SS-free curved beam. Because of data proximity and to avoid plot congestion, deflection curves for the SS-free equivalent straight beam were not plotted from the data in table 14. The predicted deflection curve based on the curved-beam deflection equation (23) is represented by a solid line with solid circular symbols, whereas the deflection curve calculated from the SPAR program is represented by a dotted line with open circular symbols. The proximity of the predicted and SPAR deflection curves validates the accuracy of the deflection equation (23) formulated for simply supported curved beams.

For comparison, figure 27 also shows the deflection curve, $\hat{y}_i^B = y_i^B = y_i - \left(i/n\right) y_n$ (eq. (14) for simply supported straight beams), represented by a dashed-dotted line with solid triangular symbols, to demonstrate the prediction accuracy. Note that for the SS-free support case, the deflection curve calculated from deflection equation (14) lies slightly under the SPAR deflection curve in the central region of the beam.

**Case of Both Ends Simply Supported and Stationary (SS-Fixed)**

Figure 28 shows the strains, $\varepsilon_i$, generated from the SPAR program, for the CEV two-point supported curved beam under the SS-fixed support condition. The strain curve has a distorted M-shape instead of a V-shape (as in the straight-beam case) because of the curvature effect and support constraints. The strain data of figure 28 were used to calculate the deflections for the CEV SS-fixed curved beam using the SPAR program and the curved-beam deflection equation (23). Table 15 presents the resulting deflection data. The radial inward deflections are defined as positive, and the outward deflections are negative.

Table 15. Comparison of deflections calculated from SPAR with those calculated from curved-beam deflection equation (23) for the CEV SS-fixed curved beam.

| $\hat{y}_i^B$ | $\hat{y}_0^B$ (left end) | $\hat{y}_1^B$ | $\hat{y}_2^B$ | $\hat{y}_3^B$ | $\hat{y}_4^B$ | $\hat{y}_5^B$ | $\hat{y}_6^B$ | $\hat{y}_7^B$ | $\hat{y}_8^B$ (center) |
|---|---|---|---|---|---|---|---|---|---|
| SPAR | 0.0000 | 0.0882 | 0.3150 | 0.6351 | 1.0021 | 1.3693 | 1.6898 | 1.9164 | 2.0025 |
| Eq. (22), curved | 0.0000 | 0.0838 | 0.3056 | 0.6200 | 0.9812 | 1.3427 | 1.6581 | 1.8811 | 1.9655 |
| Difference, percent | 0.0000 | 439887 | 2.9841 | 2.3776 | 2.0856 | 1.9426 | 1.8760 | 1.8420 | 1.8477 |

|<----------Left half of CEV SS-fixed curved beam---------->

Note: Inward deflection is considered positive; outward deflection is negative.

Figure 29 shows the deflection curves based on the data listed in table 15 for the CEV SS-fixed curved beam. The theoretical deflection curve based on the curved-beam deflection equation (23) (solid line with solid circular symbols) is fairly close to the SPAR deflection curve (dotted line with open circular symbols). In figure 29, the deflection curve, $\hat{y}_i^B = y_i^B = y_i - (i/n)y_n$, calculated from the straight-beam deflection equation (14) (dashed-dotted line with solid triangular symbols) somewhat overpredicts the deflections in the central region of the beam.

To improve the shape predictions for the SS-fixed case, the curved-beam deflection equation (23) can be modified to the following form:

$$\hat{y}_i^B = y_i - \underbrace{\left[\frac{i}{n} + \frac{6}{\pi}\left(\frac{\phi_n}{360}\right)^2 \sin^4\left(\frac{i}{n}\pi\right)\right] y_n}_{\text{Correction term to enforce } \hat{y}_n^B = 0 \text{ at right support } (i = n).} \quad ; \quad (i = 1,2,3,...,n) \tag{24}$$

Based on the modified curved-beam deflection equation (24), the deflections of the CEV SS-fixed curved beam were recalculated, and the resulting deflection data are listed in table 16.

Table 16. Comparison of deflections calculated from SPAR with those calculated from modified curved-beam deflection equation (24) for the CEV SS-fixed curved beam.

| $\hat{y}_i^B$ | $\hat{y}_0^B$ (left end) | $\hat{y}_1^B$ | $\hat{y}_2^B$ | $\hat{y}_3^B$ | $\hat{y}_4^B$ | $\hat{y}_5^B$ | $\hat{y}_6^B$ | $\hat{y}_7^B$ | $\hat{y}_8^B$ (center) |
|---|---|---|---|---|---|---|---|---|---|
| SPAR | 0.0000 | –0.0568 | –0.0913 | –0.0925 | –0.0581 | 0.0059 | 0.0849 | 0.1560 | 0.1880 |
| Eq. (24), curved | 0.0000 | –0.0570 | –0.0918 | 0.0930 | –0.0588 | 0.0046 | 0.0832 | 0.1545 | 0.1868 |
| Difference, percent | 0.0000 | 0.3521 | 0.5476 | 0.5405 | 1.2048 | 22.0339* | 2.0024 | 0.9615 | 0.6383 |

|<----------Left half of CEV SS-fixed curved beam----------> 

Note: Inward deflection is positive; outward deflection is negative.
*Caused by a small number divided by a small number.

Note from table 16 that when the modified deflection equation (24) is used, the prediction error at the beam center ( $y_8$ ) for the SS-fixed case could be reduced to nearly one-tenth (1/10) that when equation (23) is used (table 15). In table 16, the large error of 22.0339 percent for the deflection, $\hat{y}_5^B$, is caused by a small number divided by another small number, and it is insignificant.

Figure 30 compares the deflection curves calculated from the modified curved-beam deflection equation (24) with those calculated from the SPAR program using the data listed in table 16. The predicted deflection curve practically falls on top of the SPAR deflection curve, demonstrating the accuracy of the modified curved-beam deflection equation (24) established for the CEV SS-fixed curved beam.

## SINGLE–POINT COLLOCATIONS

The curved-beam deflection equations (20) and (21) formulated for two-point supported curved beams could provide sufficiently accurate shape predictions. For further optimization of shape prediction accuracy, however, the coefficients of the sine correction functions appearing in the curved-beam deflection equations (20) and (21) can be modified slightly by applying the single-point collocation method discussed in this section.

### Clamped Curved Beams

As shown in figure 11, the deflection curves generated from the curved-beam deflection equation (20) practically agree with the respective SPAR deflection curves (references). For optimum prediction accuracy, however, a single-point collocation method can be applied to further improve the correction functions in equation (20). Equations (20b–c) can be unified into a general form for $0 \le \phi_n \le 360°$ arcs as

$$\hat{y}_i^B = \underbrace{y_i - \left(\frac{i}{n}\right)^2 y_n}_{=y_i^B\,(\text{eq. (20a)})} + \underbrace{\eta \sin^4\left(\frac{i}{n}\pi\right)}_{\substack{\text{Curvature-effect} \\ \text{correction term}}} = y_i^B + \eta \sin^4\left(\frac{i}{n}\pi\right) \quad ; \quad (i = 1,2,3,...,n) \tag{25}$$

in which equation (20a) is used, and $\eta$ (in.) is the amplitude of the sine correction function. When the single-point collocation method was applied, the collocation point was chosen to be at the midpoint of the beam (load application point) where the deflection is at a maximum.

Let $\{ y^C_{n/2},\ y^B_{n/2} \}$ be the deflections at the center of the two-point supported curved beam calculated from the SPAR program and from the two-point supported straight-beam deflection equation (20a) or (21a), respectively, then the midpoint deflection differential $(y^C_{n/2} - y^B_{n/2})$ will give the value of $\eta$. Namely,

$$\eta \equiv y^C_{n/2} - y^B_{n/2} \tag{26}$$

Table 17 lists the values of $\eta$ calculated from equation (26) for all the clamped curved beams.

Table 17. Central deflections and amplitude of sine correction functions, $\eta$, for different clamped curved beams; $n$ = 16.

| $\phi_n$, deg | $y^C_{n/2}$, in. (SPAR) | $y^B_{n/2}$, in. $(= y_i - (i/n)^2\, y_n)$ | $\eta$, in. $(y^C_{n/2} - y^B_{n/2})$ | $\eta / y^C_{n/2}$, percent |
|---|---|---|---|---|
| 0 (straight) | 2.35078 | 2.365080 | –0.014300* | –0.6083** |
| 45 | 0.15144 | 0.147520 | 0.003920 | 2.5885 |
| 90 (1/4 circle) | 0.15317 | 0.143866 | 0.009304 | 6.0743 |
| 135 | 0.15974 | 0.137798 | 0.021942 | 13.7361 |
| 180 (1/2 circle) | 0.17012 | 0.126289 | 0.043831 | 25.7648 |
| 225 | 0.18499 | 0.105753 | 0.079237 | 42.8331 |
| 270 (3/4 circle) | 0.20548 | 0.087697 | 0.117783 | 52.4543 |
| 315 | 0.23336 | 0.053076 | 0.180284 | 77.2557 |
| 360 (full circle) | 0.27090 | –0.001092 | 0.271992 | 100.4031 |

*Negative for straight beam.
** Negligible.

Note in table 17 that the value of $\eta$ for the straight beam ($\phi_n = 0^\circ$) is negative, because the right-end deflection, $y_n$, is positive (fig. 11a). Also note that the magnitude of $\eta$ for the straight beam ($\phi_n = 0^\circ$) is greater than those for the $\phi_n = 45$–$90^\circ$ curved beams. When $\eta$ is normalized by the corresponding SPAR central deflection, $y^C_{n/2}$, however, the magnitude of $\eta / y^C_{n/2}$ for the straight beam ($\phi_n = 0^\circ$) becomes a negligible minimum among all cases.

Figure 31 shows the plot of the $\eta$ data listed in table 17 as a function of the curved-beam angle, $\phi_n$. When the $\eta$-curve of figure 31 is used, the value of $\eta$ for any curved-beam angle, $\phi_n$, can be established graphically. When the values of $\eta$ listed in table 17 are used, the deflection curves calculated from the general curved-beam deflection equation (25) match perfectly with the corresponding SPAR deflection

curves of figure 11 for all the curvature angles ($0 \le \phi_n \le 360°$). For graphical visualization of the deflection curves, only a typical case of a $\phi_n = 180°$ clamped curved beam is shown in figure 32. Note that the deflection curve, $\hat{y}_i^B = y_i^B = y_i - (i/n)^2\, y_n$ (eq. (20a) for clamped straight beams), lies somewhat below the SPAR deflection curve in the center region of the beam. With the single-point collocation, the corrected deflection curve calculated from equation (25) matches precisely with the SPAR deflection curve. Note that the values of $\eta$ can also be determined with the aid of experimentally generated deflection curves instead of using the deflection curves generated from the SPAR program.

## Simply Supported Curved Beams

The displacement equations (21b–g) for the simply supported curved beam can also be unified into a general form, with $\eta$ representing the amplitude of sine correction functions for all the curved-beam angles ($0 \le \phi_n \le 360^\circ$), as

$$\hat{y}_i^B = \underbrace{y_i - \frac{i}{n} y_n}_{= y_i^B \text{ (eq. (21a))}} + \underbrace{\eta \sin^m\left(\frac{i}{n}\pi\right)}_{\substack{\text{Curvature-effect} \\ \text{correction term}}} = y_i^B + \eta \sin^m\left(\frac{i}{n}\pi\right) \quad ; \quad (i = 1,2,3,...,n) \qquad (27)$$

in which equation (21a) was used, and the values of the exponent *m* of the sine correction function is *m* = 1, 3, or 4, depending on the value of $\phi_n$ (eqs. (21b–g)). The values of $\eta$ for the simply supported curved beams were calculated from equation (26) using the single-point collocation method described in the clamped curved-beam cases. Table 18 lists these values.

Table 18. Central deflections, amplitudes, and exponents $\{\eta, m\}$ of the sine correction functions for different simply supported curved beams; *n* = 16.

| $\phi_n$, deg | $y_{n/2}^C$, in. (SPAR) | $y_{n/2}^B$, in. $(= y_i - (i/n)^2\, y_n)$ | $\eta$, in. $(y_{n/2}^C - y_{n/2}^B)$ | *m* | $\eta / y_{n/2}^C$, percent |
|---|---|---|---|---|---|
| 0 (straight) | 9.40818 | 9.479265 | –0.071085* | ----- | –0.7556** |
| 45 | 0.21423 | 0.229521 | –0.015291* | 1 | –7.1377 |
| 90 (1/4 circle) | 0.22723 | 0.233778 | –0.006548* | 1 | –2.8817 |
| 135 | 0.24530 | 0.225642 | 0.019658 | 4 | 8.0139 |
| 180 (1/2 circle) | 0.27246 | 0.213297 | 0.059163 | 4 | 21.7144 |
| 225 | 0.31359 | 0.186855 | 0.126735 | 4 | 40.4142 |
| 270 (3/4 circle) | 0.37707 | 0.135262 | 0.241808 | 4 | 64.1281 |
| 315 | 0.47909 | 0.039780 | 0.439310 | 3 | 91.6968 |
| 360 (full circle) | 0.65333 | –0.157195 | 0.810525 | 3 | 124.0606 |

*Negative for $\phi_n$ = 0–90°.

**Negligible.

The values of $\eta$ listed in table 18 are plotted in figure 33 for visualization of the shape of the $\eta$ curve from which the values of $\eta$ for other unlisted curved-beam angles, $\phi_n$, can be easily obtained graphically. In table 18, the magnitude of $\eta$ for the straight beam ($\phi_n = 0^\circ$) appears to be greater than those for the $\phi_n = 45 – 180^\circ$ curved beams. When $\eta$ is normalized by the corresponding SPAR central deflection, $y^C_{n/2}$, however, the magnitude of $\eta / y^C_{n/2}$ for the straight beam ($\phi_n = 0^\circ$) becomes a negligible minimum among all cases.

When the values of $\eta$ listed in table 18 for the general curved-beam deflection equation (27) are used, the calculated deflection curves practically coincide with the corresponding SPAR deflection curves of figure 14. For graphical visualization of the deflection curves, only a typical case of $\phi_n = 180^\circ$ simply supported curved beam is shown in figure 34. Note that the deflection curve, $\hat{y}^B_i = y^B_i = y_i - \left(i/n\right) y_n$ (eq. (21a) for simply supported straight beams), lies somewhat below the SPAR deflection curve in the center region of the beam. With the single-point collocation, the corrected deflection curve based on equation (27) matches precisely with the SPAR deflection curve. In actual shape predictions, the values of $\eta$ can be determined in the light of actual measured deflection curves instead of using the SPAR deflection curves.

## STRAIN–SENSING STATION DENSITY

It is important to mention that when fiber-optic strain-sensing systems are used, the strain-sensing station density (value of *n*) can be easily increased at will by simply increasing the multiplexed Bragg grating density (that is, reducing the sensing intervals; ref. 3) without the need for time-consuming installations of additional strain sensors, as is the case with using conventional strain gages. The effect of strain-sensing station density on the shape prediction accuracy was investigated by increasing the value of *n* from 16 to 32. Increasing the number of strain-sensing stations implies the shrinking of the divided beam subdomains (that is, shrinking the sensing intervals), causing the theoretical piece-wise linear beam to approach the actual curved beam. Therefore, one might expect the shape prediction accuracy to improve, but the overall benefit was found to be miniscule.

For the cantilever curved beams, the shape prediction accuracy remained practically the same when the value of *n* was increased from 16 to 32. Likewise, for the two-point supported curved beams, the prediction accuracy was insensitive to the change in the *n* value from 16 to 32 as described in detail in the following section.

### Clamped Curved Beams

Figure 35 shows the bending strain curves, generated from the SPAR program, for the clamped curved-beam cases ($0 \le \phi_n \le 360^\circ$) based on *n* = 32. These strain curves are very similar to the strain curves based on *n* = 16 (fig. 10). The strain data of figure 35 were used to calculate the amplitude, $\eta$, of the sine correction functions for *n* = 32 from the single-point collocation equation (26) for different clamped curved-beam cases. Table 19 lists these values and also lists the corresponding values of $\eta$ for *n* = 16 (taken from table 17) for comparison.

Table 19. Central deflections and amplitudes of the sine correction function, $\eta$, calculated for different clamped curved beams; $n$ = 32.

| $\phi_n$, deg | $y^C_{n/2}$, in. (SPAR) | $y^B_{n/2}$, in. ($\equiv y_i - (i/n)^2\, y_n$) | $\eta$, in. ($\equiv y^C_{n/2} - y^B_{n/2}$) ($n$ = 32) | $\eta$, in. (table 17) ($n$ = 16) |
|---|---|---|---|---|
| 0 (straight) | 2.35078 | 2.370436 | –0.019656* | –0.014300* |
| 45 | 0.15144 | 0.144950 | 0.006490 | 0.003920 |
| 90 (1/4 circle) | 0.15317 | 0.144379 | 0.008791 | 0.009304 |
| 135 | 0.15974 | 0.137835 | 0.021905 | 0.021942 |
| 180 (1/2 circle) | 0.17012 | 0.127108 | 0.043012 | 0.043822 |
| 225 | 0.18499 | 0.110216 | 0.074774 | 0.079237 |
| 270 (3/4 circle) | 0.20548 | 0.089372 | 0.116108 | 0.117783 |
| 315 | 0.23336 | 0.053559 | 0.179801 | 0.180284 |
| 360 (full circle) | 0.27090 | –0.001129 | 0.272029 | 0.271992 |

* Negative for the straight beam.

Table 19 shows that $\eta$ is nearly insensitive to the change in strain-sensing station density (value of $n$). Figure 36 shows the $\eta$ curves based on the data listed in table 19 for the clamped curved beams. The $\eta$ curves for $n$ = 16 and $n$ = 32 are extremely close, indicating that prediction accuracy is insensitive to the change in strain-sensing station density (value of $n$).

Figure 37 shows the deflection curves of different clamped curved beams based on $n$ = 32. The corresponding deflection curves based on $n$ = 16 (taken from fig. 33) also are plotted for comparison. Note that increasing the value of $n$ from 16 to 32 did move the deflection curves, $\hat{y}^B_i = y_i$ (eq. (10) for cantilever straight beams), upward and thereby reduced the magnitudes of the right-end deflections, $y_n$. The deflection curves, $\hat{y}^B_i = y^B_i = y_i - (i/n)^2\, y_n$ (eq. (20a) for clamped straight beams), based on $n$ = 16 and $n$ = 32 for each curved-beam angle, however, turned out to be extremely close, and their difference is graphically indistinguishable. Note in figure 37 that the single-point collocation deflection curves calculated from equation (25) based on $n$ = 32 are practically coincidental with the corresponding SPAR deflection curves for the whole range of curved-beam angles ($0 \le \phi_n \le 360^\circ$) (see fig. 32 for the $n$ = 16 case). Based on these observations, using $n$ = 16 could be considered adequate in the present shape prediction analysis of the clamped curved beams (see ref. 4).

## Simply Supported Curved Beams

Figure 38 shows the bending strain curves, generated from the SPAR program, for the simply supported curved-beam cases ($0 \le \phi_n \le 360^\circ$) for $n$ = 32. Again, these strain curves are practically identical to the strain curves for $n$ = 16 (fig. 13). The strain data of figure 38 were used to calculate the amplitude of the sine correction function, $\eta$, for $n$ = 32 from the single-point collocation equation (26) for different simply supported curved beams. Table 20 lists these values and also lists the values of $\eta$ based on $n$ = 16 (taken from table 18) for comparison.

Table 20. Central deflections, amplitudes, and exponents $\{\eta, m\}$ of the sine correction function for different simply supported curved beams; $n = 32$.

| $\phi_n$, deg | $y^C_{n/2}$, in. (SPAR) | $y^B_{n/2}$, in. $(\equiv y_i - (i/n)y_n)$ | $\eta$, in. $(\equiv y^C_{n/2} - y^B_{n/2})$ $(n = 32)$ $(n = 16)$ | $\eta$, in. (table 18) |
|---|---|---|---|---|
| 0 (straight) | 9.40818* | 9.41767 | –0.066570** | –0.071085** |
| 45 | 0.21423 | 0.216002 | –0.001772** | –0.015291** |
| 90 (1/4 circle) | 0.22723 | 0.217717 | –0.009513** | –0.006548** |
| 135 | 0.24530 | 0.211281 | 0.034019 | 0.019658 |
| 180 (1/2 circle) | 0.27246 | 0.197559 | 0.074901 | 0.059163 |
| 225 | 0.31359 | 0.170597 | 0.142992 | 0.126735 |
| 270 (3/4 circle) | 0.37707 | 0.120870 | 0.256200 | 0.241808 |
| 315 | 0.47909 | 0.026165 | 0.452925 | 0.439310 |
| 360 (full circle) | 0.65333 | –0.172672 | 0.826002 | 0.810525 |

*Very much larger compared with curved-beam cases.
**Negative for $\phi_n$ = 0–90°.

Figure 39 compares the $\eta$ curves for $n = 16$ and $n = 32$, plotted from the data listed in table 20, for the simply supported curved beams. The two $\eta$ curves are quite close, indicating that the prediction accuracy is insensitive to the change in strain-sensing station density (value of $n$).

In figure 40, the deflection curves calculated from $\hat{y}^B_i = y^B_i = y_i - (i/n)y_n$ (eq. (21a) for simply supported straight beams), based on $n = 32$ for different simply supported curved beams, are compared with the corresponding deflection curves, $\hat{y}^B_i = y^B_i = y_i - (i/n)y_n$, based on $n = 16$ (taken from fig. 14). The two deflection curves, $\hat{y}^B_i = y^B_i = y_i - (i/n)y_n$, based on $n = 16$ and $n = 32$ for each curved-beam angle are fairly close, but not as close as those in the clamped support cases (fig. 37). Figure 40 also shows that the single-point collocation deflection curves calculated from equation (27) based on $n = 32$ are pictorially coincidental with the corresponding SPAR deflection curves for curved-beam angles in the range $0 \le \phi_n \le 180°$. For larger curved-beam angles, $225 \le \phi_n \le 360°$, however, the left and right regions of the deflection curves based on equation (27) become slightly off from the corresponding SPAR deflection curves (see fig. 34 for the $n = 16$ case). Again, based on these observations, using $n = 16$ could be considered adequate for the present shape prediction analysis of the simply supported curved beams (see also ref. 4).

# DISCUSSION

In the shape prediction analysis of the CEV curved wall and other curved aerospace structures, using the clamped support condition is more realistic than using the simply supported condition. Under the clamped support condition, only two mathematical forms of deflection equations (20b–c) are needed for the shape predictions of clamped two-point supported curved beams, including a full circular ring.

The values of $\eta$ listed in tables 19 and 20 are for the central load of $P = 2$ lb only. For any other central load, $P$, the associated $\eta$ values (for $\phi_n$ = 0–360°) can be obtained by simply scaling up (or

scaling down) the values of $\eta$ in tables 19 and 20 in proportion to the magnitude of the new central load, *P*. The present curved-beam shape analysis is for the symmetrical loading condition, which occurs in most of the actual curved structures, such as an aircraft fuselage subjected to landing impacts, or a bomber fuselage subjected to a side blast wave. For measurements of the radial displacements of the fuselage cross section, either a semicircumferential or full-circumferential fiber-optic strain-sensing line system can be used (see figure 41 for the landing impact case).

For rare nonsymmetrical loading cases, the mathematical functional forms of the curvature-effect correction terms must be properly modified accordingly. Furthermore, the present curved-beam shape prediction method can also be applied to shape predictions of irregular-shaped structures such as a generic CEV shell, which is the union of a windward shallow spherical shell, a leeward deep spherical shell, a shoulder toroidal shell, and a side conical shell. The shape prediction analysis of the CEV shell (circular cross section normal to the axis of symmetry, and rounded triangular cross section along the axis of symmetry) is currently under way, and the results are expected to be presented in a subsequent report.

# SUMMARY

The Ko displacement theory originally developed for shape predictions of straight beams was further extended to shape predictions of curved beams with different curvatures. The surface strains for input to the deflection equations for shape predictions were analytically generated from finite-element nodal stress outputs. The shape prediction errors resulting from the use of straight-beam deflection equations for curved beams were examined in light of the finite-element deflection curves. Mathematical functional forms for curvature-effect correction terms were established and incorporated into the straight-beam deflection equations for shape predictions of both cantilever curved beams and two-point supported curved beams. The newly developed curved-beam deflection equations were applied to shape predictions of crew exploration vehicle (CEV) curved beams for accuracy validation. The principal findings of the present analytical shape prediction analysis of curved beams are as follows:

1. For both cantilever straight beams (limit case of a curved beam) and two-point supported straight beams under tip load, the straight-beam deflection equation is very accurate in shape predictions.

2. When the straight-beam deflection equation was used for shape predictions of cantilever curved beams, the beam tip prediction errors were {0.0834, 1.4951, 6.1000, 14.3011, 26.6437} percent for cases of curved-beam angles of {0.0, 22.5, 45.0, 67.5, 90.0} degrees, respectively.

3. When the newly established cantilever curved-beam deflection equation was used, the beam tip prediction errors could be brought down to {0.0834, 0.0849, 0.2127, 0.0126, 1.4978} percent for cases of curved-beam angles of {0.0, 22.5, 45.0, 67.5, 90.0} degrees, respectively.

4. For two-point clamped curved beams, two deflection equations were formulated for accurate shape predictions of a whole range of curved beams, including the circular ring.

5. For two-point simply supported curved beams, six deflection equations were formulated for accurate shape predictions of a whole range of curved beams, including the circular ring.

6. The newly formulated cantilever curved-beam deflection equation was applied to shape predictions of the CEV cantilever curved beam with a miniscule prediction error of 0.4646 percent at the beam tip.

7. The modified deflection equations for two-point supported curved beams were applied to shape predictions of the CEV two-point supported curved beam with negligible beam center prediction errors of {1.8477, 0.2349, 0.9222, 0.6383} percent, respectively, for the support cases of both ends clamped and free to move along the beam curve, both ends clamped and stationary, both ends simply supported and free to move along the beam curve, and both ends simply supported and stationary.

8. For both cantilever and two-point supported curved beams, the prediction accuracy was found to be insensitive to the change in strain-sensing station density from 16 to 32.

9. The single-point collocation method could be used to optimize the shape prediction accuracy of two-point supported curved beams.

# FIGURES

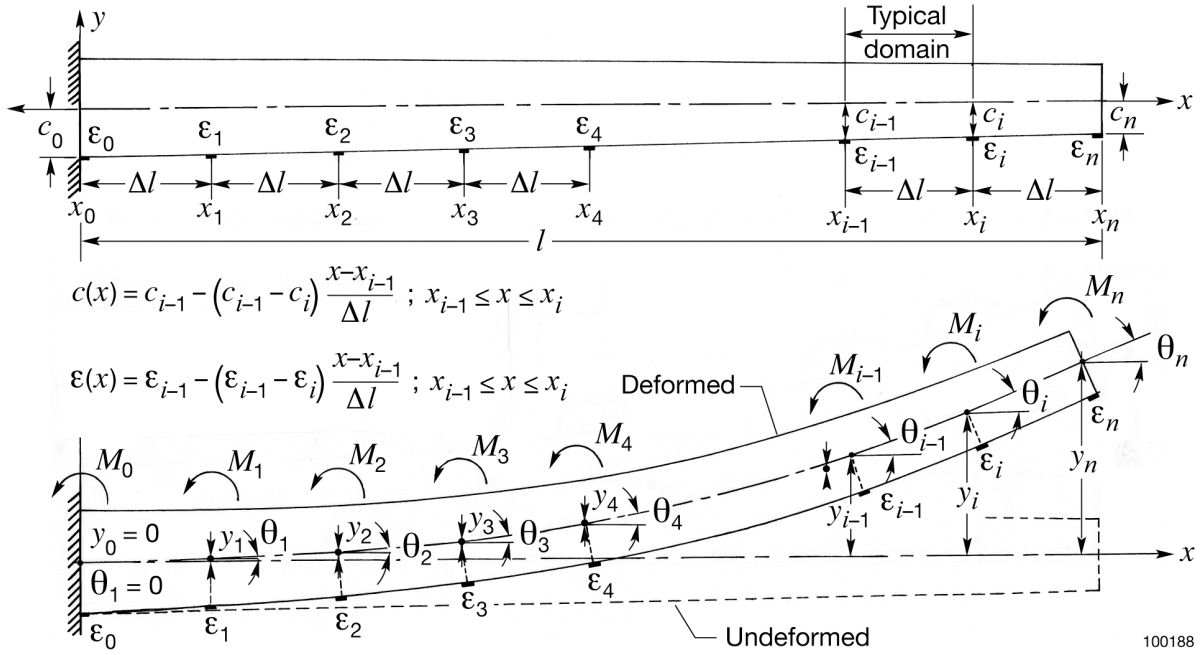


Figure 1. Nonuniform cantilever beam instrumented with equally spaced surface bending strain sensors.

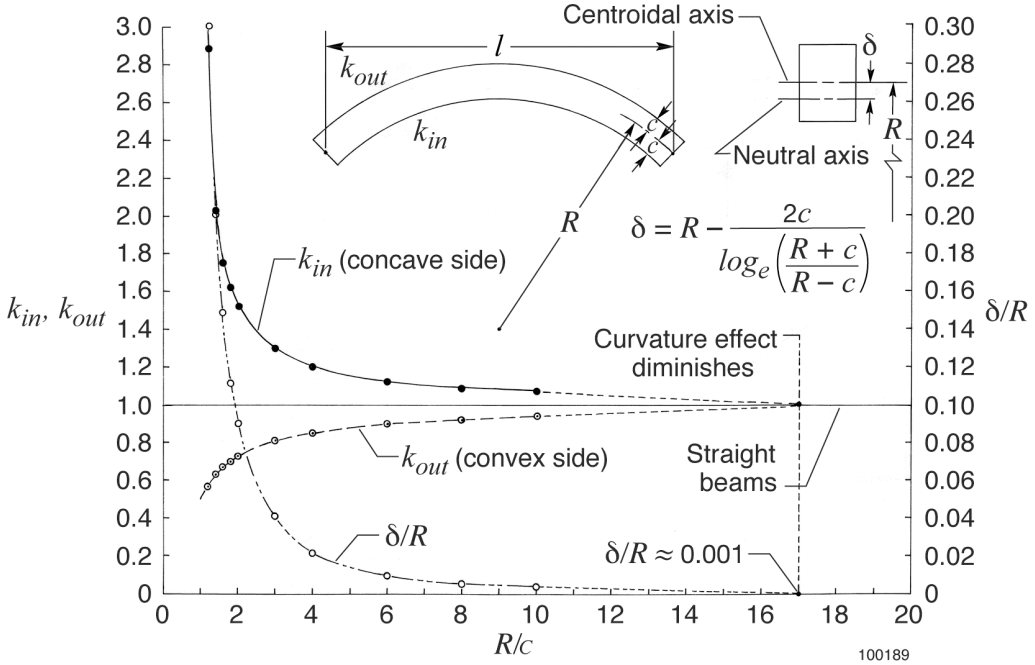


Figure 2. Plots of stress ratios, $\{k_{in}, k_{out}\}$, and neutral axis offset factor, $\delta / R$, for curved beams as functions of curvature factor, $R / c$.

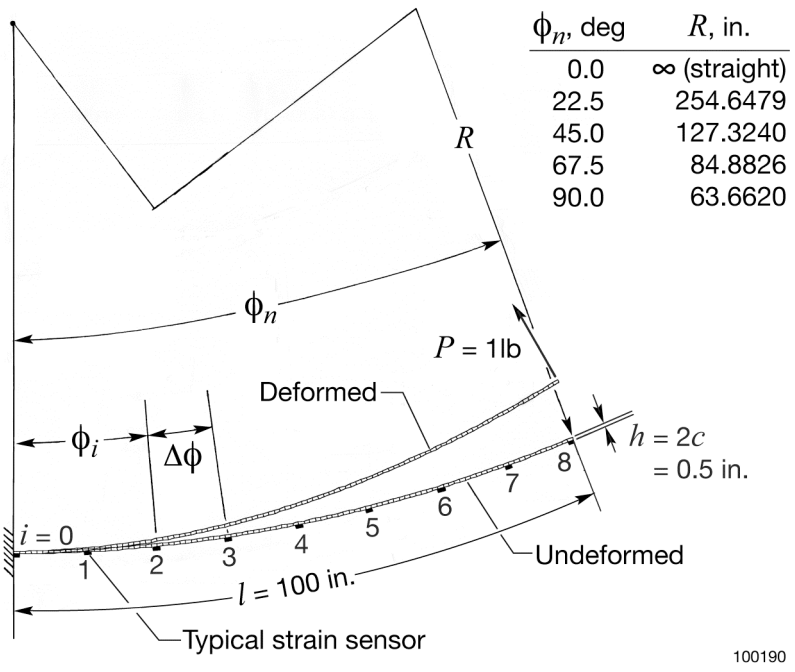


Figure 3. Cantilever curved beam subjected to a tip load of $P$ = 1 lb.

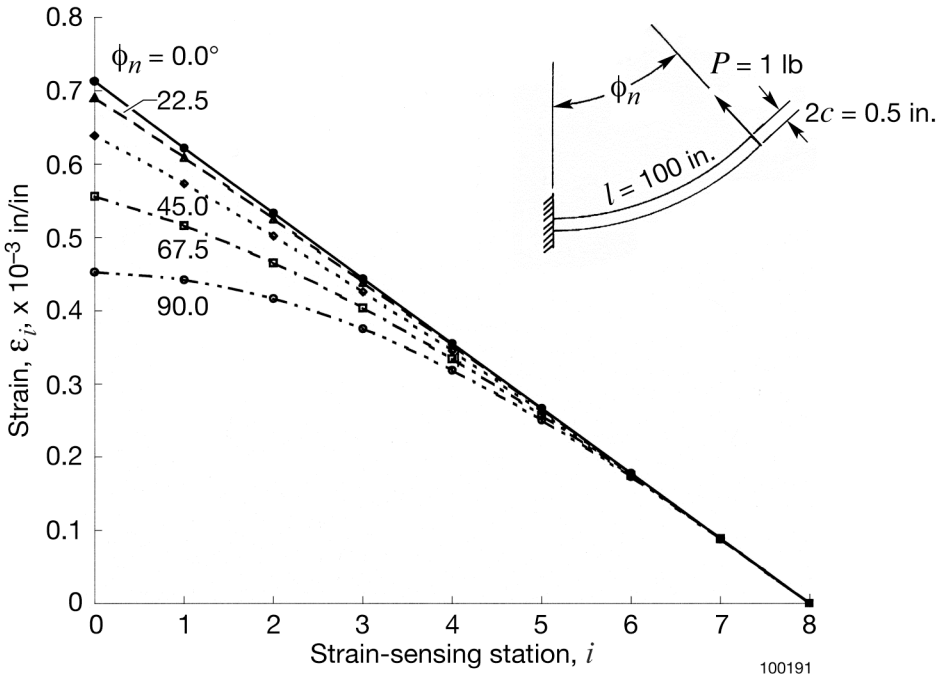


Figure 4. Bending strains, generated from SPAR, for different cantilever curved beams; $P$ = 1 lb; $n$ = 8.

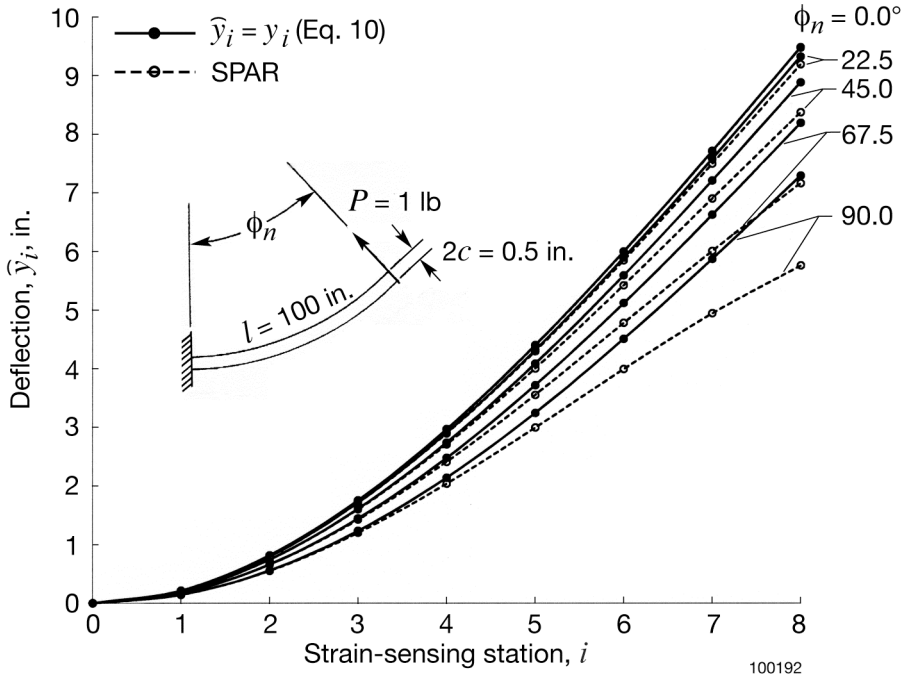


Figure 5. Comparison of deflection curves calculated from SPAR with those calculated from straight-beam deflection equation (10) for different cantilever curved beams; $P$ = 1 lb; $n$ = 8.

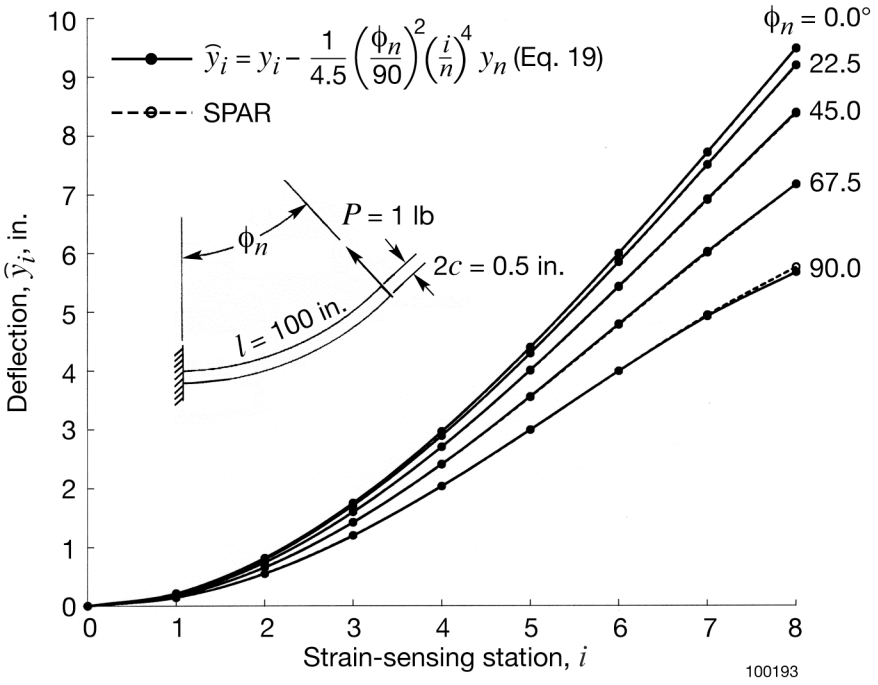


Figure 6. Comparison of deflection curves calculated from SPAR with those calculated from cantilever curved-beam deflection equation (19) for different cantilever curved beams; $P$ = 1 lb; $n$ = 8.

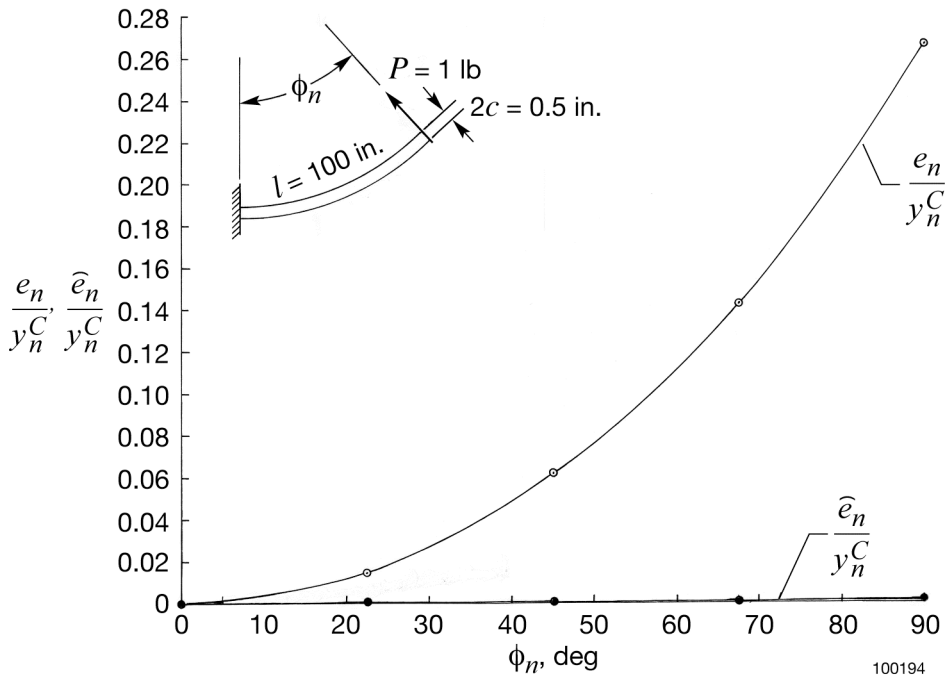


Figure 7. Uncorrected and corrected deflection prediction errors, $\{ e_n / y_n^C, \hat{e}_n / y_n^C \}$, at curved-beam tip plotted as functions of curved-beam azimuth angle, $\phi_n$; $P$ = 1 lb; $n$ = 8.

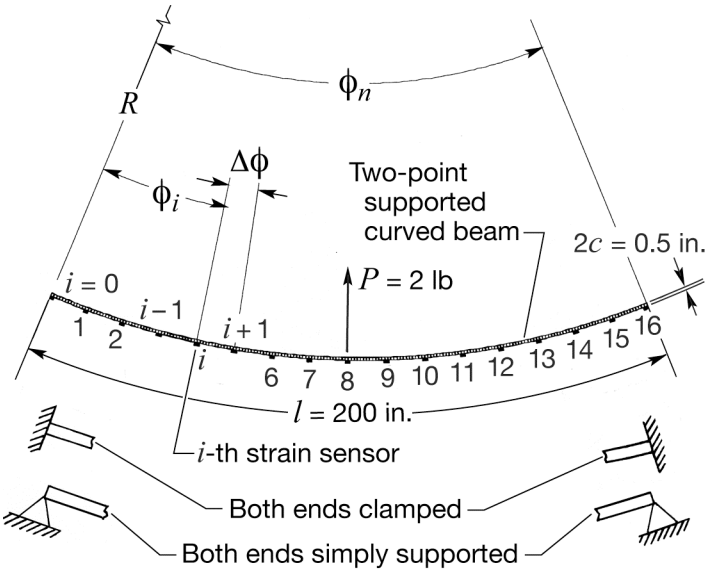


| $\phi_n$, deg | $R$, in. |
|---|---|
| 0 | ∞ (straight) |
| 45 | 254.65 |
| 90 | 127.32 |
| 135 | 84.88 |
| 180 | 63.66 |
| 225 | 50.93 |
| 270 | 42.44 |
| 315 | 36.38 |
| 360 | 31.83 |

Figure 8. Two-point supported curved beam under different support conditions subjected to a central upward load of $P$ = 2 lb.

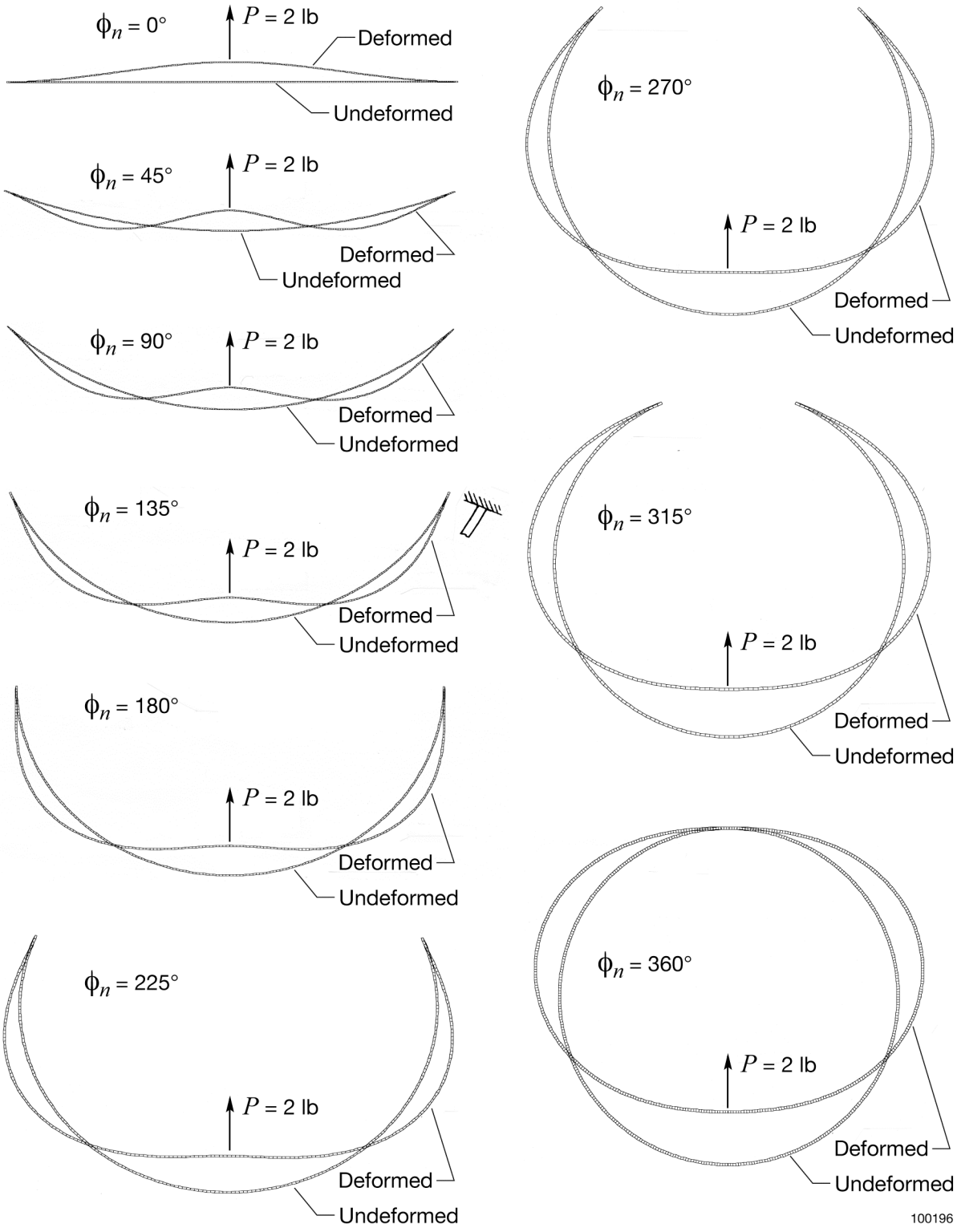


Figure 9. Deformed shapes, generated from SPAR, of two-point supported curved beams with different curvatures; both ends clamped; $P$ = 2 lb.

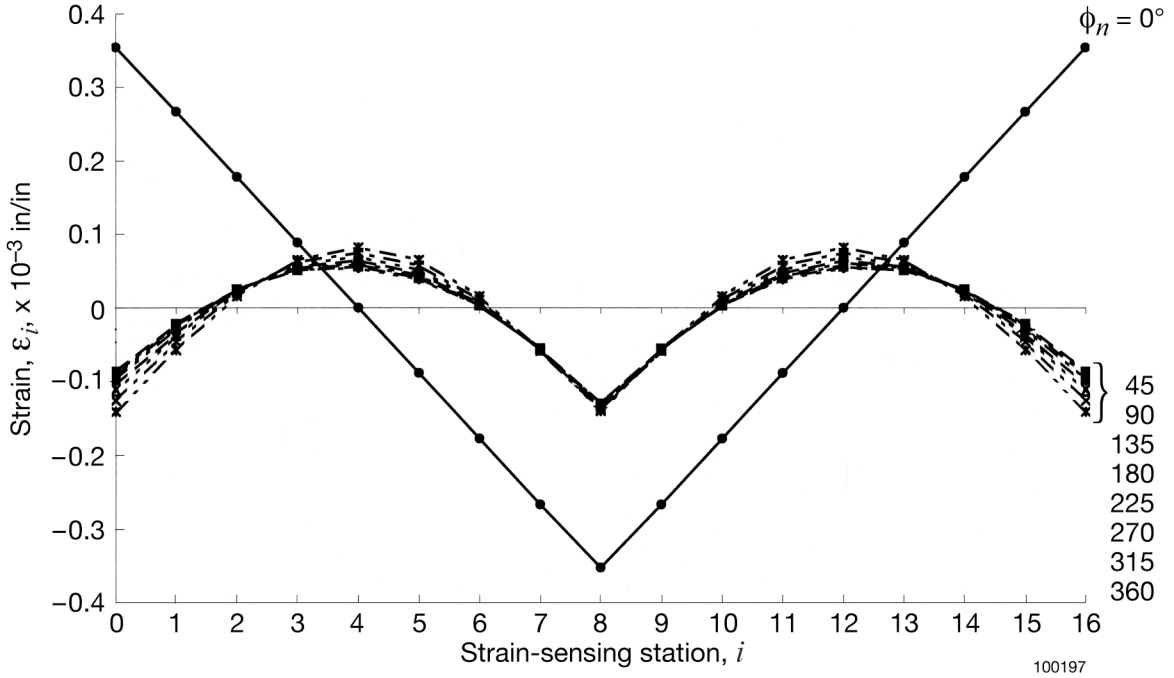


Figure 10. Bending strains, generated from SPAR, for two-point supported curved beams with different curvatures; both ends clamped; $P$ = 2 lb; $n$ = 16.

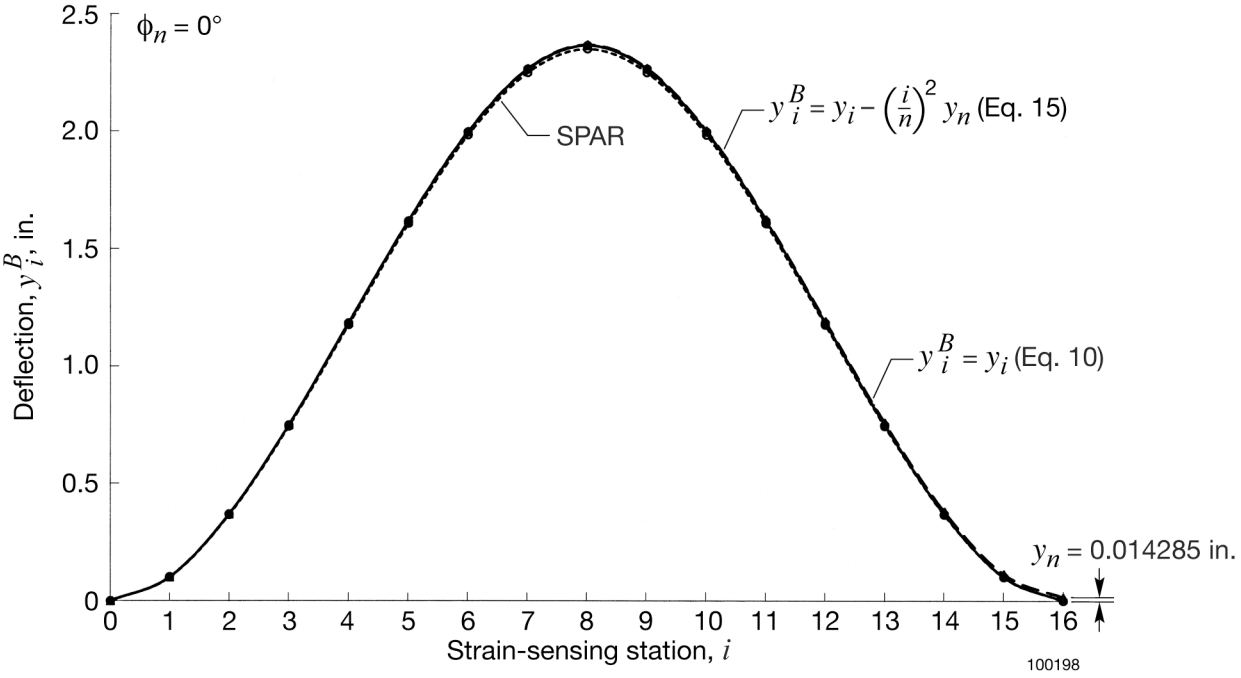


(a) $\phi_n = 0^\circ$

Figure 11. Deflection curves calculated for two-point supported curved beams with different curvatures; both ends clamped; $P$ = 2 lb; $n$ = 16.

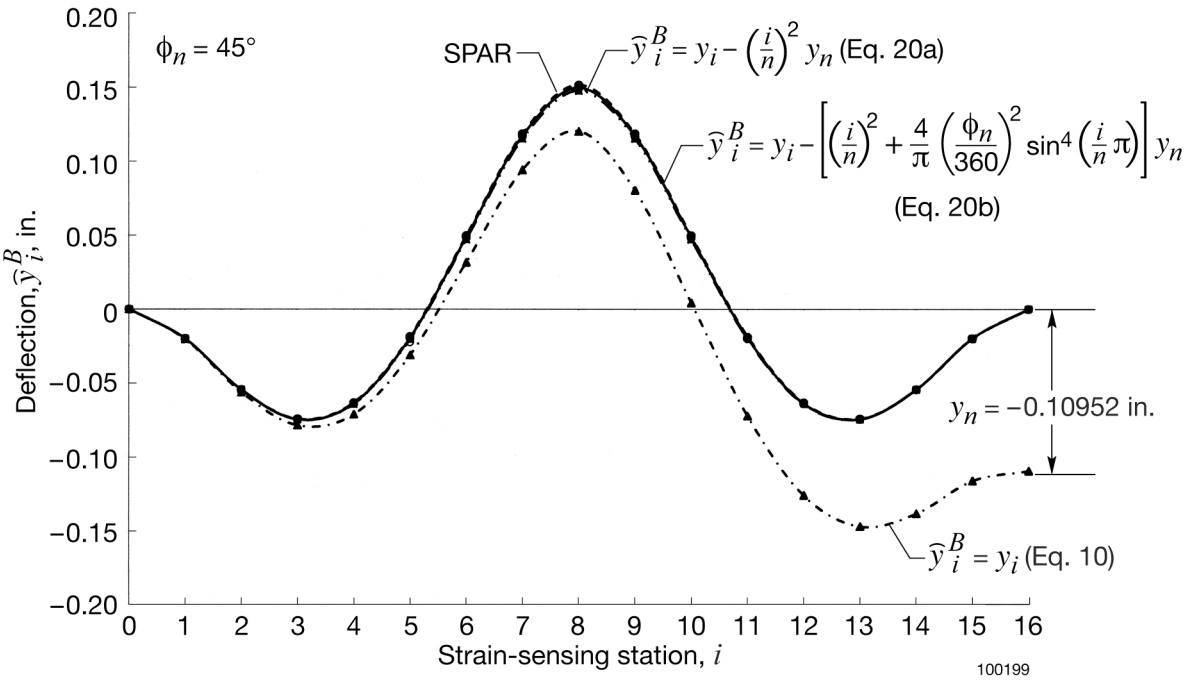


(b) $\phi_n = 45°$

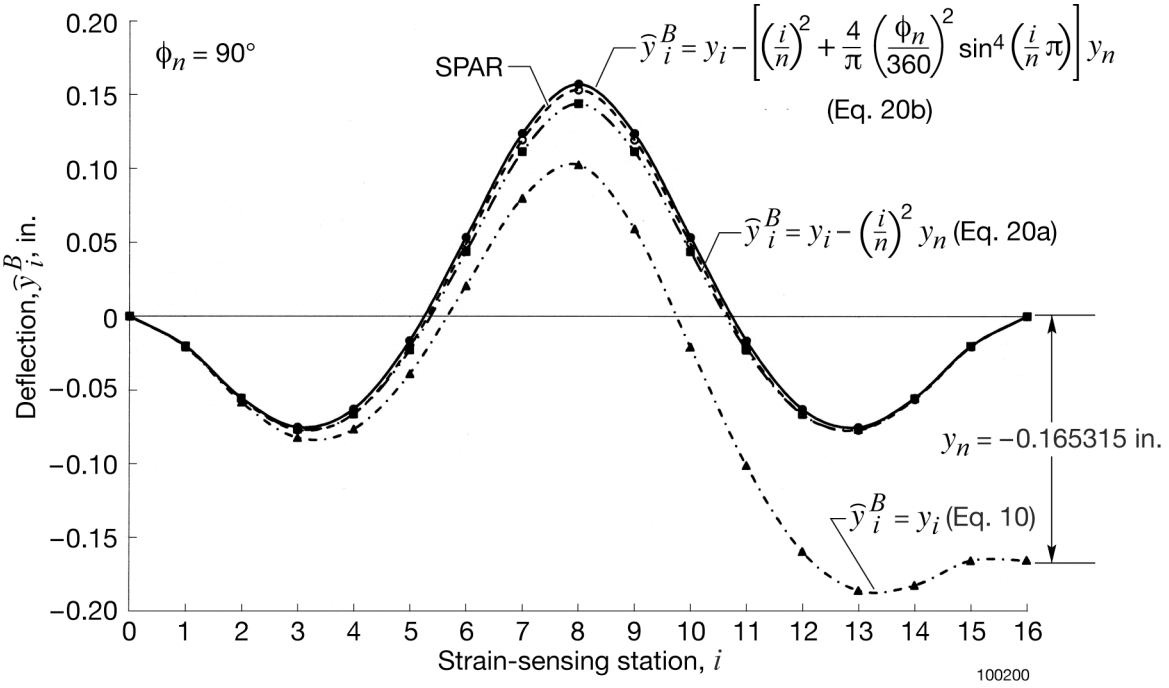


(c) $\phi_n = 90°$

Figure 11. Continued.

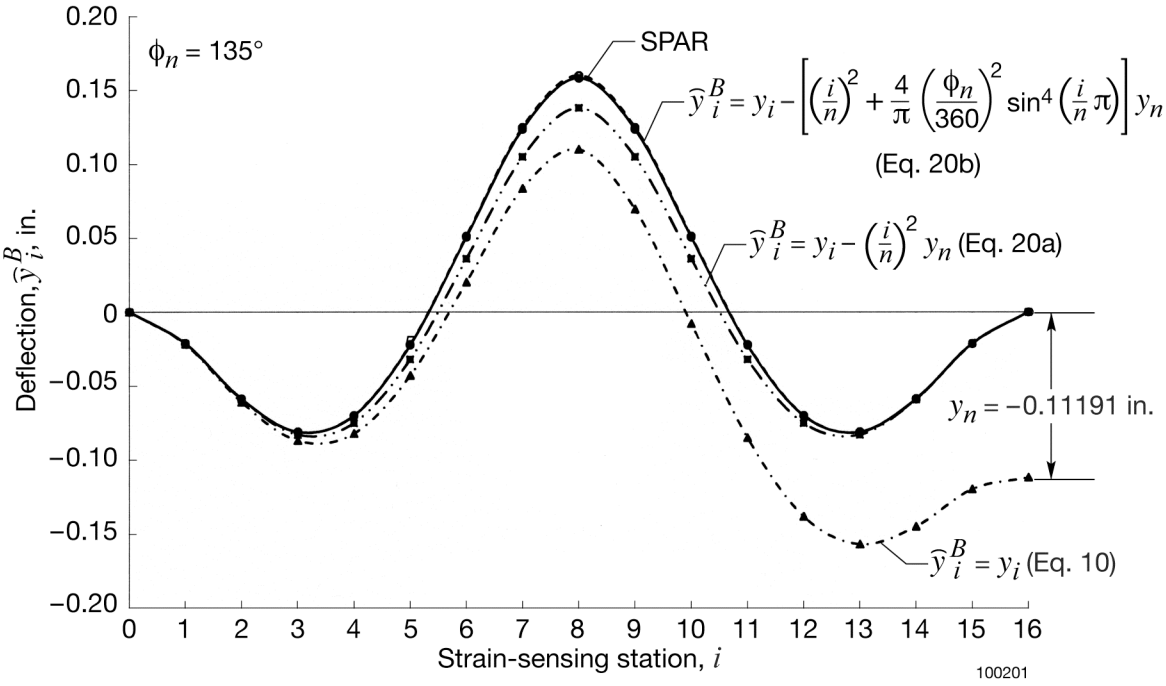


(d) $\phi_n = 135°$

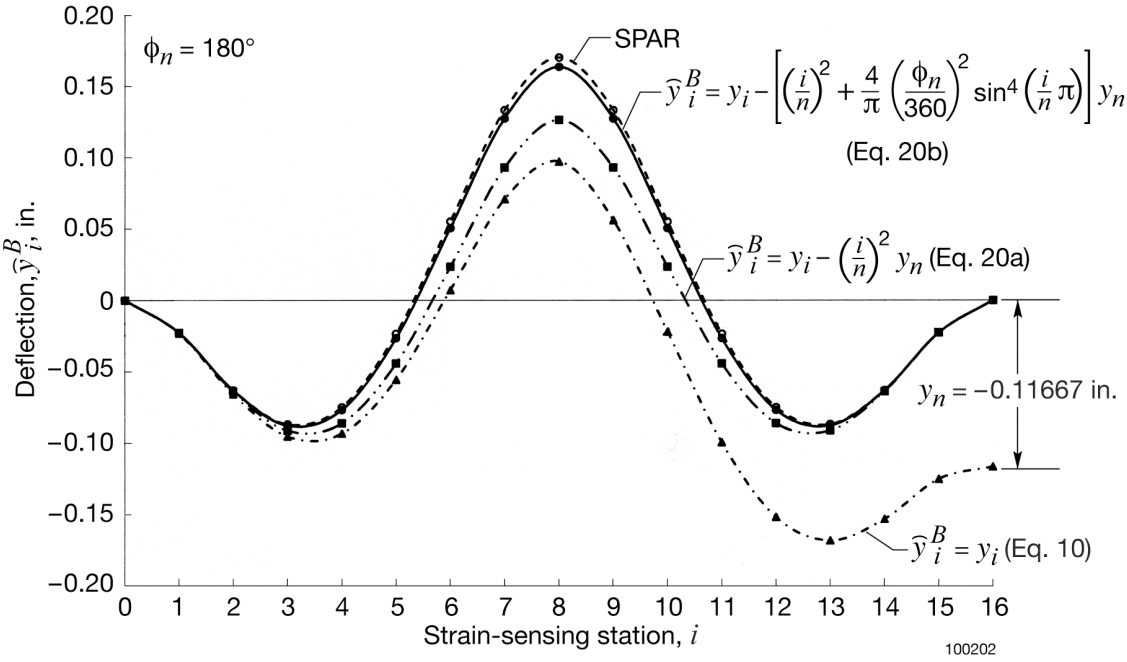


(e) $\phi_n = 180°$

Figure 11. Continued.

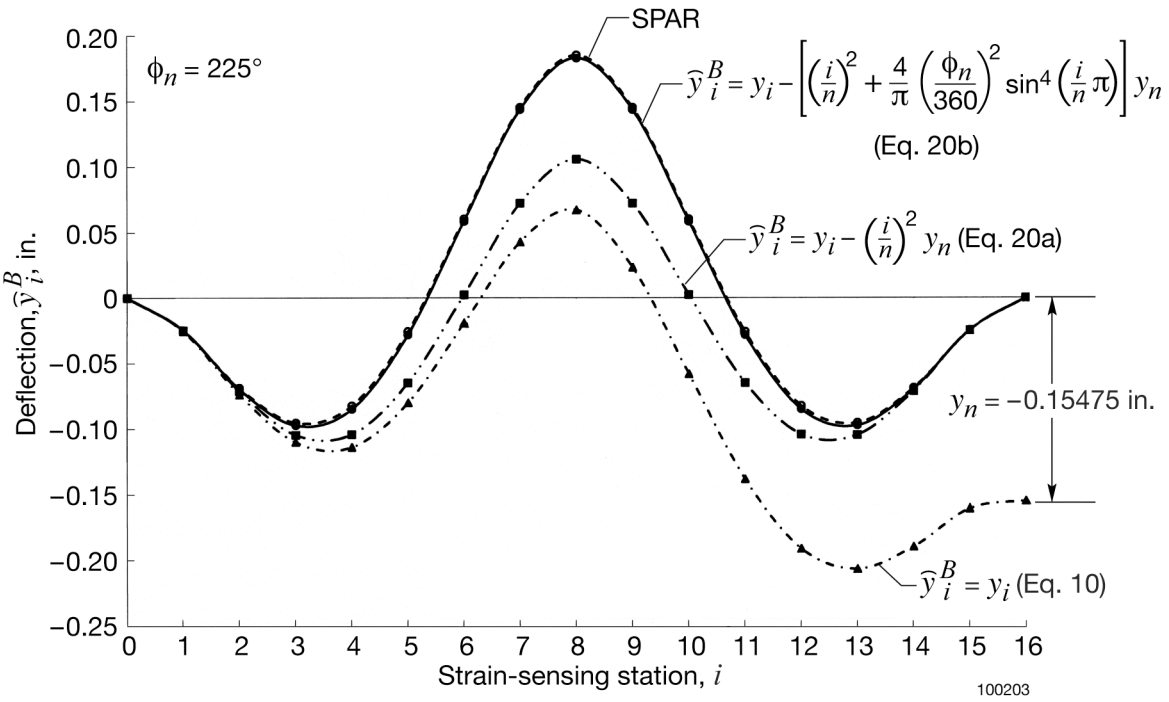


(f) $\phi_n = 225°$

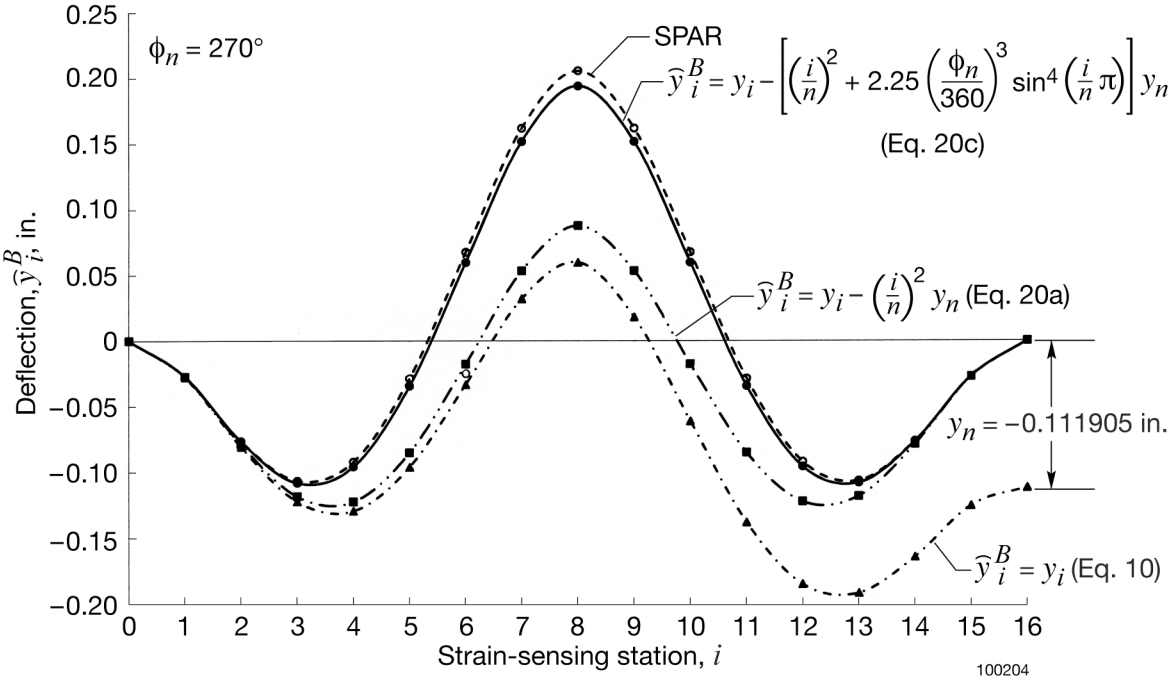


(g) $\phi_n = 270°$

Figure 11. Continued.

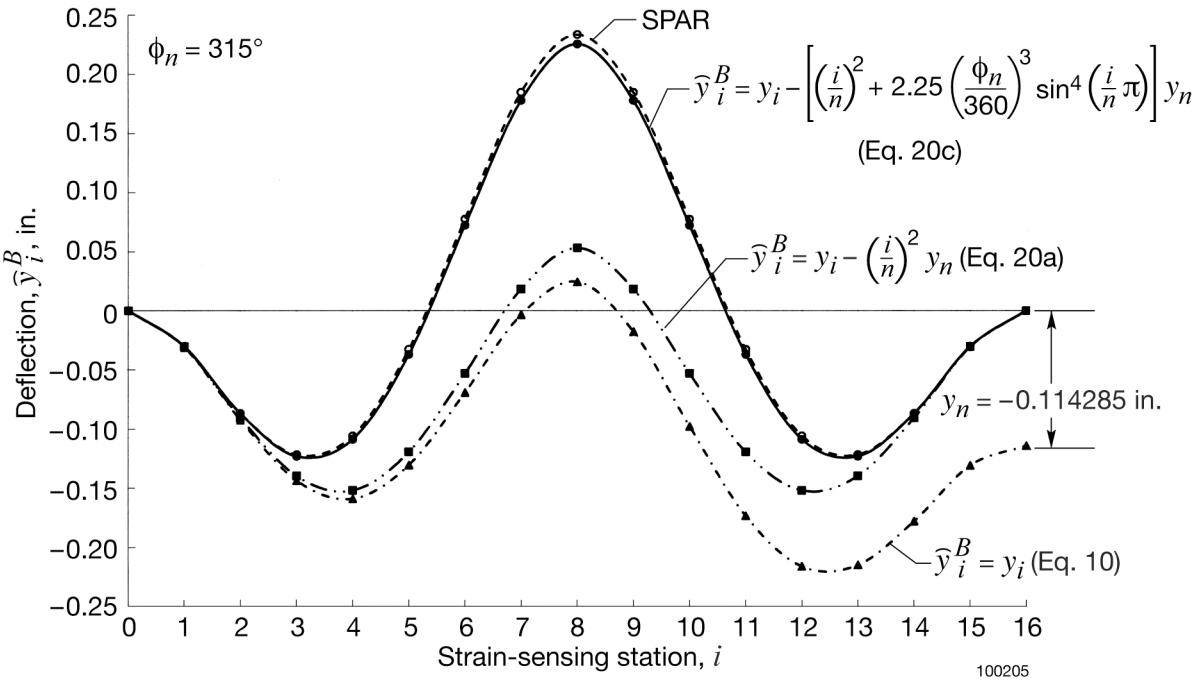


(h) $\phi_n = 315°$

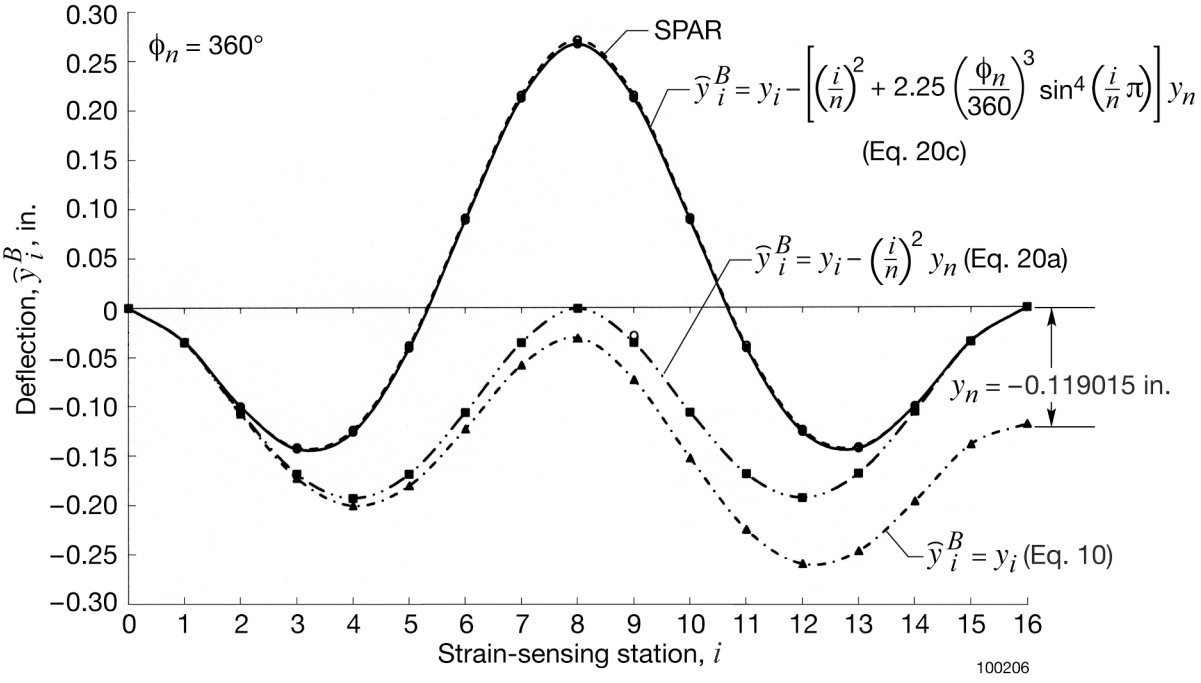


(i) $\phi_n = 360°$

Figure 11. Concluded.

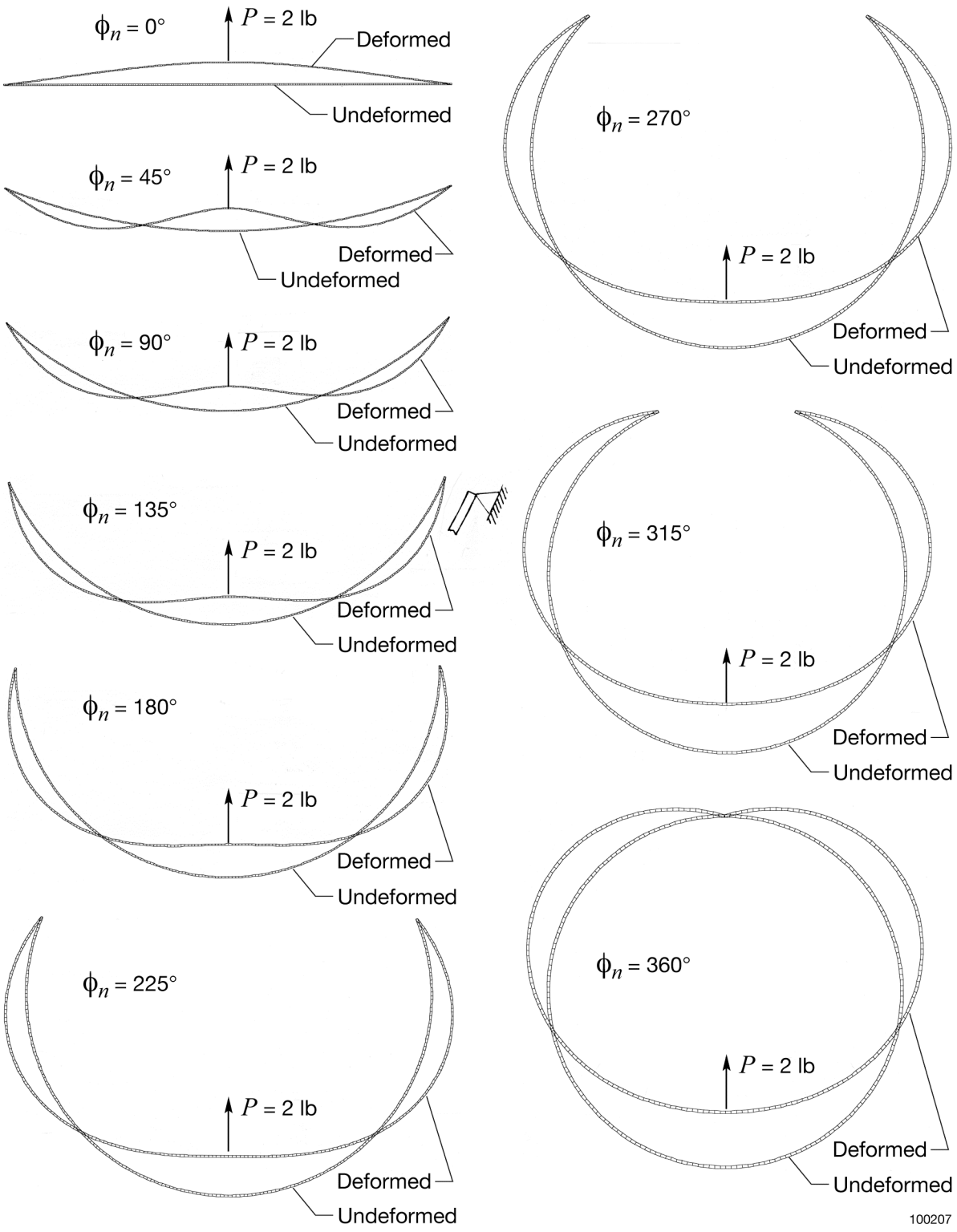


Figure 12. Deformed shapes, generated from SPAR, of two-point supported curved beams with different curvatures; both ends simply supported; $P$ = 2 lb.

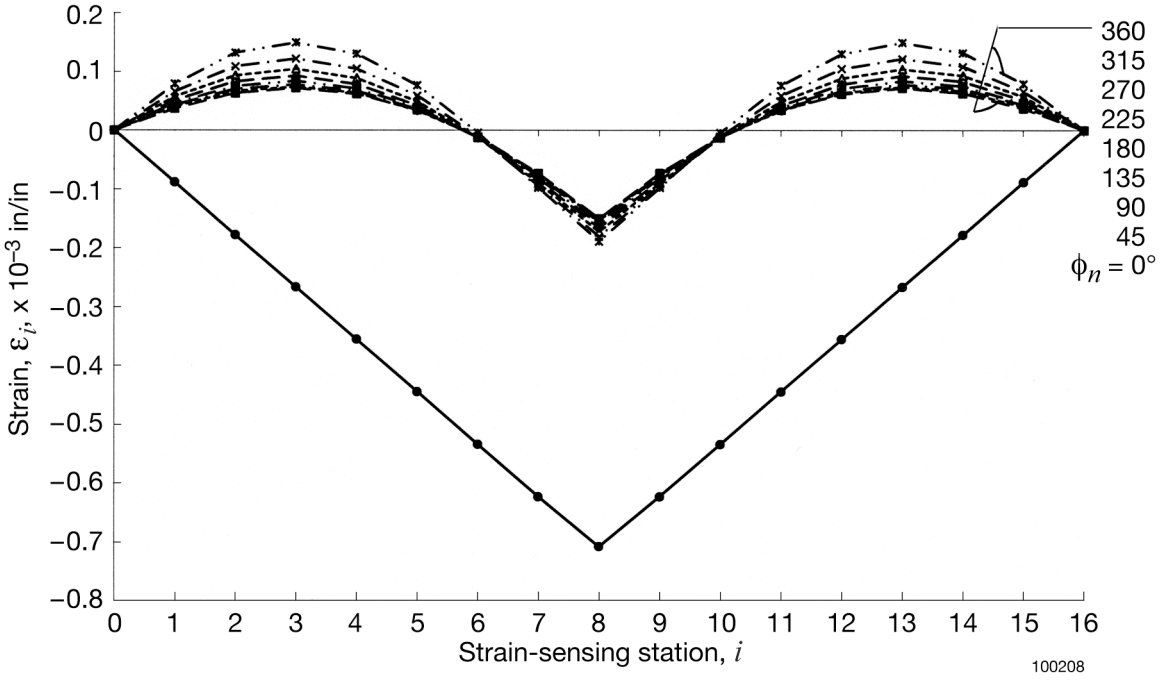


Figure 13. Bending strains, generated from SPAR, for two-point supported curved beams with different curvatures; both ends simply supported; $P$ = 2 lb; $n$ = 16.

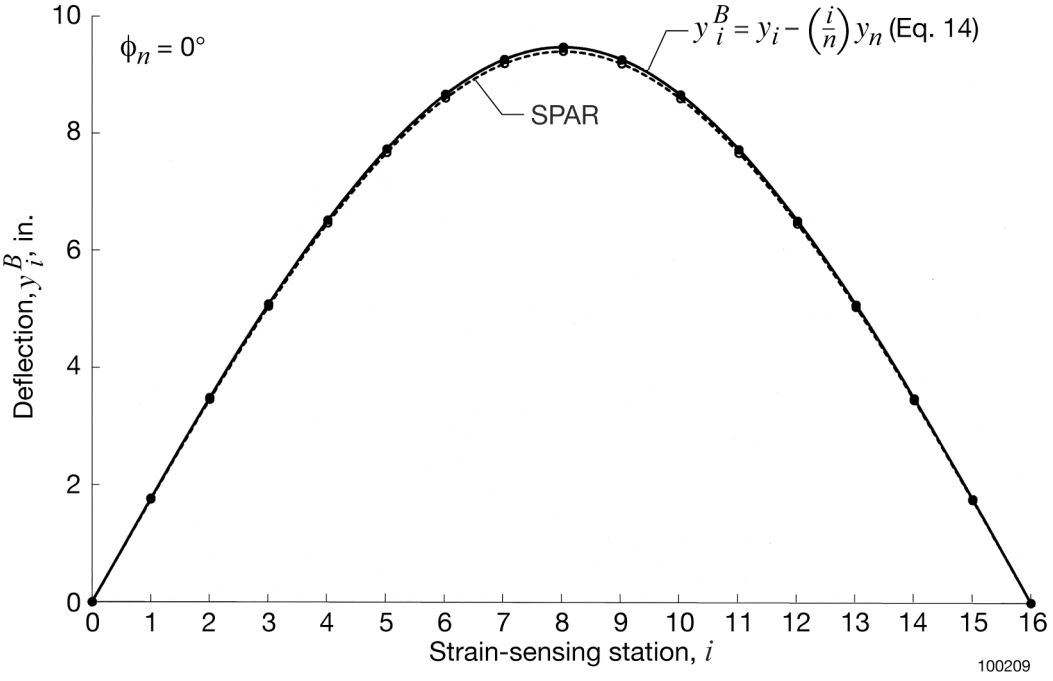


(a) $\phi_n = 0^\circ$

Figure 14. Deflection curves calculated for two-point supported curved beams with different curvatures; both ends simply supported; $P$ = 2 lb; $n$ = 16.

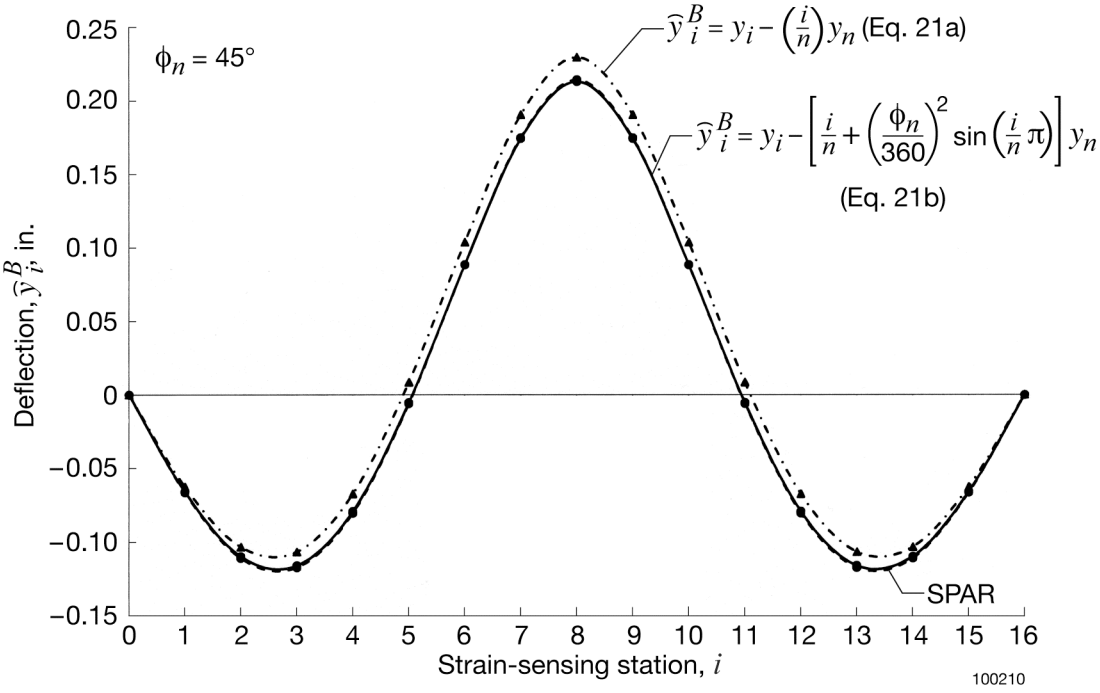


(b) $\phi_n = 45°$

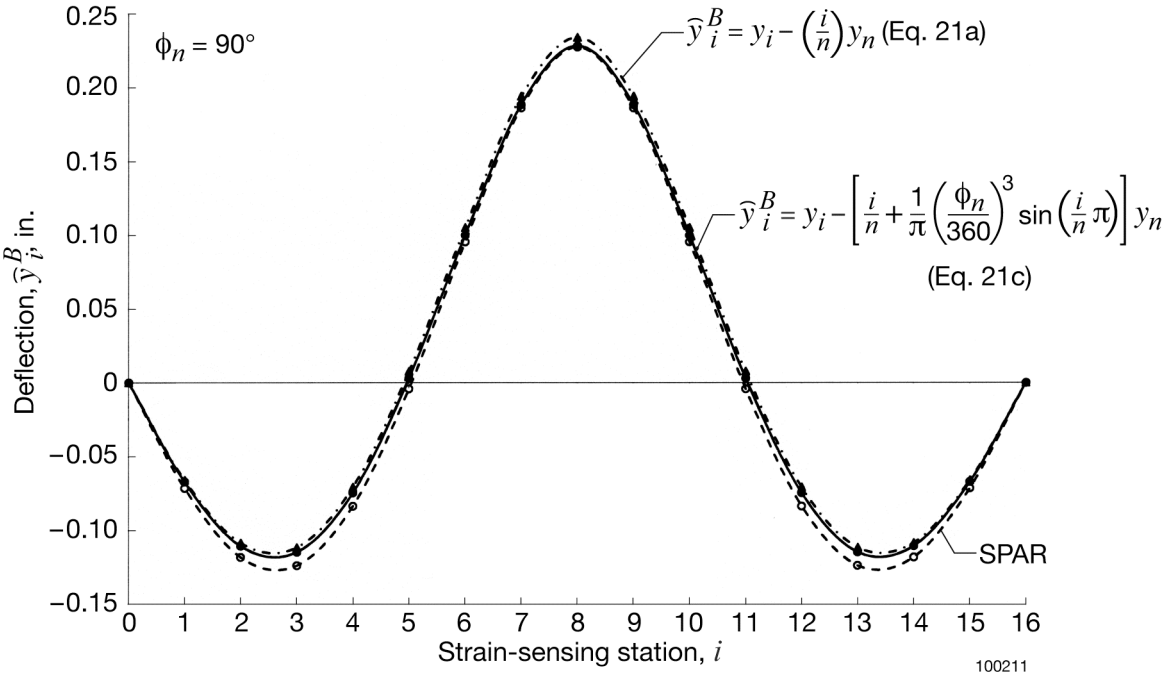


(c) $\phi_n = 90°$

Figure 14. Continued.

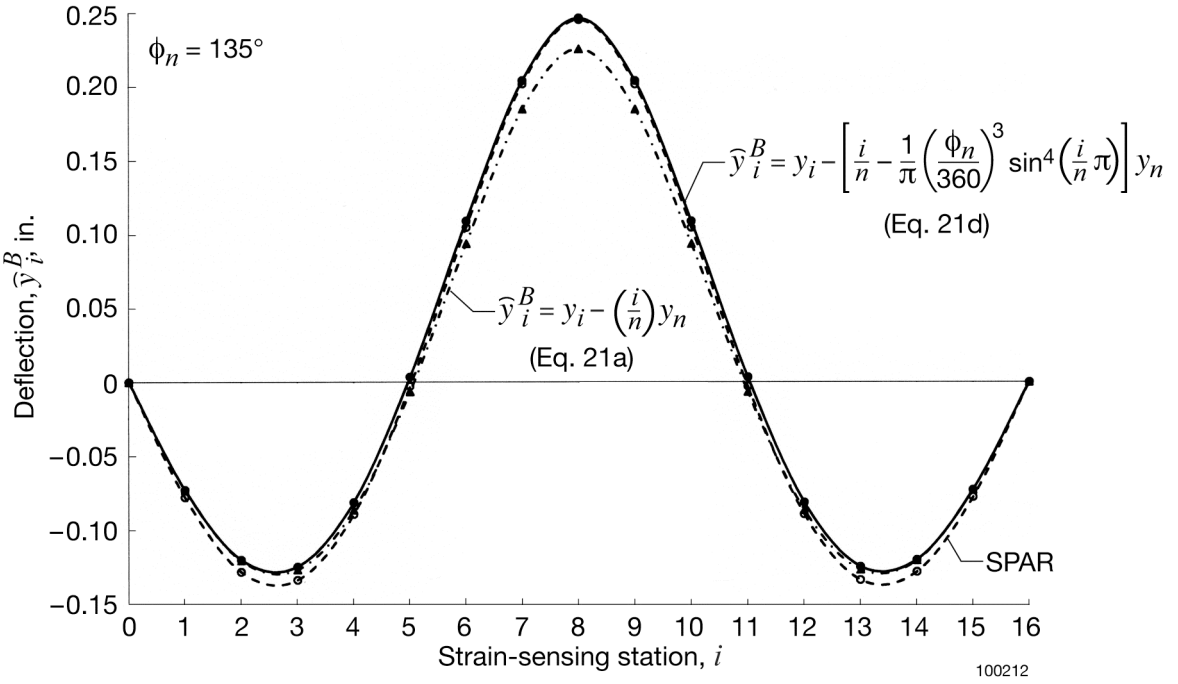


(d) $\phi_n = 135^\circ$

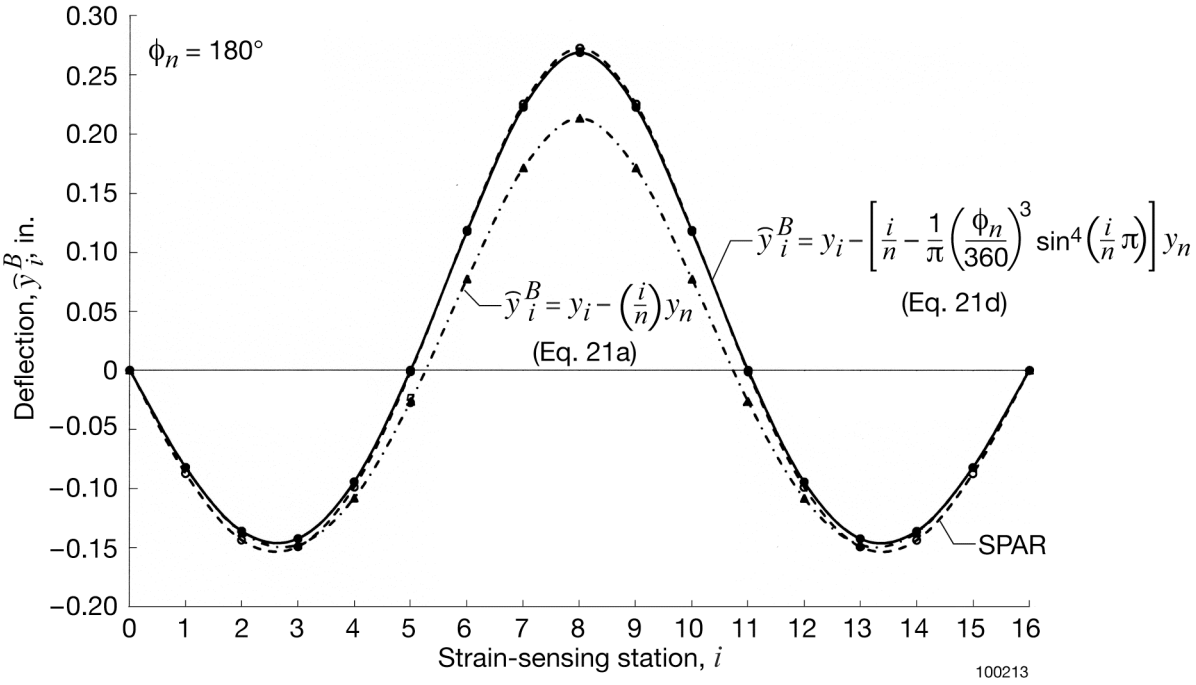


(e) $\phi_n = 180^\circ$

Figure 14. Continued.

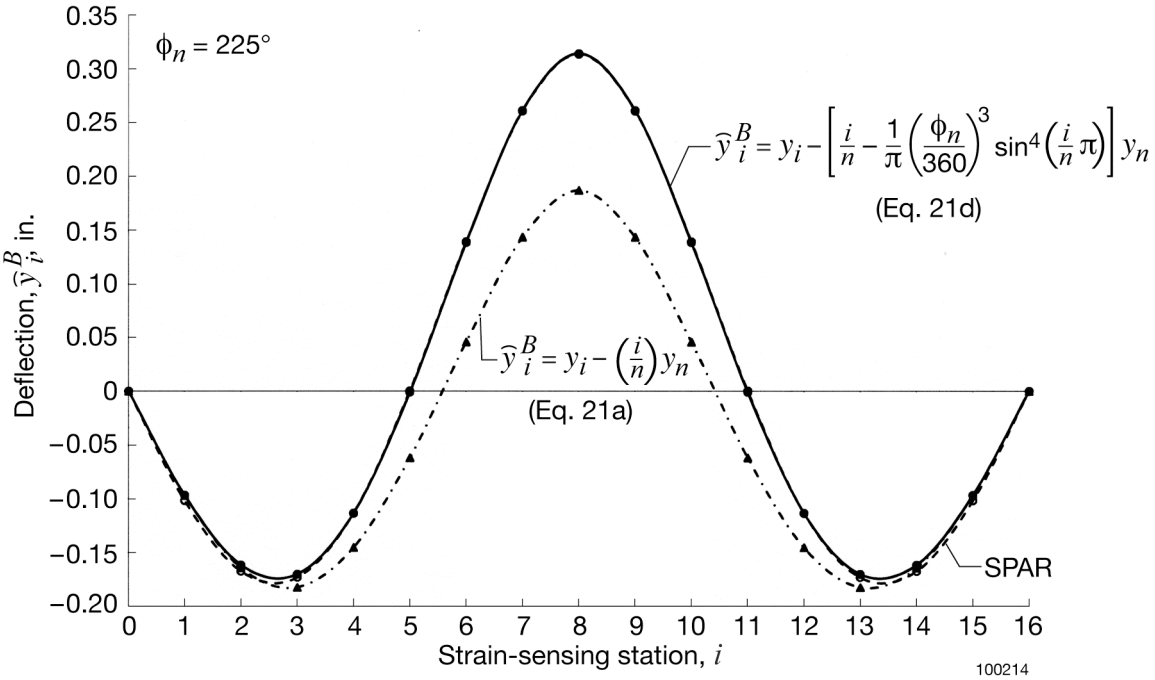


(f) $\phi_n = 225°$

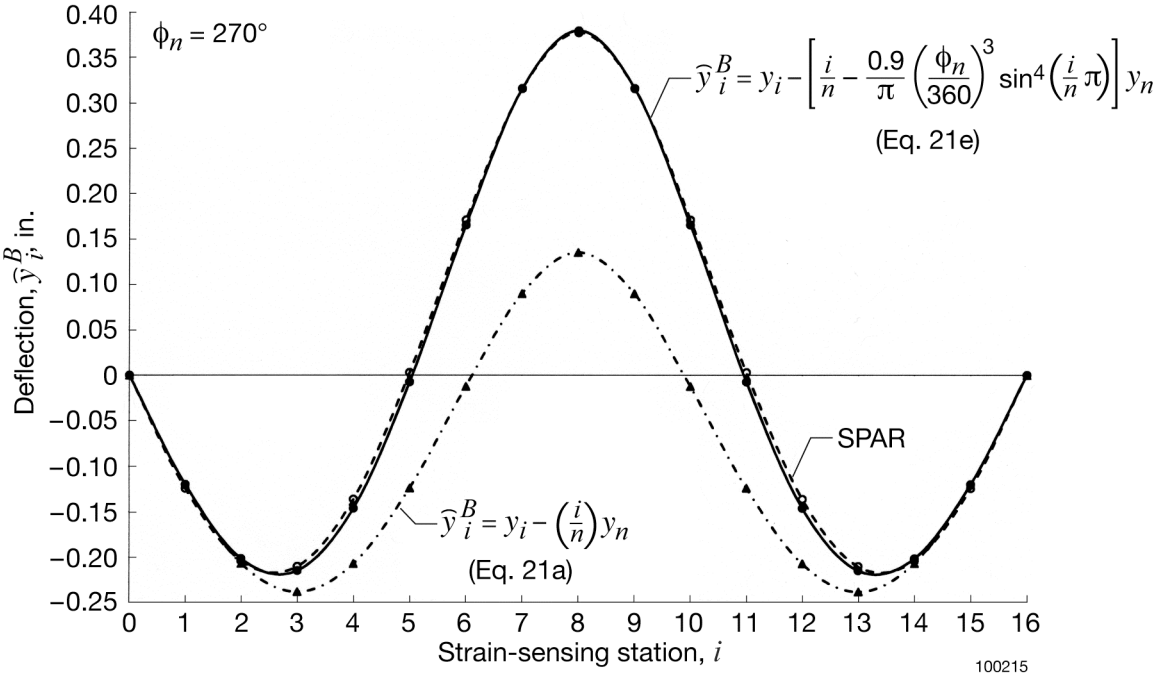


(g) $\phi_n = 270°$

Figure 14. Continued.

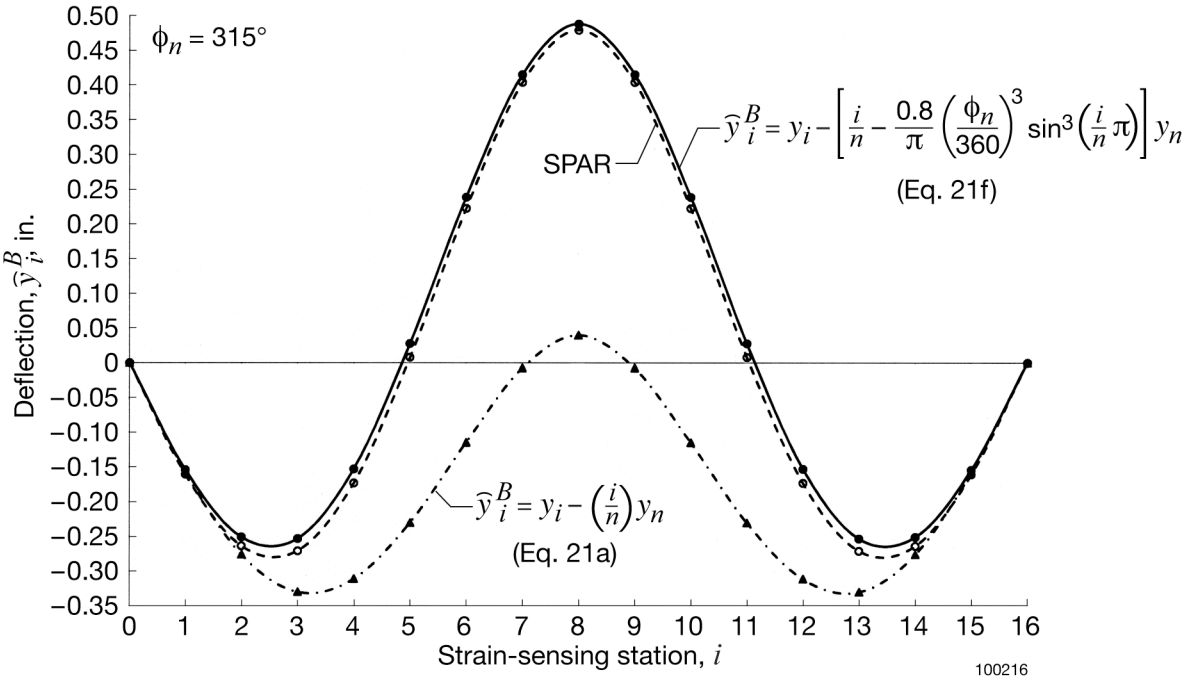


(h) $\phi_n = 315°$

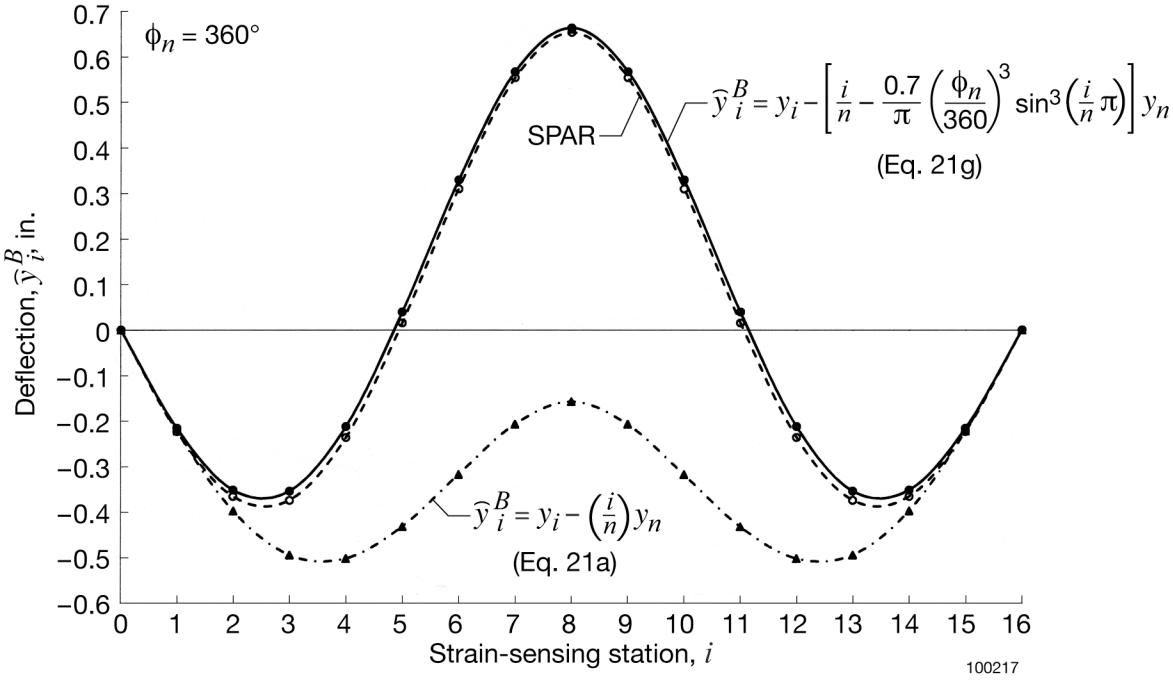


(i) $\phi_n = 360°$

Figure 14. Concluded.

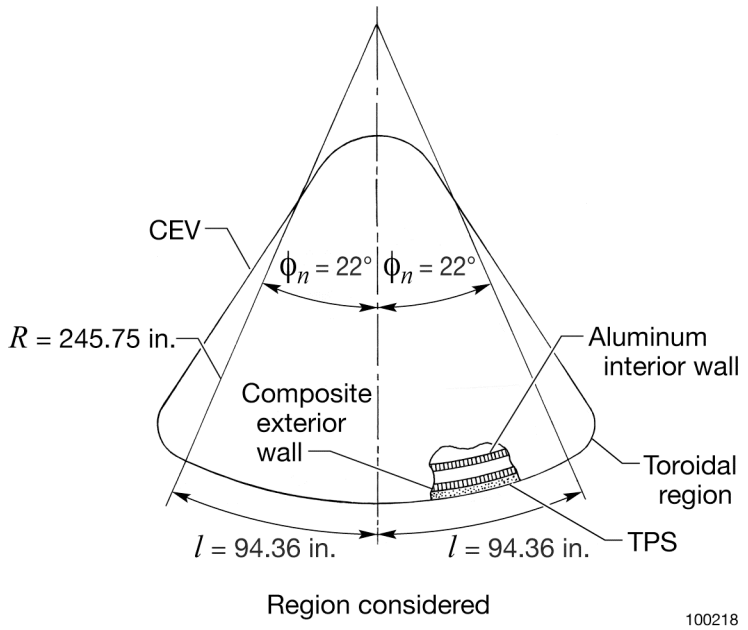


Figure 15. Generic crew exploration vehicle fabricated with dual sandwich wall structures.

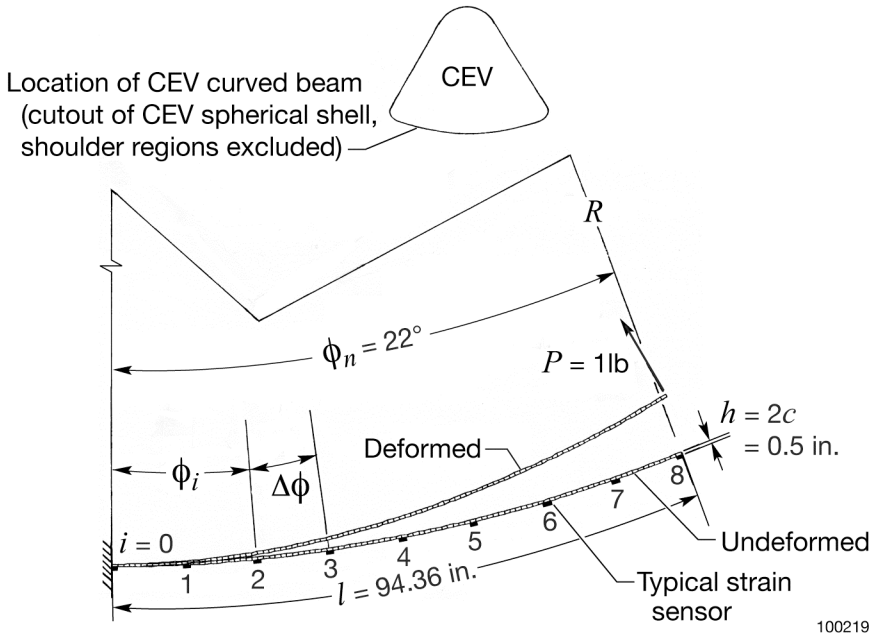


Figure 16. Crew exploration vehicle cantilever curved beam subjected to a tip load of $P$ = 1 lb.

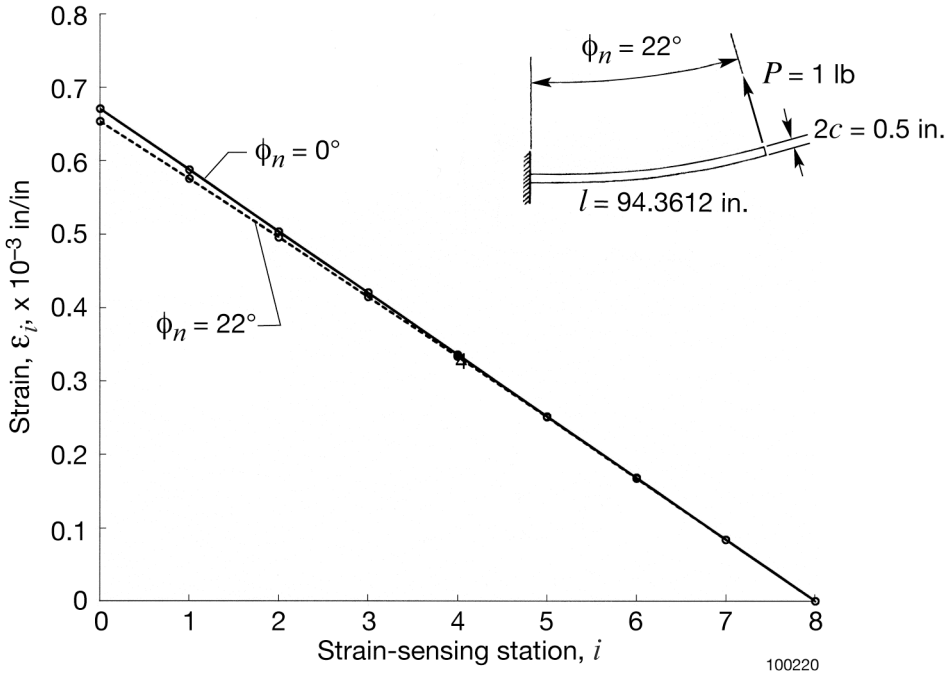


Figure 17. Bending strains, generated from SPAR, for crew exploration vehicle cantilever curved beam and equivalent straight beam; $P$ = 1 lb; $n$ = 8.

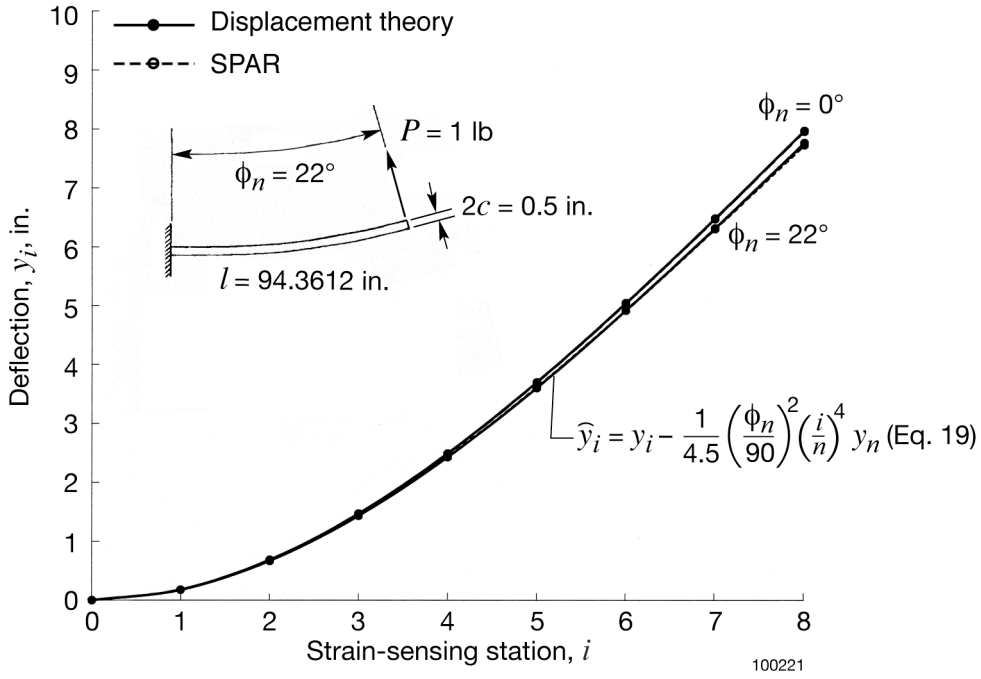


Figure 18. Comparison of SPAR deflection curves with corresponding predicted deflection curves calculated from deflection equations (10) and (19) for crew exploration vehicle cantilever curved beam and equivalent straight beam, respectively; $P$ = 1; $n$ = 8 lb.

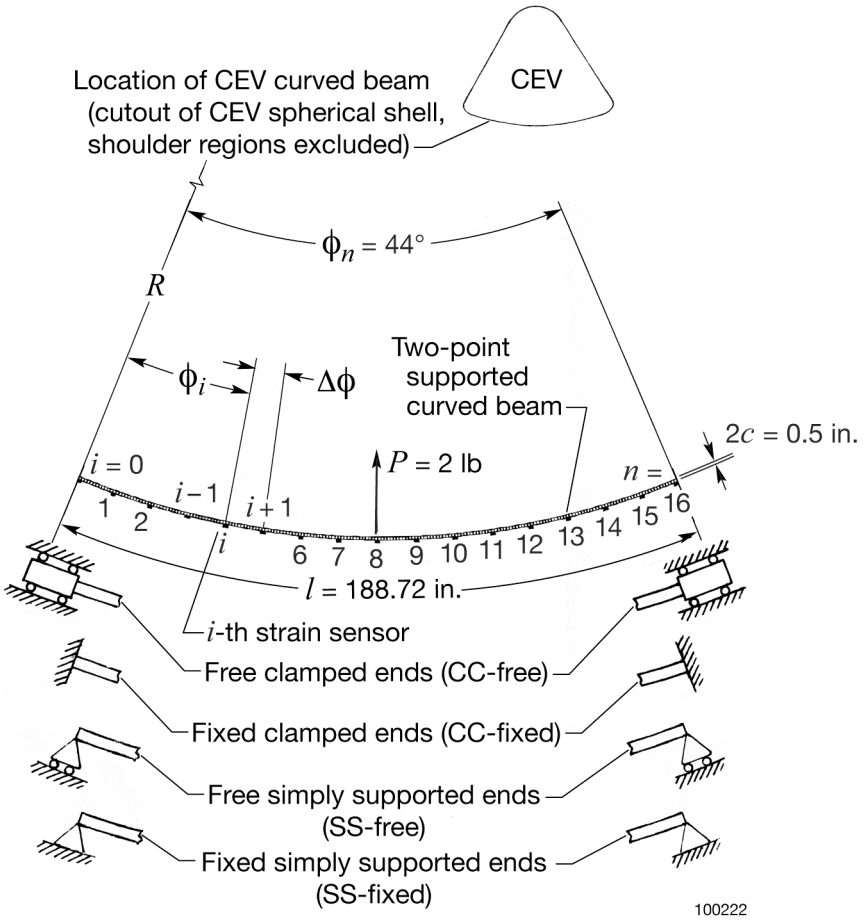


Figure 19. Crew exploration vehicle two-point supported curved beam under different support conditions subjected to a central load of $P$ = 2 lb.

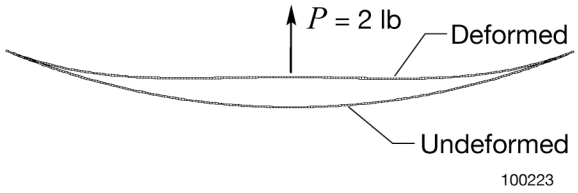


(a) Both ends clamped and free to move along beam curve (CC-free).

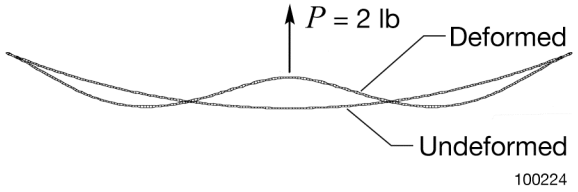


(b) Both ends clamped and stationary (CC-fixed).

Figure 20. Deformed shapes, generated from SPAR, of crew exploration vehicle two-point supported curved beams; both ends clamped; $P$ = 2 lb.

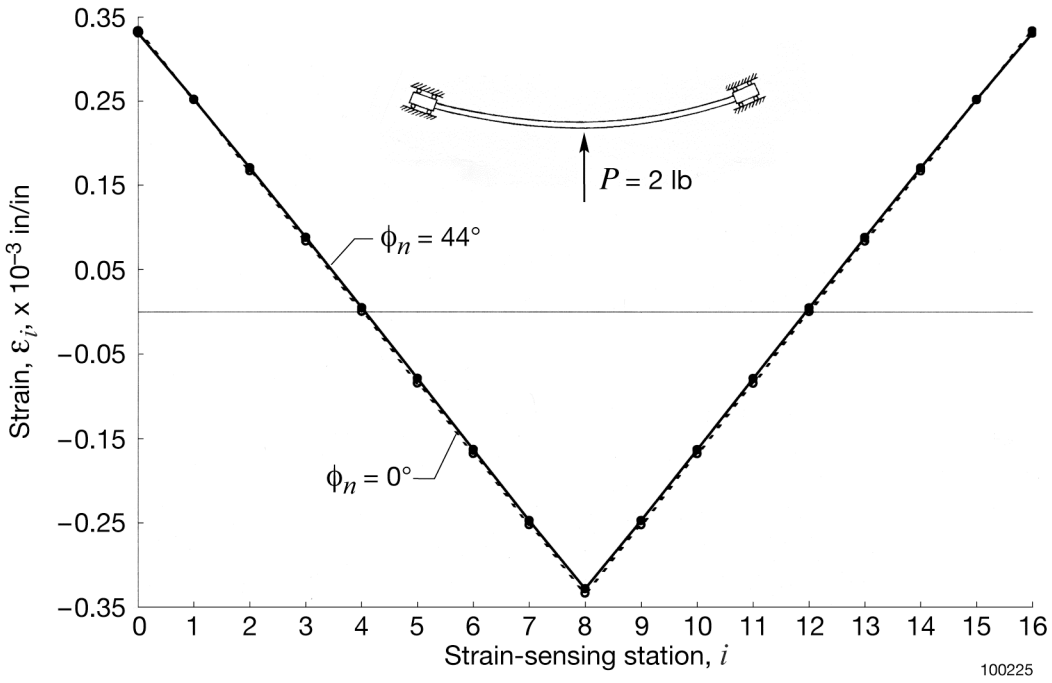


Figure 21. Comparison of SPAR bending strains for crew exploration vehicle two-point supported curved beam and equivalent straight beam; both ends clamped and free to move along beam curve (CC-free); $P$ = 2 lb; $n$ = 16.

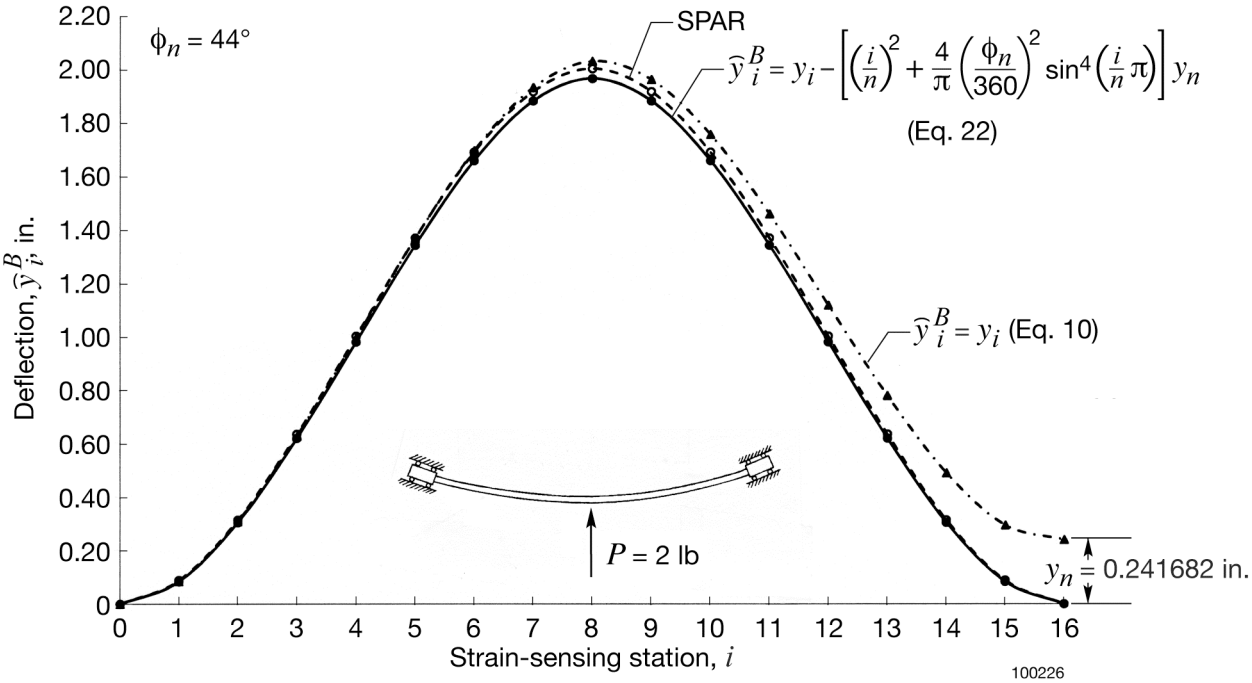


Figure 22. Comparison of SPAR deflection curve with predicted deflection curve based on curved-beam deflection equation (22) for crew exploration vehicle two-point supported curved beam; both ends clamped and free to move along beam curve (CC-free); $P$ = 2 lb; $n$ = 16.

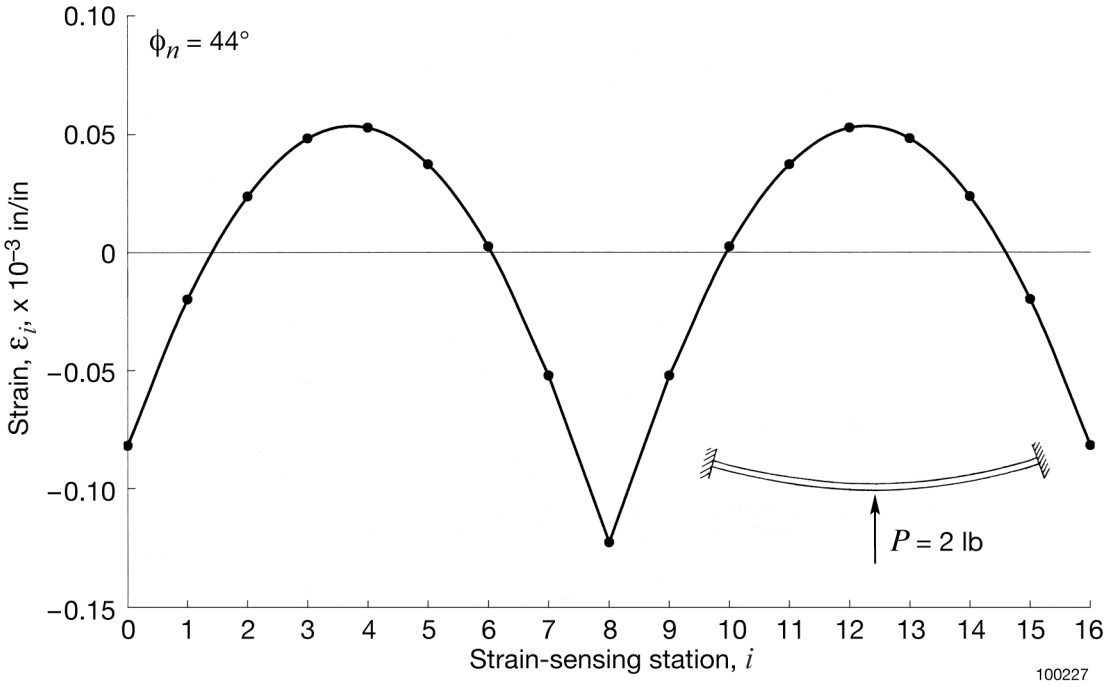


Figure 23. Bending strains, generated from SPAR, for crew exploration vehicle two-point supported curved beam; both ends clamped and stationary (CC-fixed); $P$ = 2 lb; $n$ = 16.

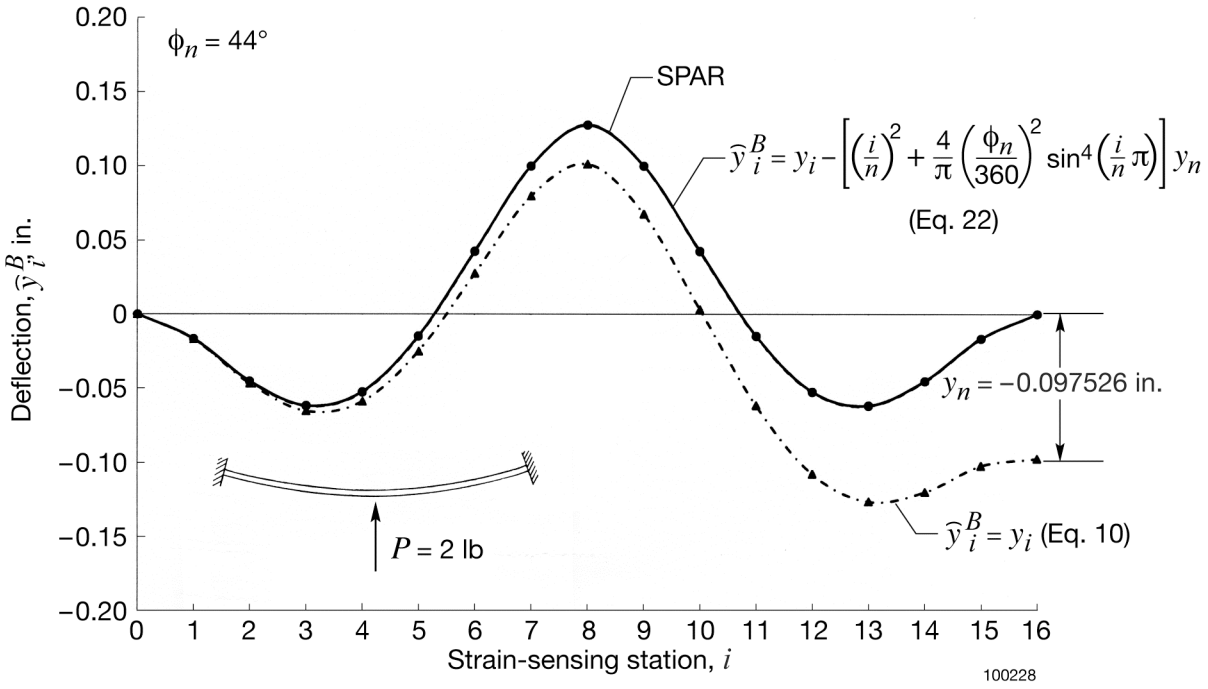


Figure 24. Comparison of SPAR deflection curve with predicted deflection curve based on curved-beam deflection equation (22) for crew exploration vehicle two-point supported curved beam; both ends clamped and stationary (CC-fixed); $P$ = 2 lb; $n$ = 16.

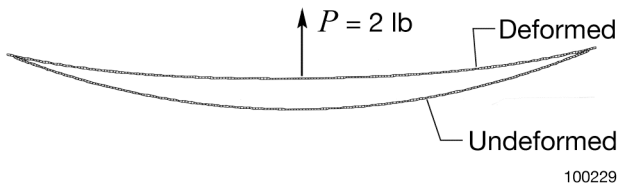


(a) Both ends simply supported and free to move along beam curve (SS-free).

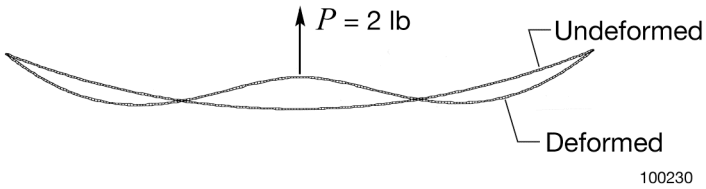


(b) Both ends simply supported and stationary (SS-fixed).

Figure 25. Deformed shapes, generated from SPAR, of crew exploration vehicle two-point supported curved beams; both ends simply supported; $P$ = 2 lb.

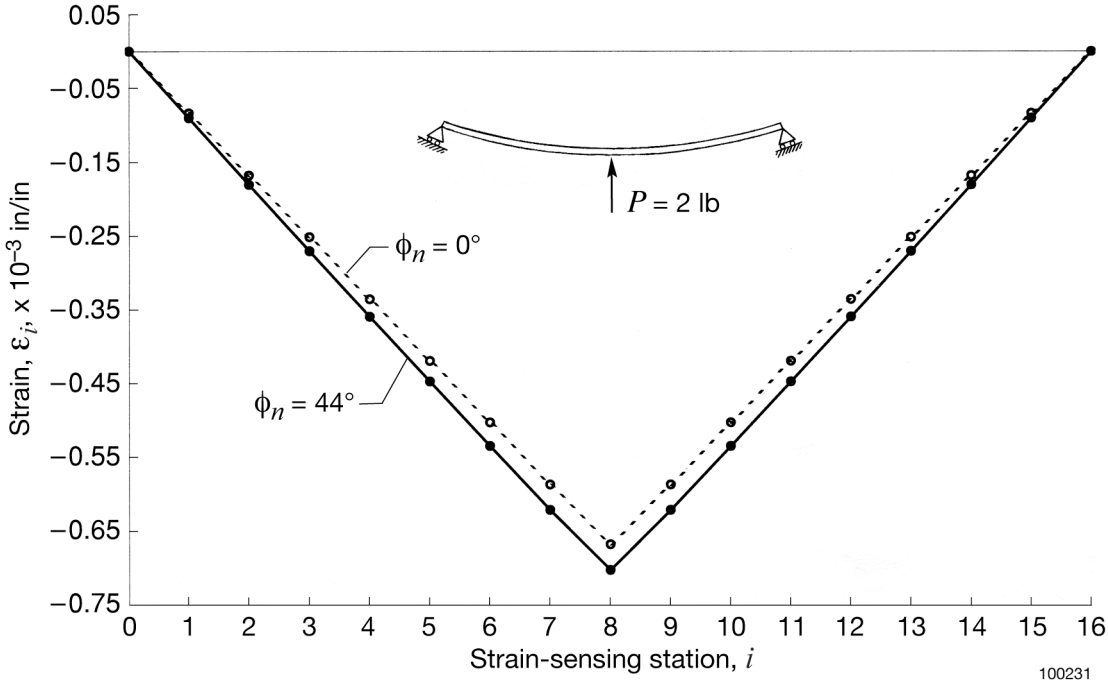


Figure 26. Comparison of SPAR bending strains for crew exploration vehicle two-point supported curved beam and equivalent straight beam; both ends simply supported and free to move along beam curve (SS-free); $P$ = 2 lb; $n$ = 16.

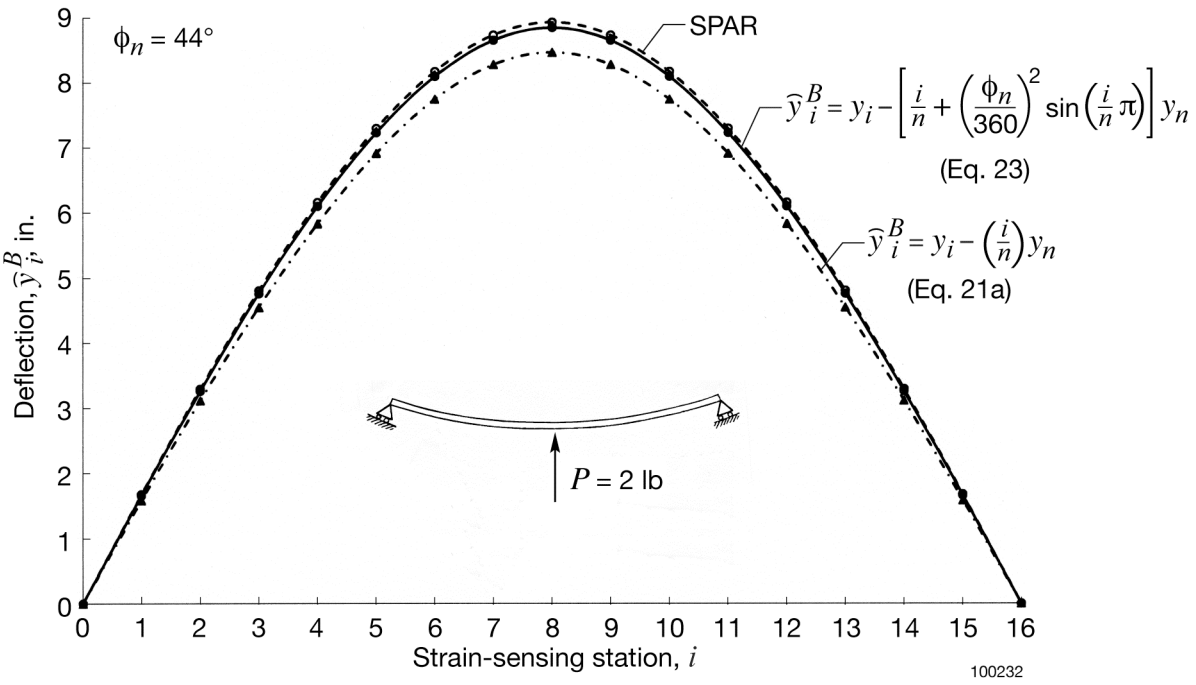


Figure 27. Comparison of SPAR deflection curve with predicted deflection curve based on curved-beam deflection equation (23) for crew exploration vehicle two-point supported curved beam; both ends simply supported and free to move along beam curve (SS-free); $P$ = 2 lb; $n$ = 16.

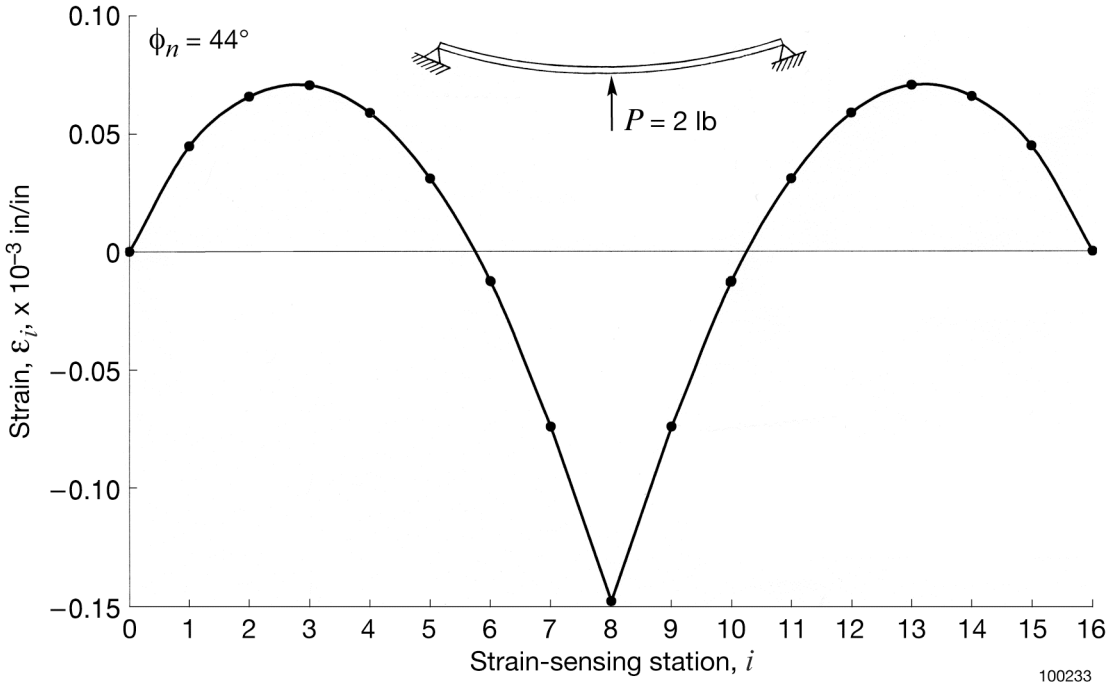


Figure 28. Bending strains, generated from SPAR, for crew exploration vehicle two-point supported curved beam; both ends simply supported and stationary (SS-fixed); $P$ = 2 lb; $n$ = 16.

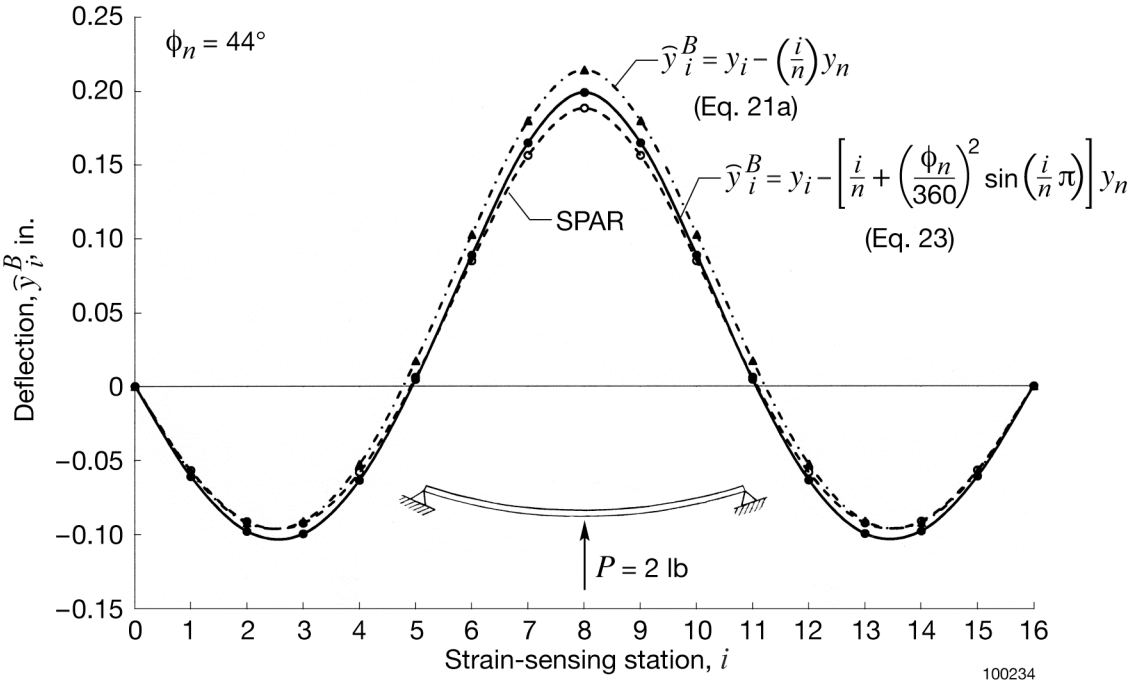


Figure 29. Comparison of SPAR deflection curve with predicted deflection curve based on curved-beam deflection equation (23) for crew exploration vehicle two-point supported curved beam; both ends simply supported and stationary (SS-fixed); $P$ = 2 lb; $n$ = 16.

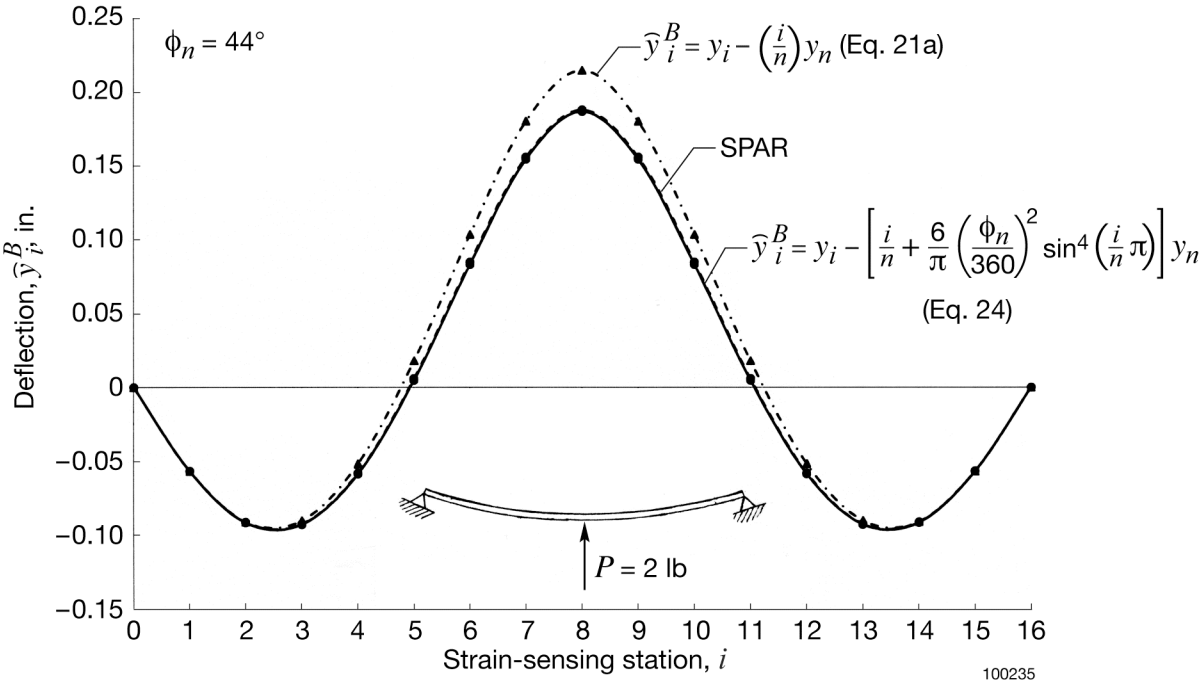


Figure 30. Comparison of SPAR deflection curve with predicted deflection curve based on curved-beam deflection equation (24) for crew exploration vehicle two-point supported curved beam; both ends simply supported and stationary (SS-fixed); $P$ = 2 lb; $n$ = 16.

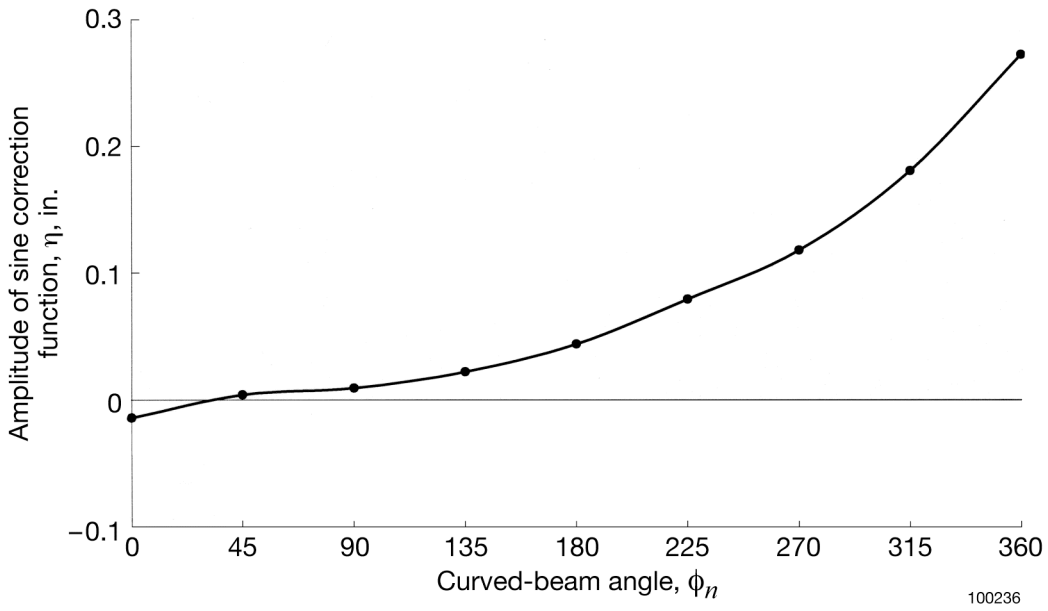


Figure 31. Plot of amplitude of sine correction function, $\eta$, as a function of curved-beam angle, $\phi_n$, for the clamped curved beam; $n = 16$.

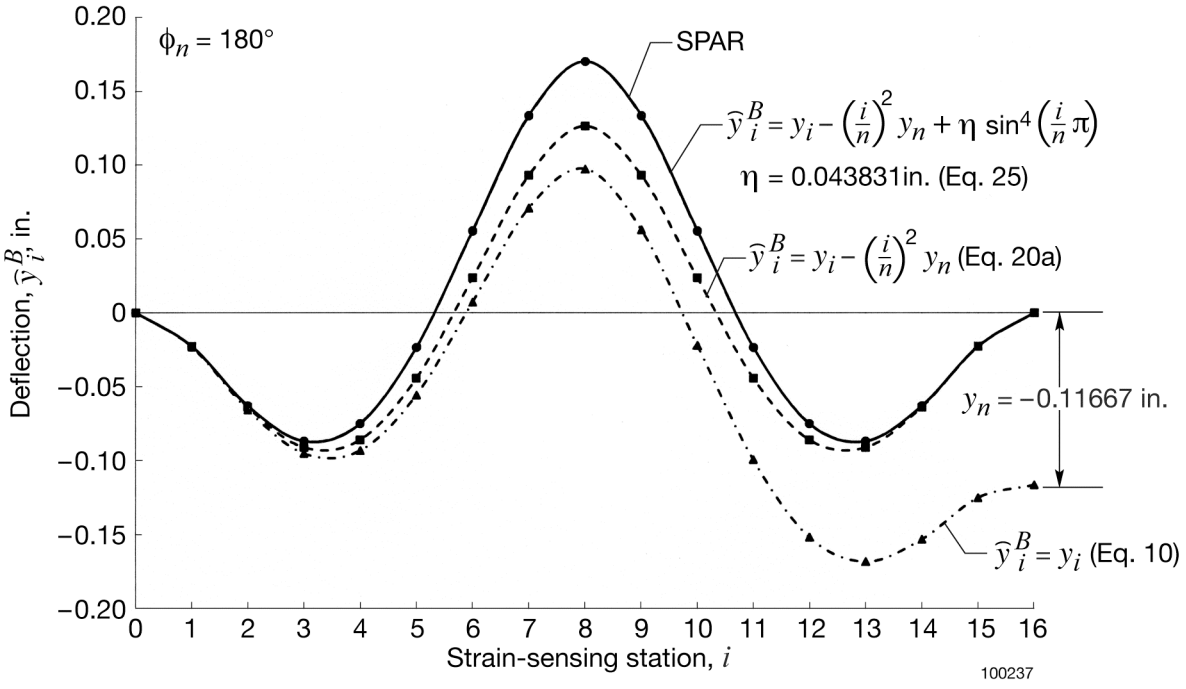


Figure 32. Comparison of SPAR deflection curve with single-point collocation deflection curves for the clamped curved beam; $\phi_n = 180°$; $P = 2$ lb; $n = 16$.

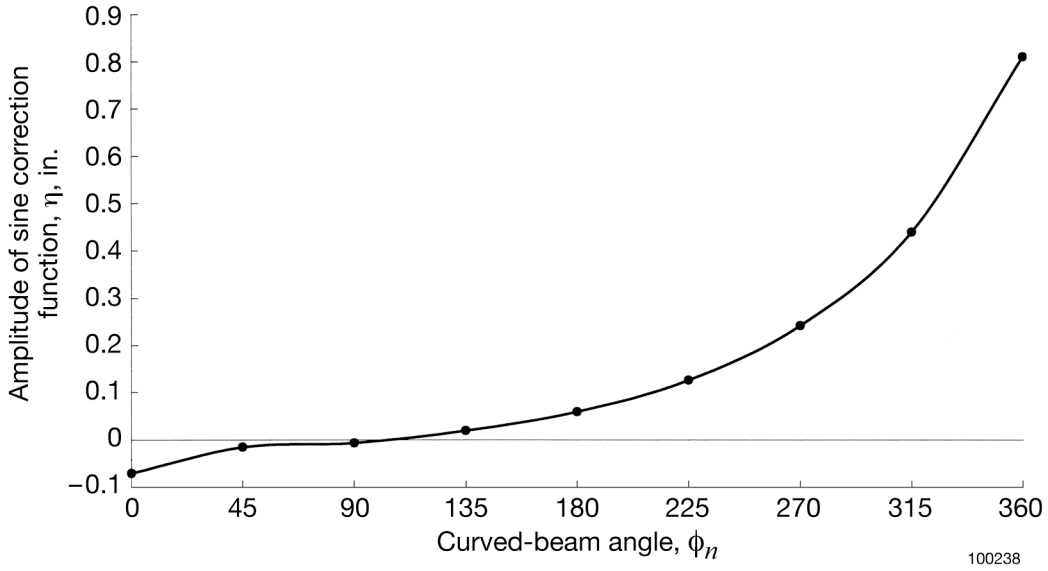


Figure 33. Plot of amplitude of sine correction function, $\eta$, as a function of curved-beam angle, $\phi_n$, for the simply supported curved beam; $n$ = 16.

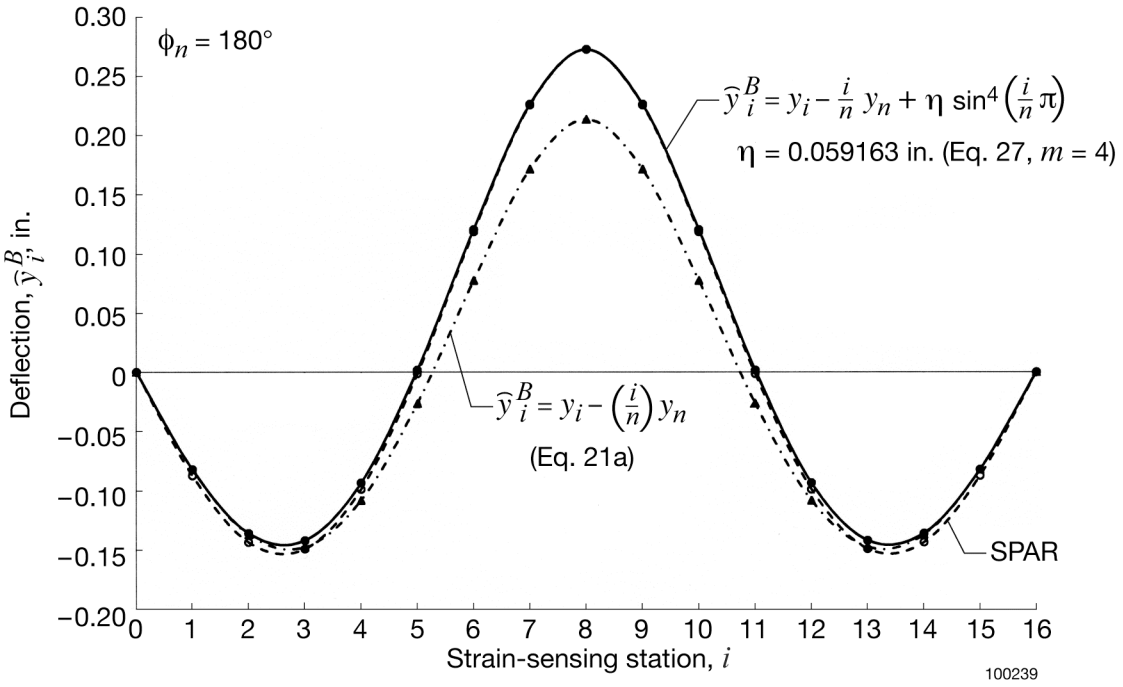


Figure 34. Comparison of SPAR deflection curve with single-point collocation deflection curves for the simply supported curved beam; $\phi_n$ = 180°; $P$ = 2 lb; $n$ = 16.

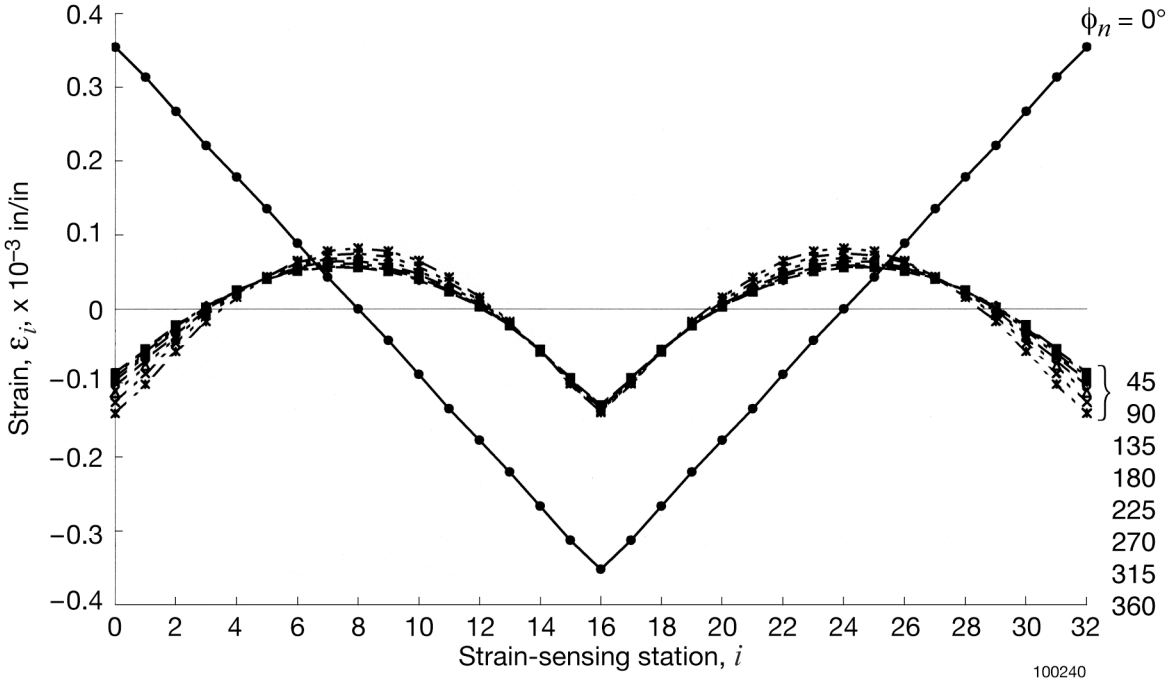


Figure 35. Bending strains, generated from SPAR, for the clamped curved beam; $P$ = 2 lb; $n$ = 32.

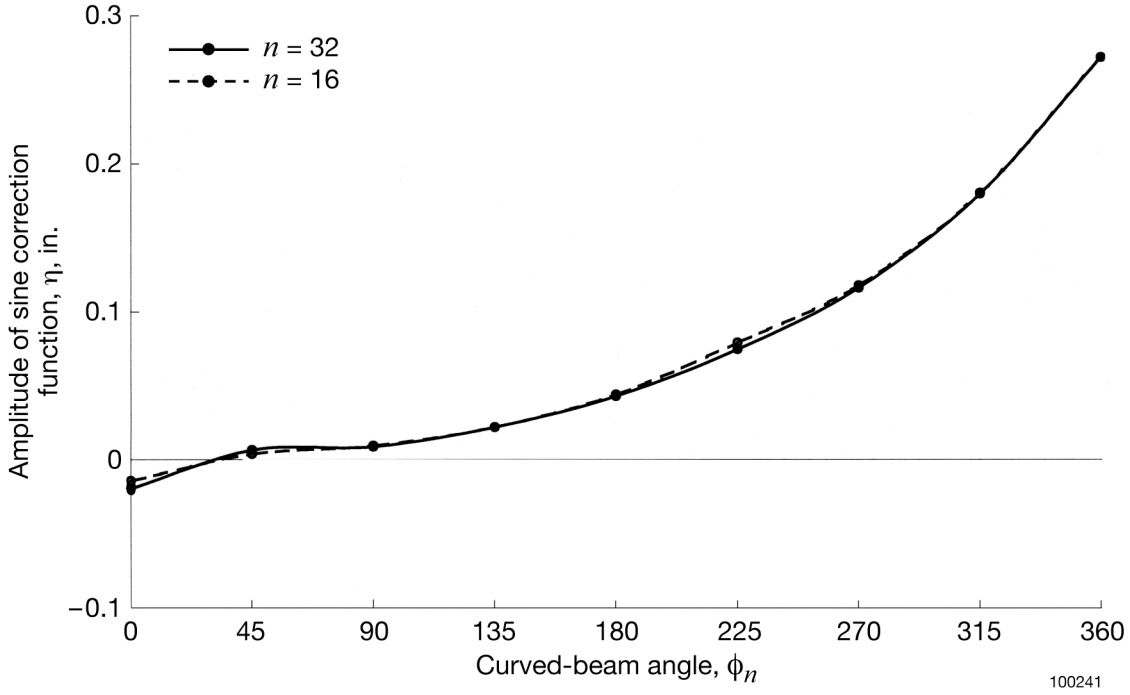


Figure 36. Plot of amplitude of sine correction function, $\eta$, as a function of curved-beam angle, $\phi_n$, for the clamped curved beam; $n$ = 32.

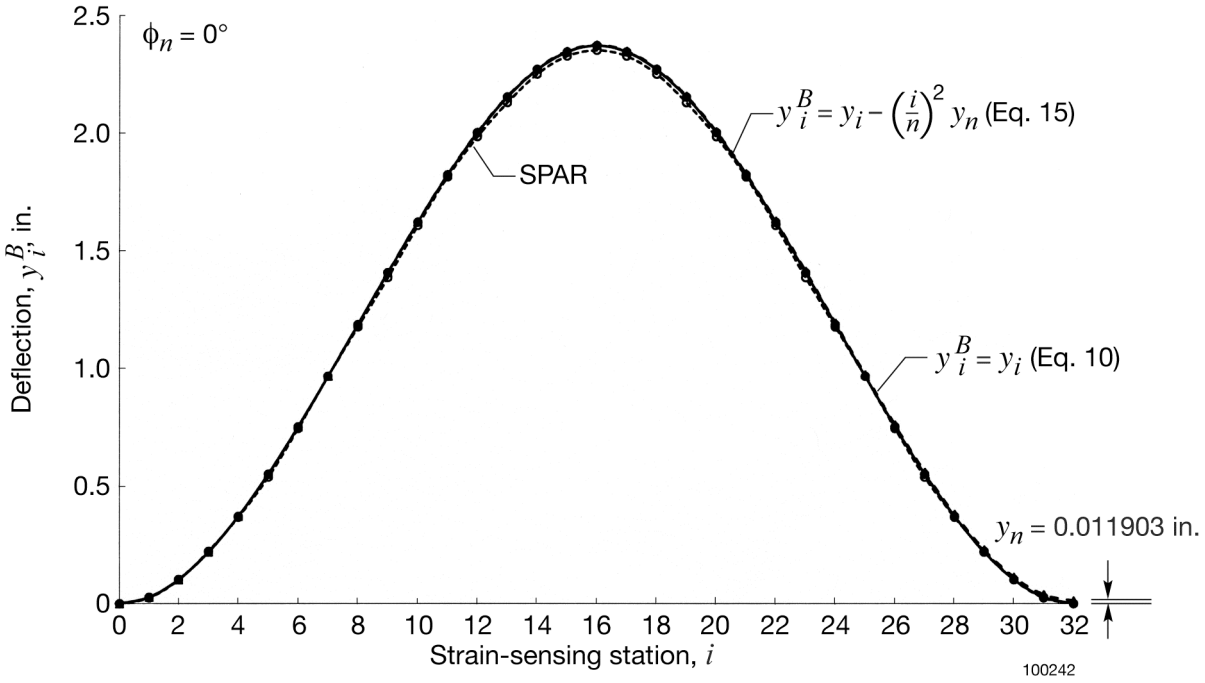


(a) $\phi_n = 0°$

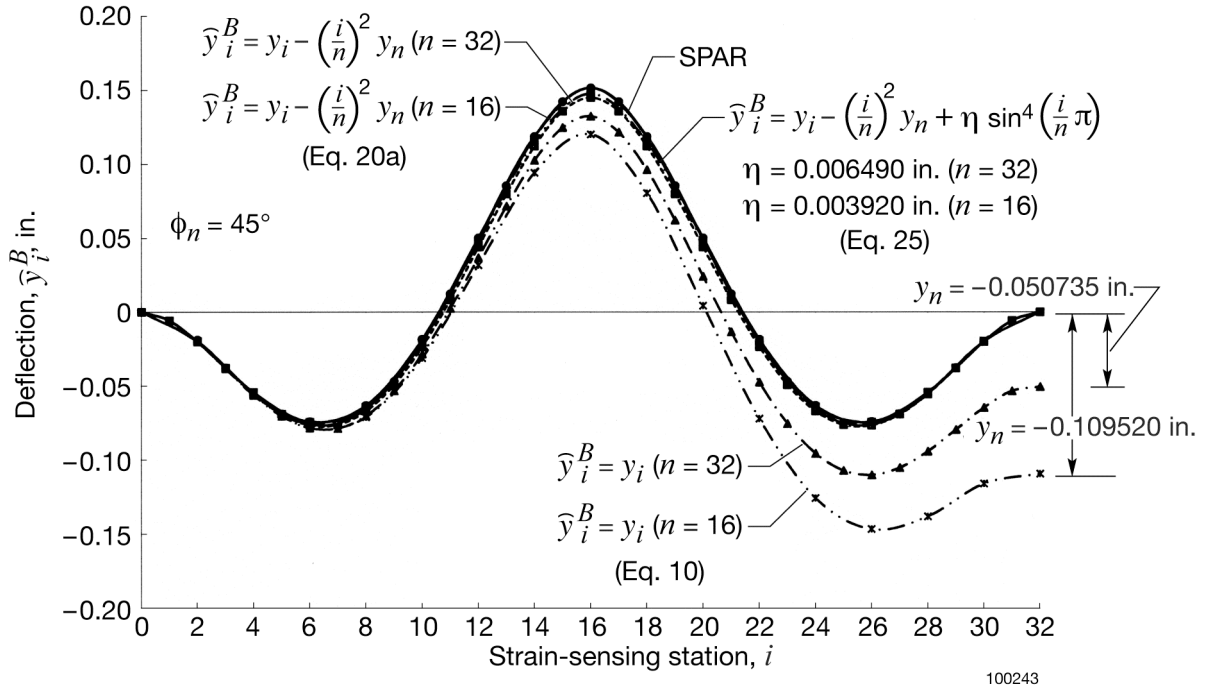


(b) $\phi_n = 45°$

Figure 37. Deflection curves calculated for two-point supported curved beams with different curvatures; both ends clamped; $P$ = 2 lb; $n$ = 32.

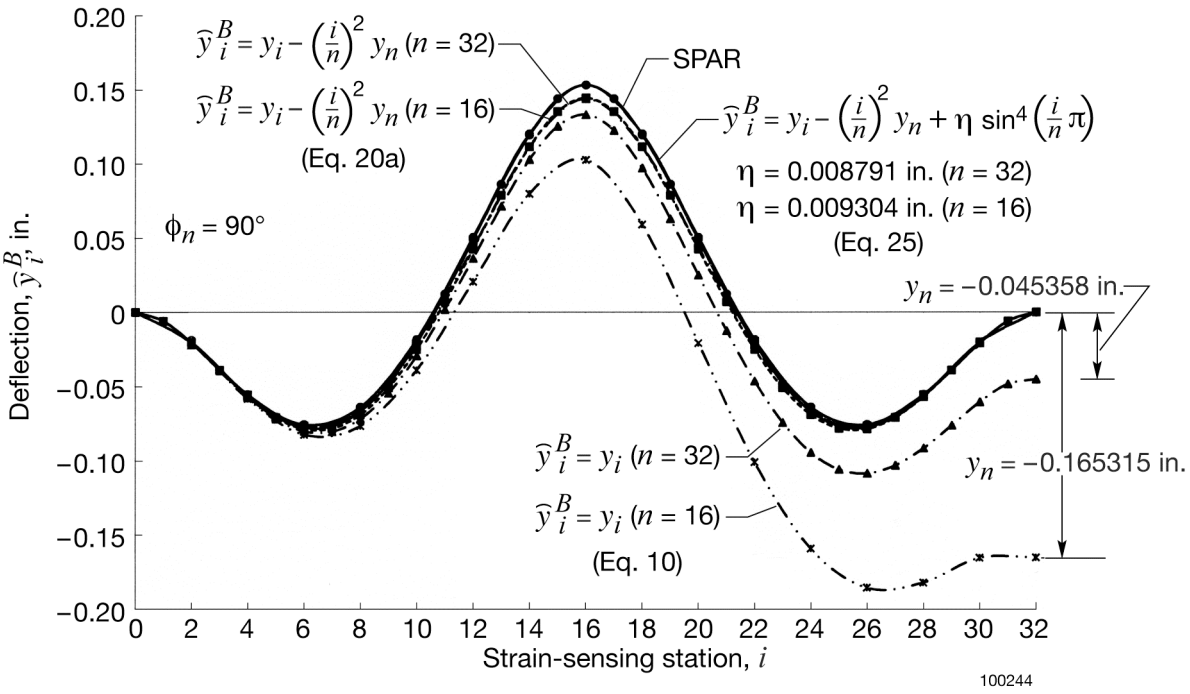


(c) $\phi_n = 90^\circ$

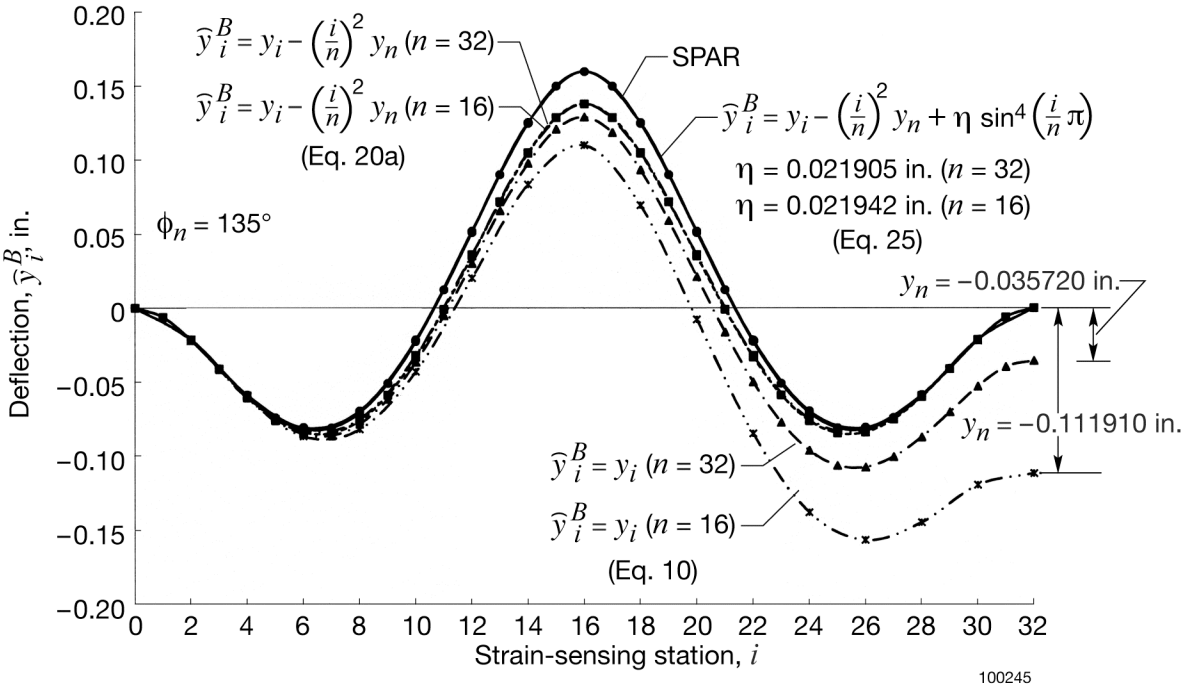


(d) $\phi_n = 135^\circ$

Figure 37. Continued.

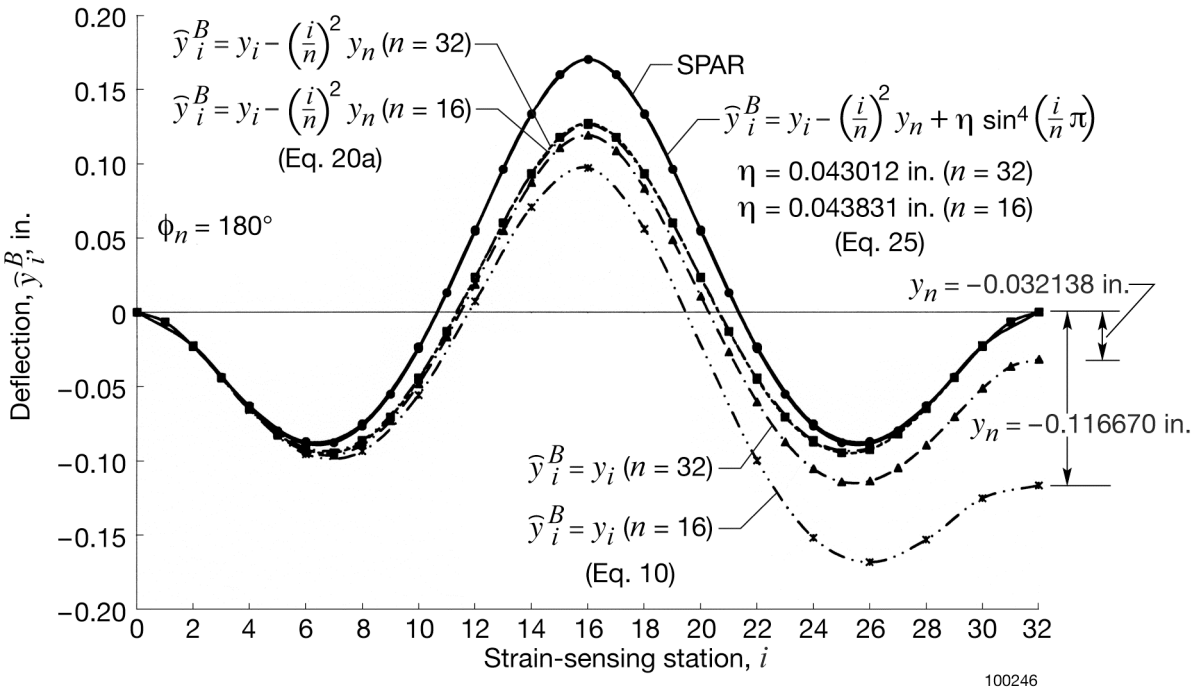


(e) $\phi_n = 180°$

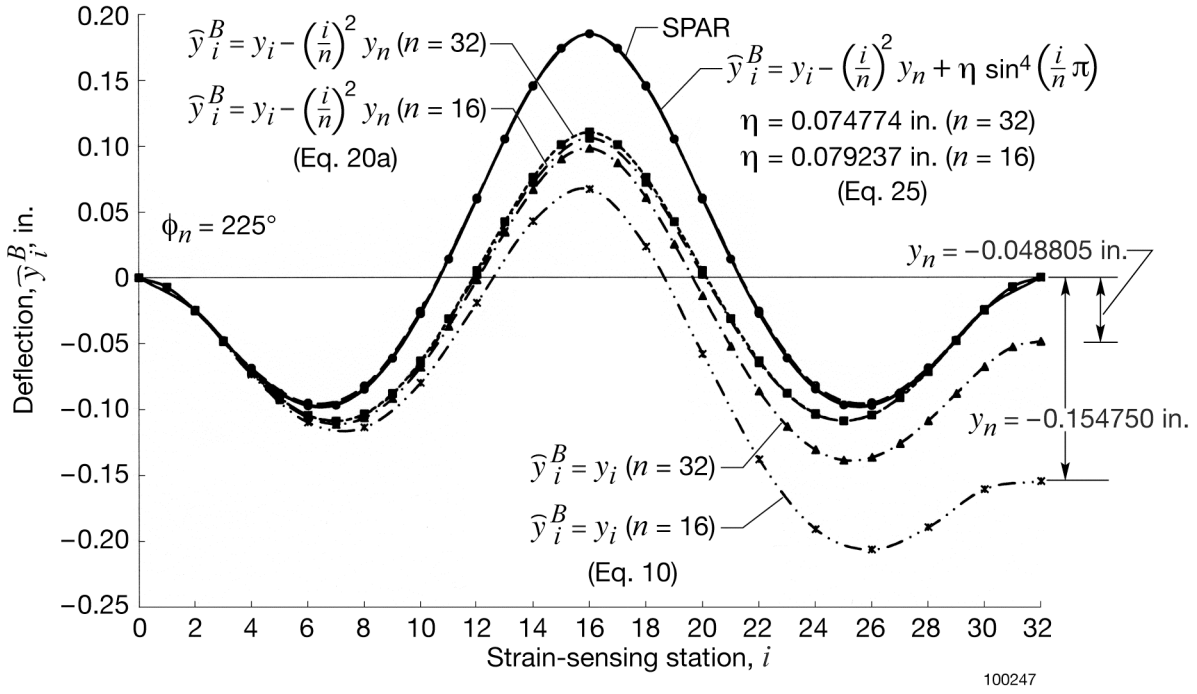


(f) $\phi_n = 225°$

Figure 37. Continued.

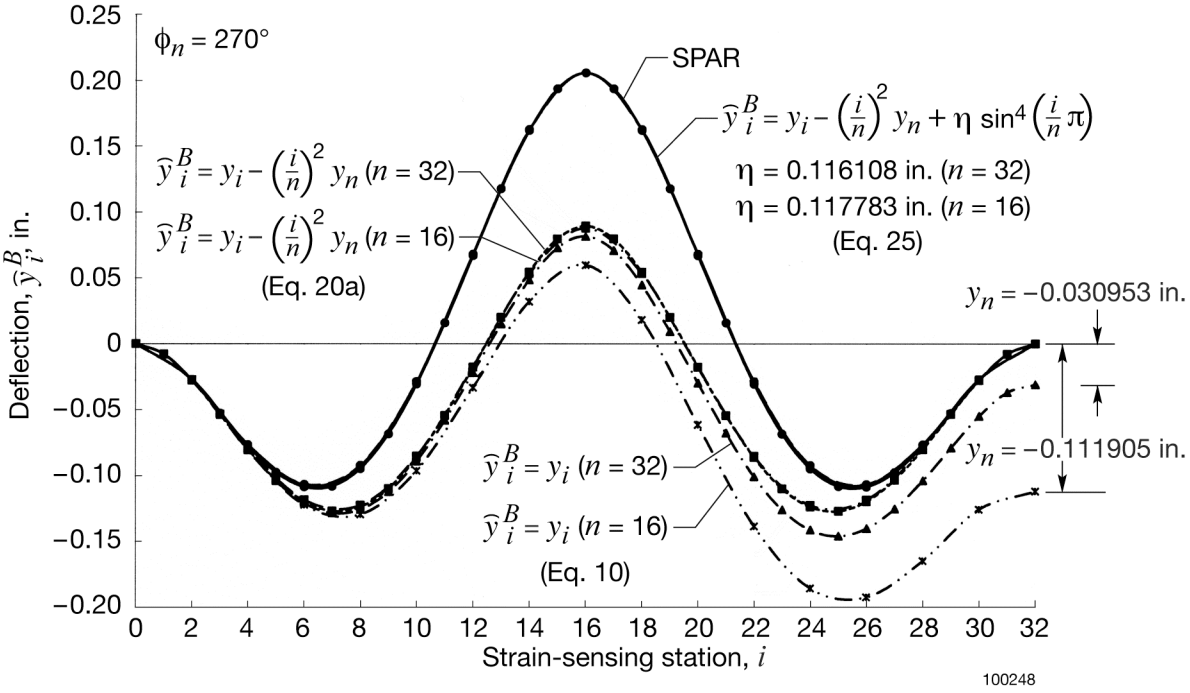


(g) $\phi_n = 270^\circ$

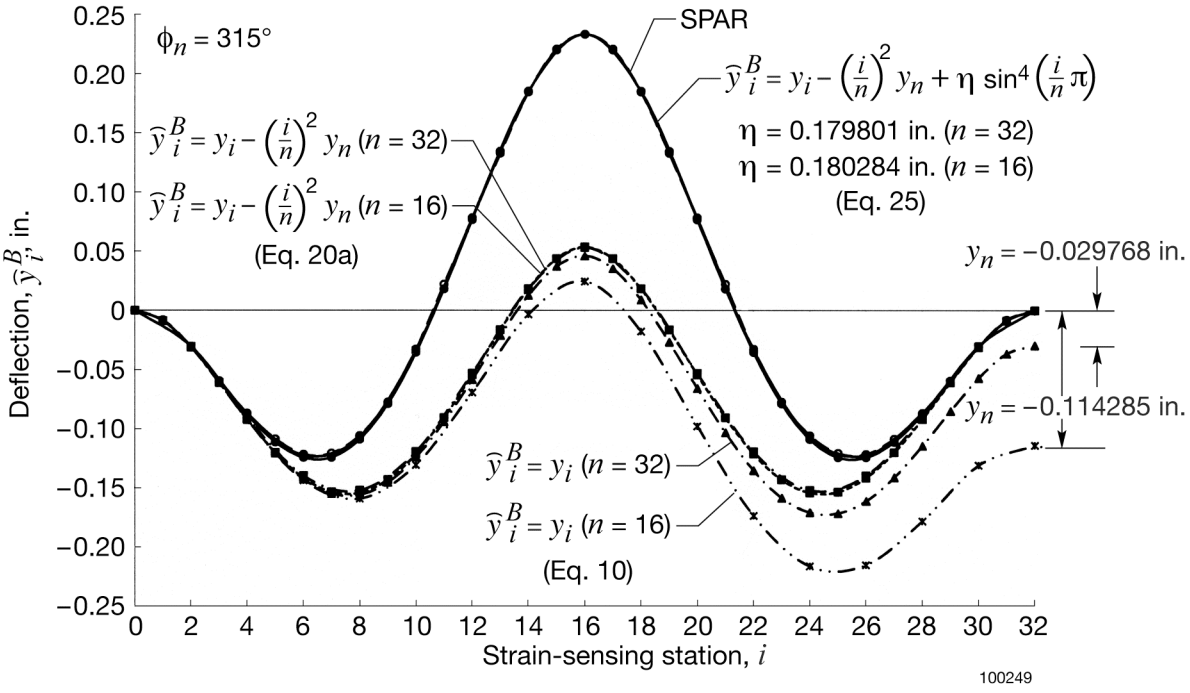


(h) $\phi_n = 315^\circ$

Figure 37. Continued.

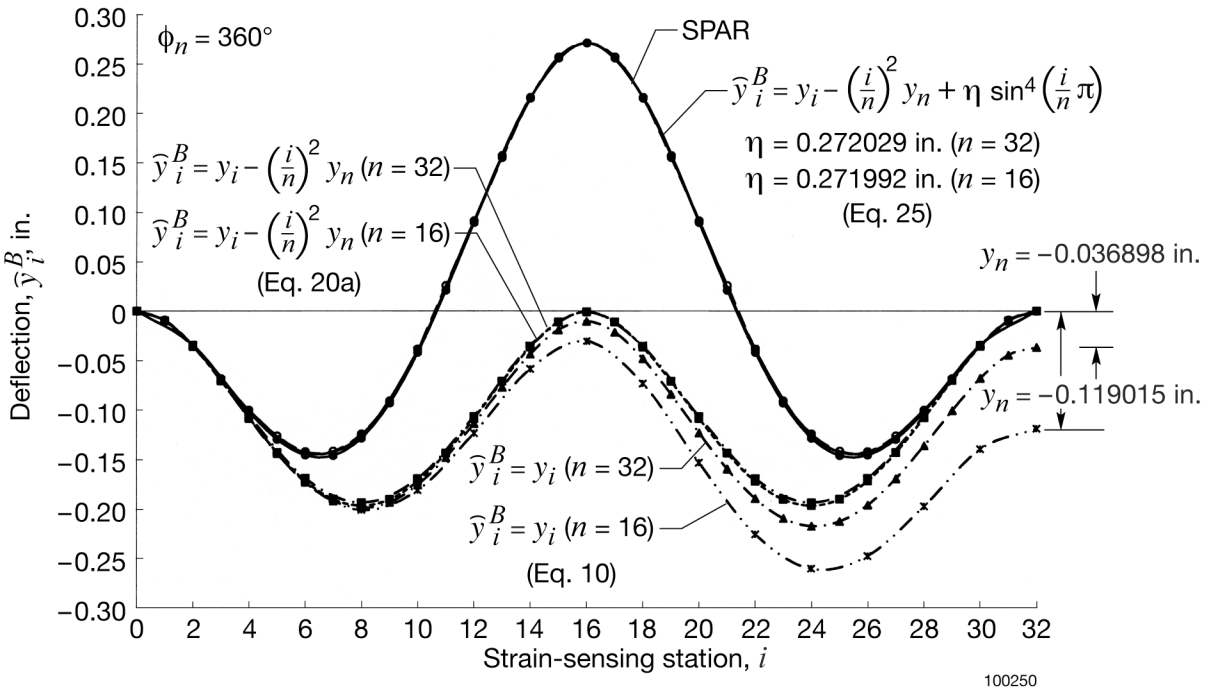


(i) $\phi_n = 360^\circ$

Figure 37. Concluded.

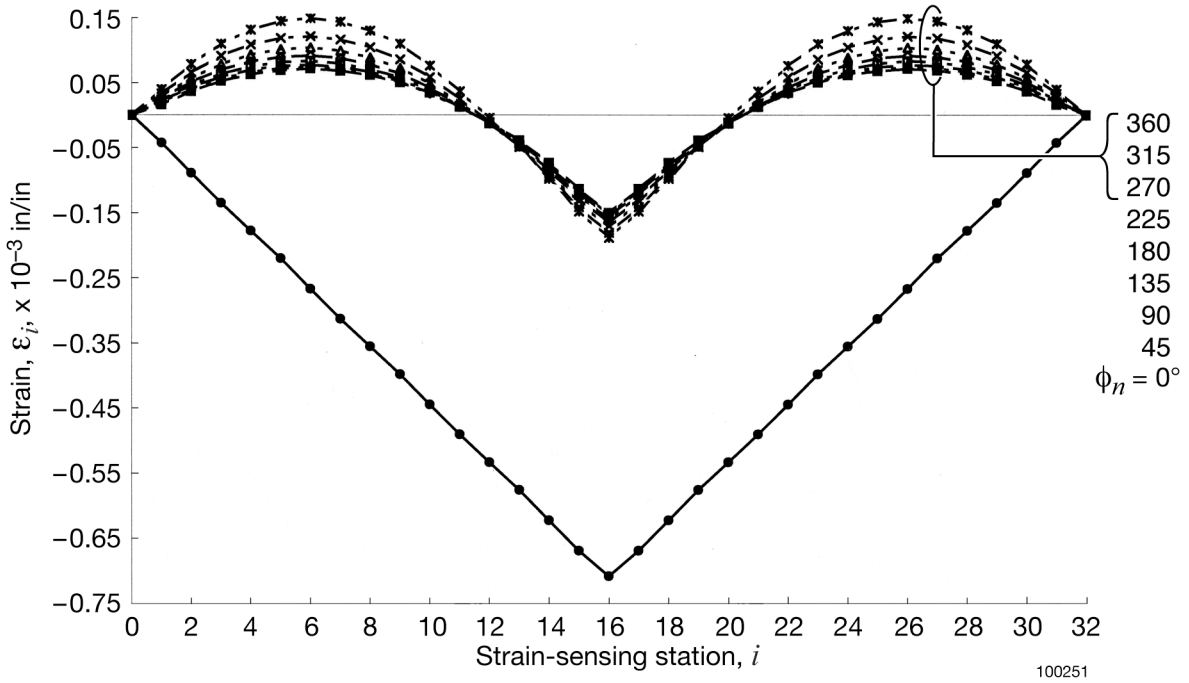


Figure 38. Bending strains, generated from SPAR, for the simply supported curved beam; $P$ = 2 lb; $n$ = 32.

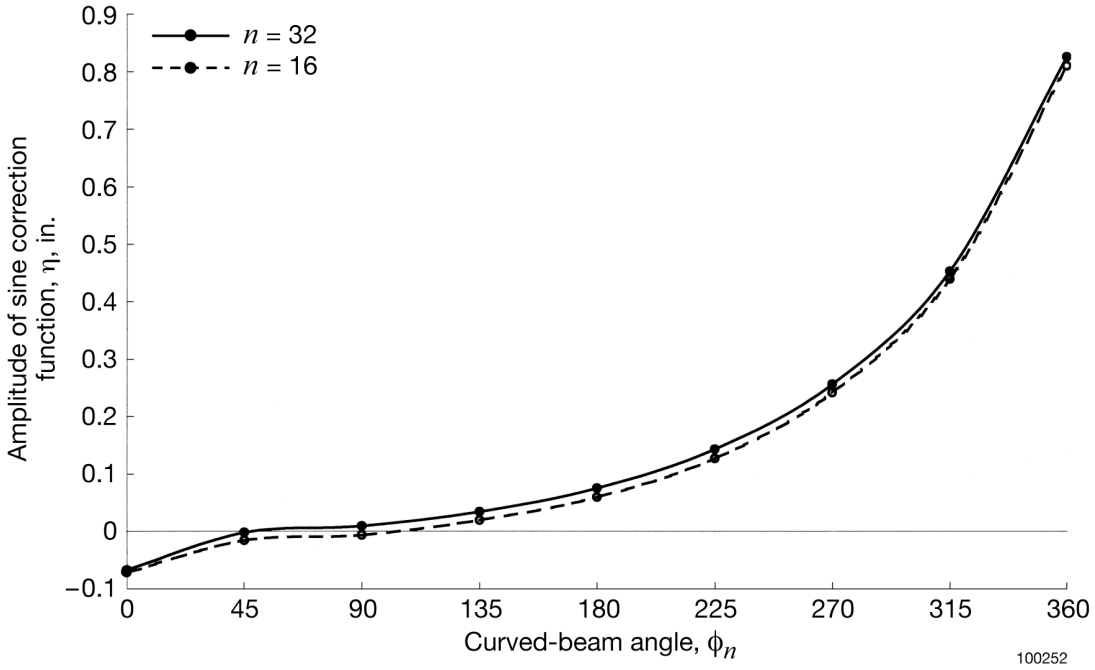


Figure 39. Plot of amplitude of sine correction function, $\eta$, as a function of curved-beam angle for the simply supported curved beam; $n = 32$.

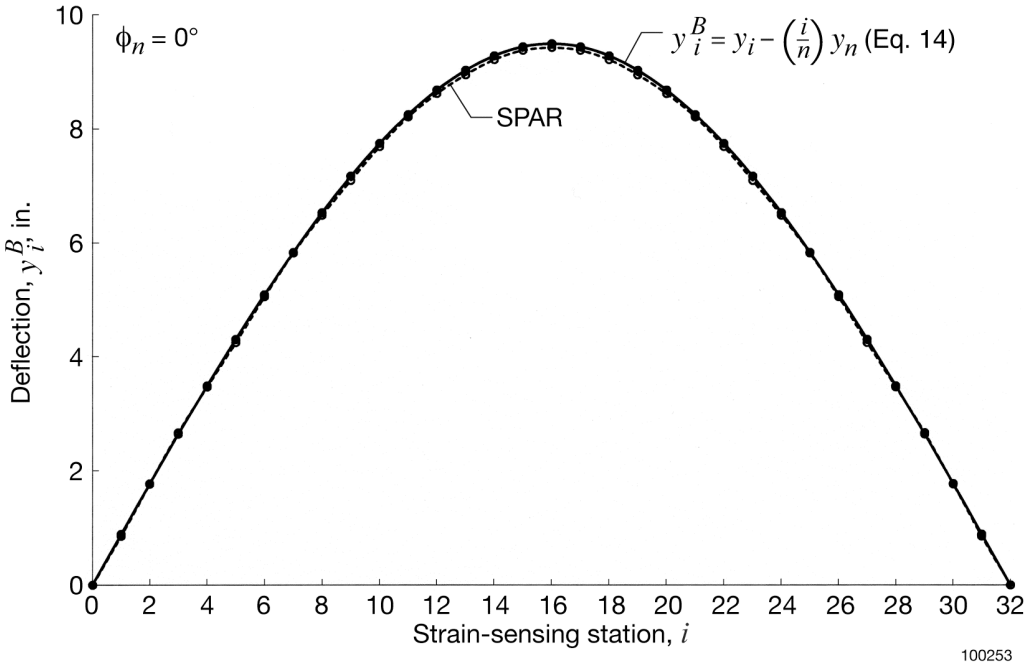


(a) $\phi_n = 0^\circ$

Figure 40. Comparison of SPAR deflection curve with single-point collocation deflection curves for the simply supported curved beam; $\phi_n = 180°$; $P = 2$ lb; $n = 32$.

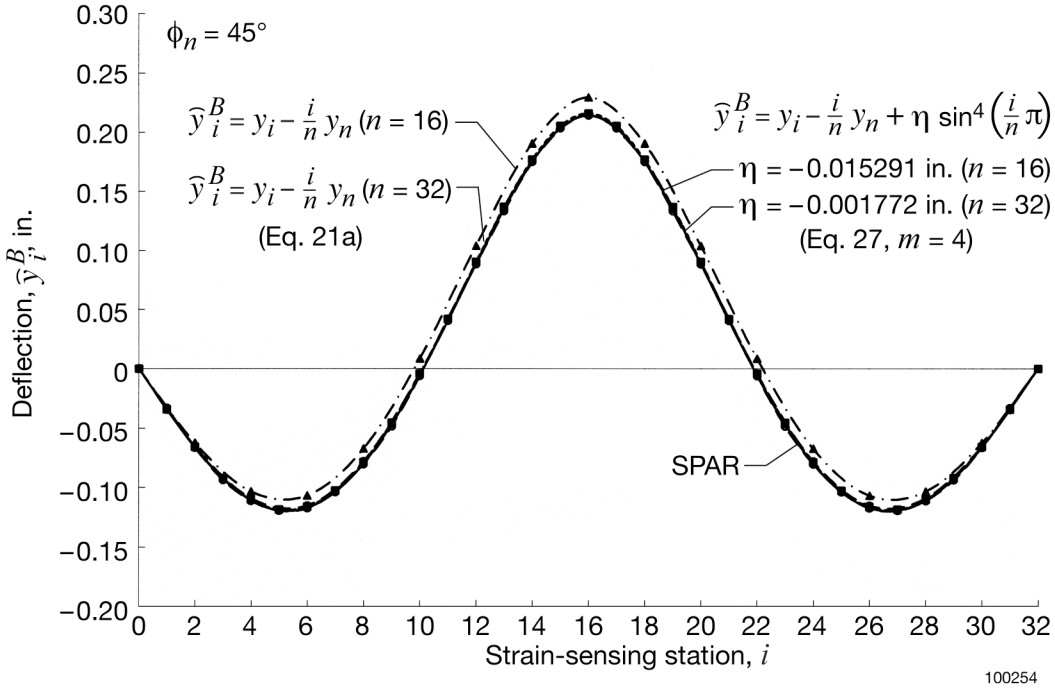


(b) $\phi_n = 45°$

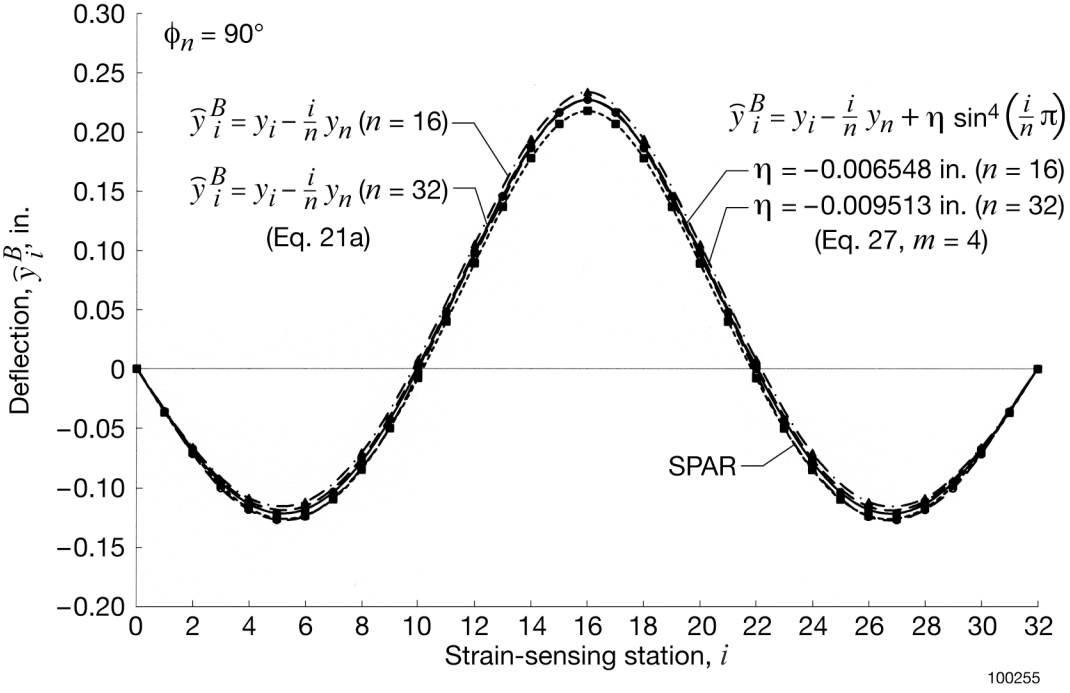


(c) $\phi_n = 90°$

Figure 40. Continued.

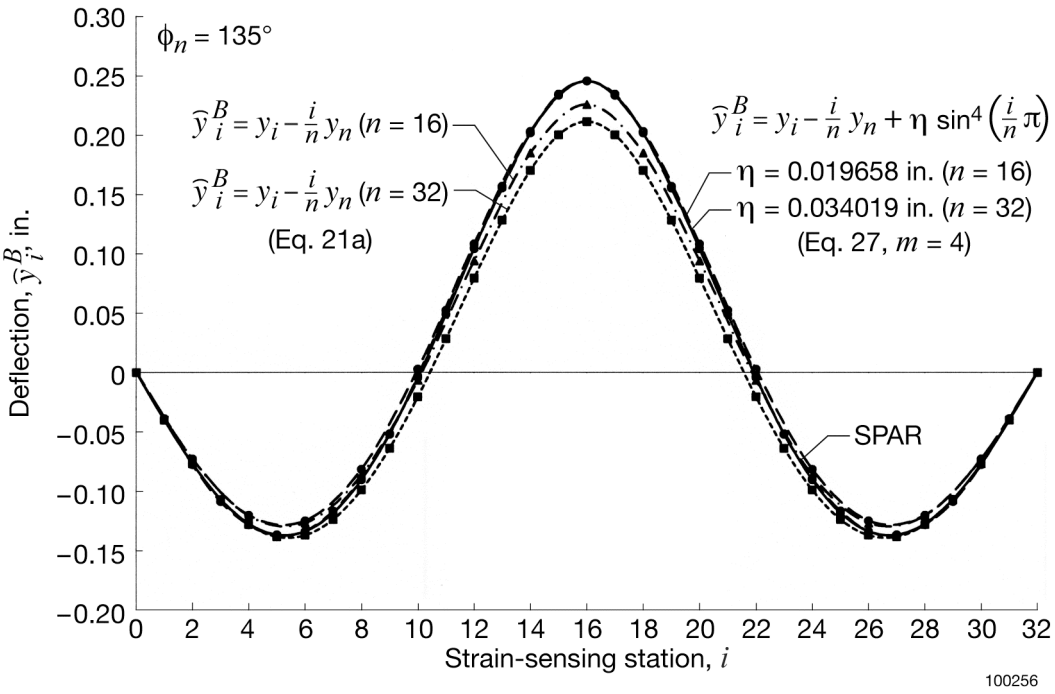


(d) $\phi_n = 135^\circ$

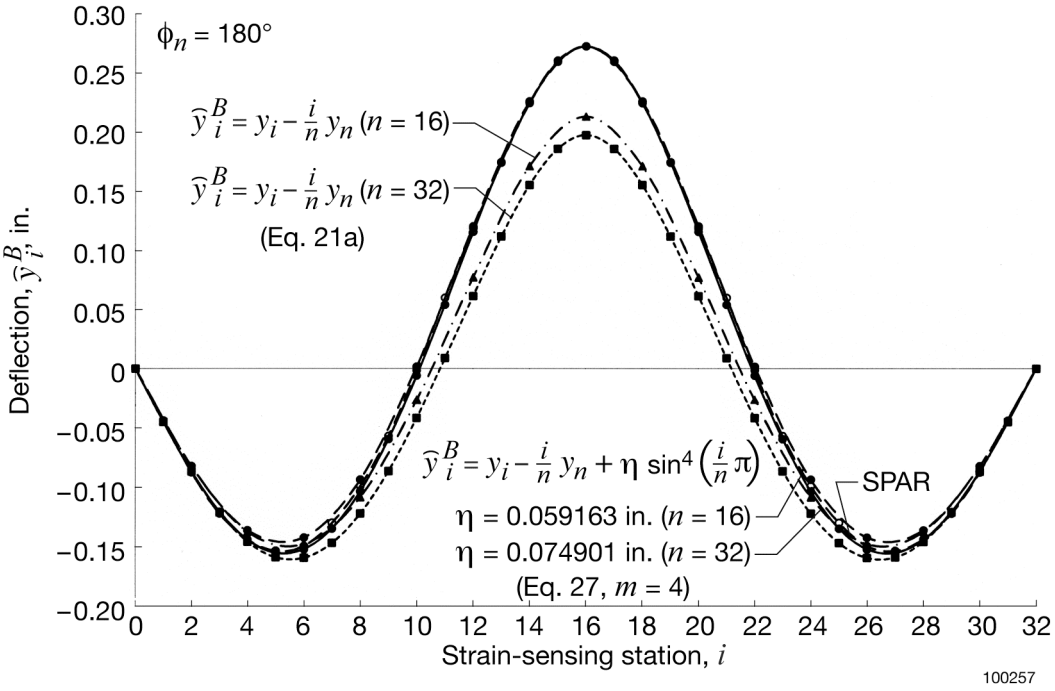


(e) $\phi_n = 180^\circ$

Figure 40. Continued.

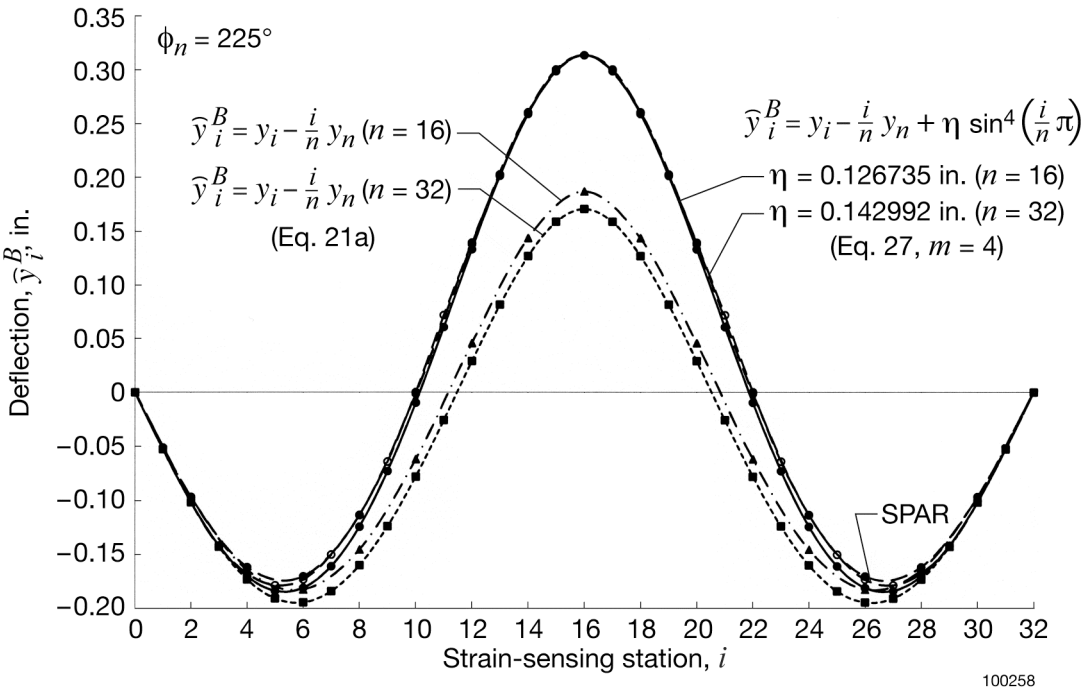


(f) $\phi_n = 225^\circ$

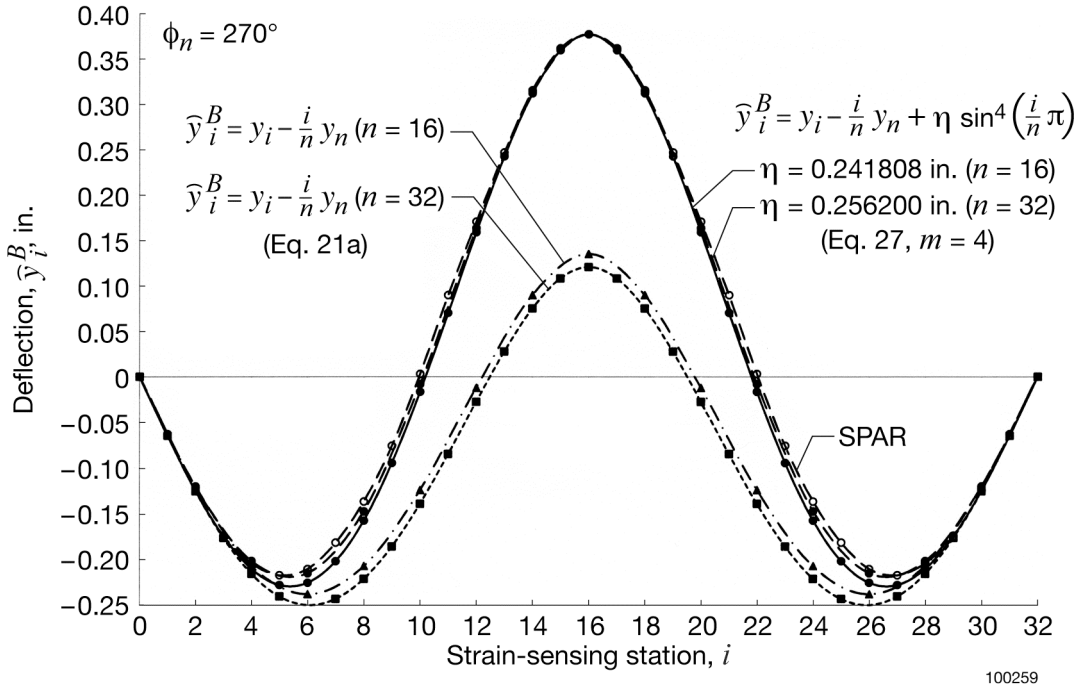


(g) $\phi_n = 270^\circ$

Figure 40. Continued.

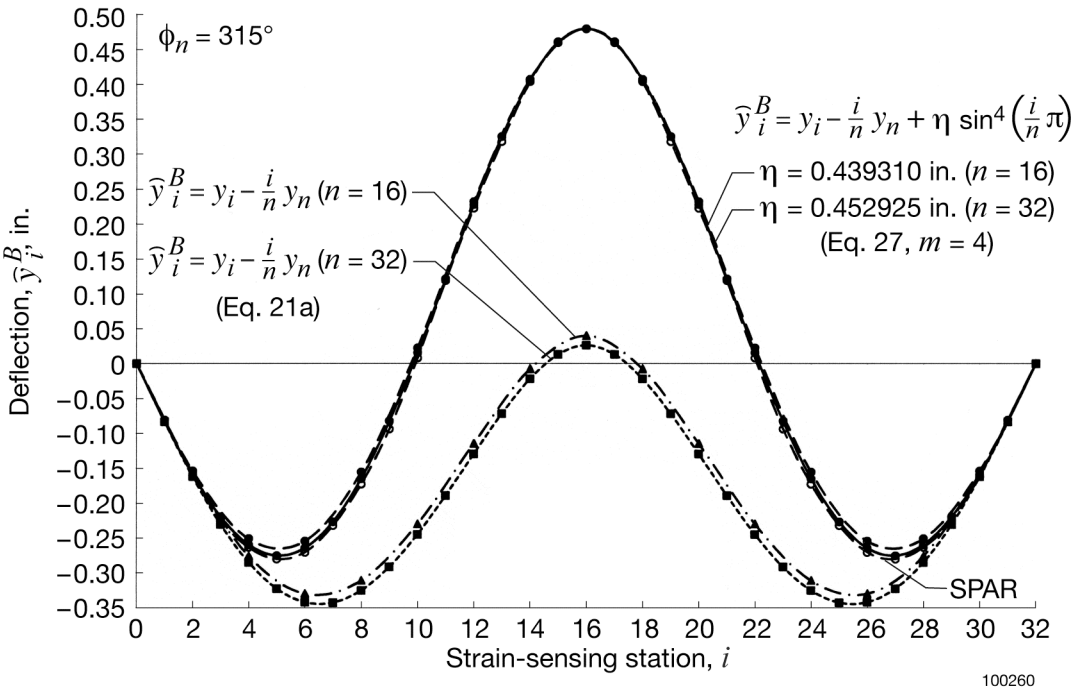


(h) $\phi_n = 315^\circ$

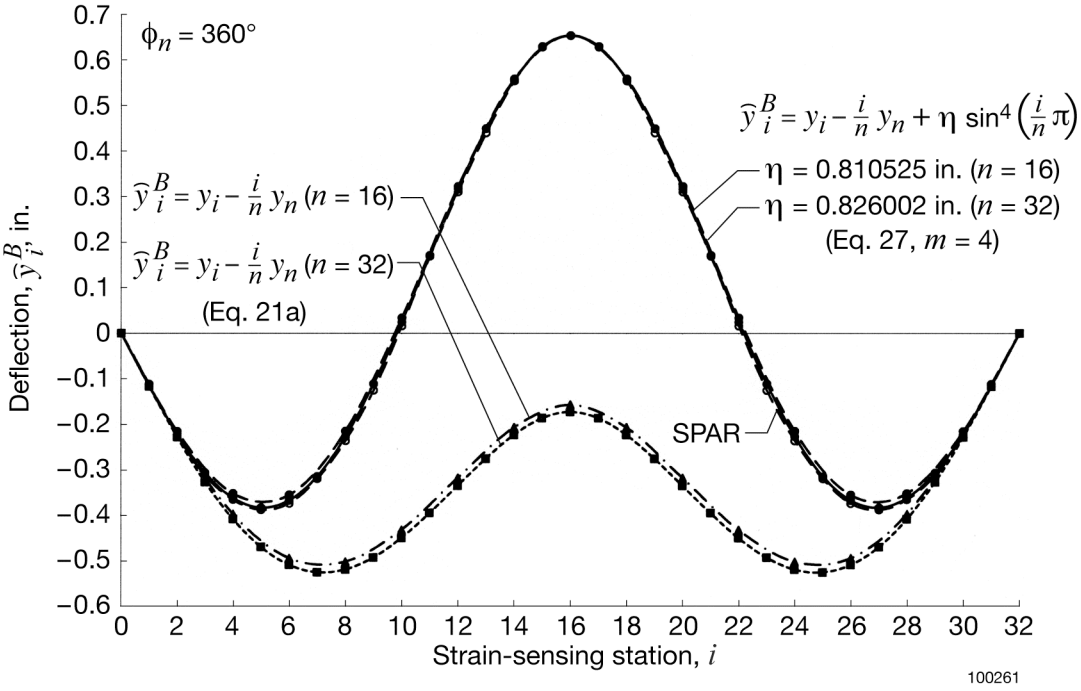


(i) $\phi_n = 360^\circ$

Figure 40. Concluded.

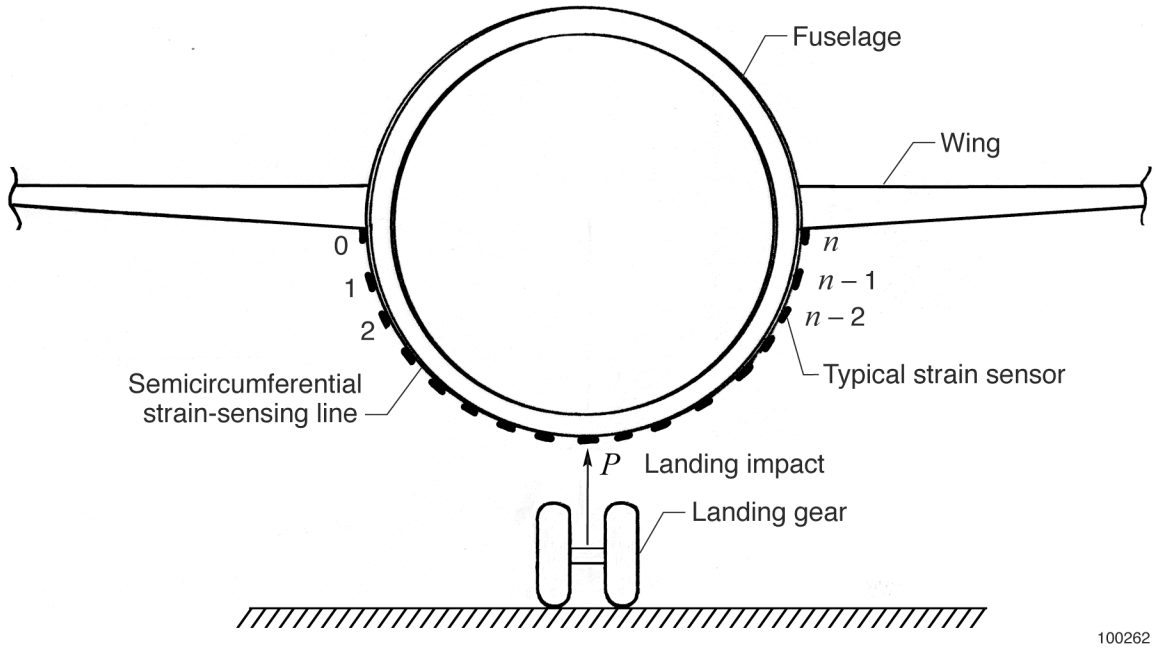


(a) Semicircumferential strain-sensing line system.

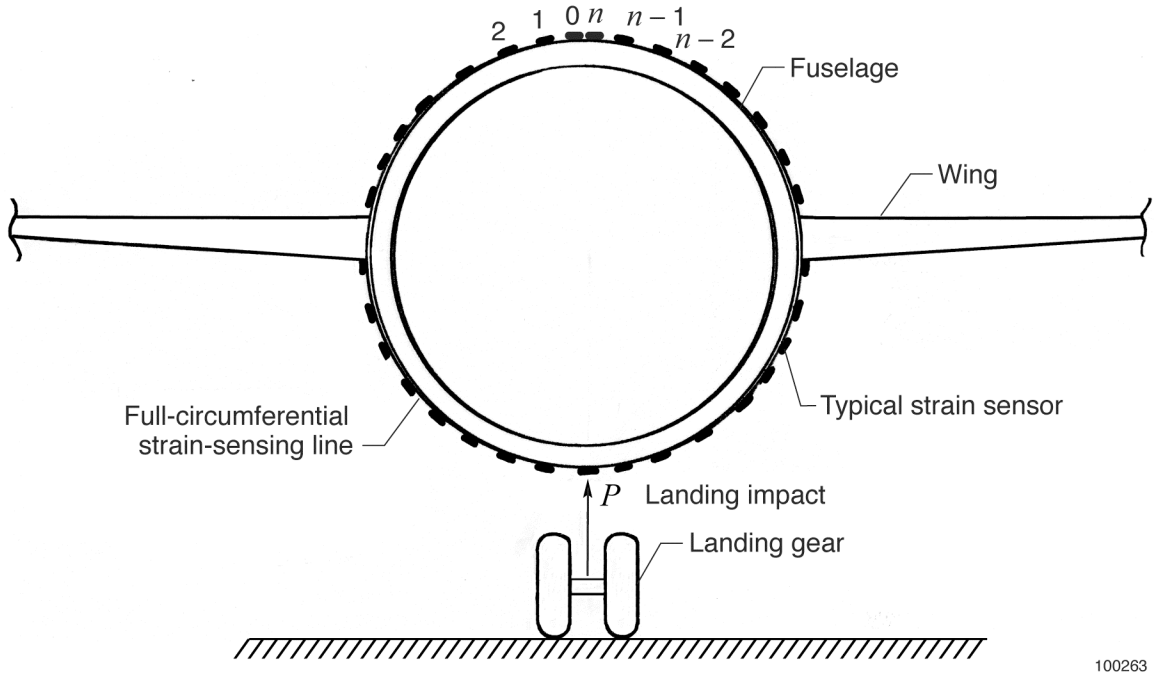


(b) Full-circumferential strain-sensing line system.

Figure 41. Strain-sensing systems for measurements of radial displacements of aircraft fuselage cross sections caused by landing impacts.

# REFERENCES


1. Bang, Hyung-Joon, Hyun-Kyu Kang, Chang-Sun Hong, and Chun-Gon Kim, "Optical Fiber Sensor Systems for Simultaneous Monitoring of Strain and Fractures in Composites," *Smart Materials and Structures*, Vol. 14, Sept. 2005, pp. N52–N58.

2. Wehrle, Günther, Percy Nohama, Hypolito José Kalinowski, Pedro Ingácio Torres, and Luiz Carlos Guedes Valente, "A Fiber Optic Bragg Grating Strain Sensor for Monitoring Ventilatory Movements," *Measurement Science and Technology*, Vol. 12, April 2001, pp. 805–809.

3. Baldwin, Christopher S., Toni J. Salter, and Jason S. Kiddy, "Static Shape Measurements Using A Multiplexed Fiber Bragg Grating Sensor System," *Proceedings of Smart Structures and Materials 2004: Smart Sensor Technology and Measurement Systems*, edited by Eric Udd and Daniele Inaudi, Vol. 5384, San Diego, March 15, 2004, pp. 206–217.

4. Ko, William L., W.L. Richards, and Van T. Tran. *Displacement Theories for In-Flight Deformed Shape Predictions of Aerospace Structures*, NASA/TP-2007-214612, 2007.

5. Ko, William L., and Van Tran Fleischer, *Further Development of Ko Displacement Theory for Deformed Shape Predictions of Nonuniform Aerospace Structures*, NASA/TP-2009-214643, 2009.

6. Ko, William L., *Collection of Memoranda on Applications of Ko Displacement Theory to Deformed Shape Predictions of Aerospace Structures*, NASA BR-119, Aerostructures Branch, Dryden Flight Research Center, Edwards, CA, April 2008.

7. Ko, William L., W. Lance Richards, and Van Tran Fleischer, *Applications of Ko Displacement Theory to the Deformed Shape Predictions of the Doubly-Tapered Ikhana Wing*, NASA/TP-2009-214652, 2009.

8. Ko, William L., and William Lance Richards, *Method for Real-Time Structure Shape-Sensing*, U.S. Patent No. 7,520,176, issued April 21, 2009.

9. Richards, William Lance, and William L. Ko, *Process for Using Surface Strain Measurements to Obtain Operational Loads for Complex Structures*, U.S. Patent No. 7,715,994, issued May 11, 2010.

10. Roark, Raymond J., *Formulas for Stress and Strain*, Third Edition, McGraw-Hill Book Company, Inc., New York, 1954.

11. Faupel, Joseph, H., *Engineering Design: A Synthesis of Stress Analysis and Materials Engineering*, John Wiley and Sons, Inc., New York, 1964.

12. Whetstone, W.D., *SPAR Structural Analysis System Reference Manual*, System Level 13A, Vol. 1, Program Execution, NASA CR-158970-1, 1978.

# REPORT DOCUMENTATION PAGE

*Form Approved*
*OMB No. 0704-0188*



| 1. REPORT DATE *(DD-MM-YYYY)* | 2. REPORT TYPE | 3. DATES COVERED *(From - To)* |
|---|---|---|
| 01-04-2011 | Technical Publication | |

**4. TITLE AND SUBTITLE**
Extension of Ko Straight-Beam Discplacement Theory to Deformed Shape Predictions of Slender Curved Structures

**5a. CONTRACT NUMBER**

**5b. GRANT NUMBER**

**5c. PROGRAM ELEMENT NUMBER**

**6. AUTHOR(S)**
Ko, William L. and Fleischer, Van Tran

**5d. PROJECT NUMBER**

**5e. TASK NUMBER**

**5f. WORK UNIT NUMBER**

**7. PERFORMING ORGANIZATION NAME(S) AND ADDRESS(ES)**
NASA Dryden Flight Research Center
P.O. Box 273
Edwards, CA 93523-0273

**8. PERFORMING ORGANIZATION REPORT NUMBER**
H-3073

**9. SPONSORING/MONITORING AGENCY NAME(S) AND ADDRESS(ES)**
National Aeronautics and Space Administration
Washington, DC 20546-0001

**10. SPONSORING/MONITOR'S ACRONYM(S)**
NASA

**11. SPONSORING/MONITORING REPORT NUMBER**
NASA/TP-2011-214657

**12. DISTRIBUTION/AVAILABILITY STATEMENT**
Unclassified -- Unlimited
Subject Category 39 Availability: NASA CASI (443) 757-5802 Distribution: Standard

**13. SUPPLEMENTARY NOTES**
Ko and Fleischer, NASA Dryden Flight Research Center

**14. ABSTRACT**

The Ko displacement theory originally developed for shape predictions of straight beams is extended to shape predictions of curved beams. The surface strains needed for shape predictions were analytically generated from finite-element nodal stress outputs. With the aid of finite-element displacement outputs, mathematical functional forms for curvature-effect correction terms are established and incorporated into straight-beam deflection equations for shape predictions of both cantilever and two-point supported curved beams. The newly established deflection equations for cantilever curved beams could provide quite accurate shape predictions for different cantilever curved beams, including the quarter-circle cantilever beam. Furthermore, the newly formulated deflection equations for two-point supported curved beams could provide accurate shape predictions for a range of two-point supported curved beams, including the full-circular ring. Accuracy of the newly developed curved-beam deflection equations is validated through shape prediction analysis of curved beams embedded in the windward shallow spherical shell of a generic crew exploration vehicle. A single-point collocation method for optimization of shape predictions is discussed in detail.

**15. SUBJECT TERMS**
Curvature-effect corrections, Curved-beam shape predictions, Deflection equations, Distributed surface strains, Ko Displacement Theory

| 16. SECURITY CLASSIFICATION OF: | | | 17. LIMITATION OF ABSTRACT | 18. NUMBER OF PAGES | 19b. NAME OF RESPONSIBLE PERSON |
|---|---|---|---|---|---|
| a. REPORT | b. ABSTRACT | c. THIS PAGE | | | STI Help Desk at email: help@sti.nasa.gov |
| | | | | | 19b. TELEPHONE NUMBER *(Include area code)* |
| U | U | U | UU | 83 | (443) 757-5802 |